

PETER ZEILER SKANDS

L-Violating Supersymmetry

IMPLEMENTATION IN PYTHIA AND STUDY OF LHC DISCOVERY POTENTIAL



THESIS FOR THE DEGREE
CANDIDATUS SCIENTIARUM IN PHYSICS

JULY 28, 2001
NIELS BOHR INSTITUTE
DEPARTMENT FOR EXPERIMENTAL HIGH ENERGY PHYSICS

This thesis is submitted for evaluation in accordance with the requirements for obtainment of the degree of Cand. Scient. in physics at the Niels Bohr Institute, University of Copenhagen.

I am very grateful to the Lørup foundation, the Nordic Academy for Advanced Study (NorFA), and the Niels Bohr Institute (the HEP group in particular) for financial support. In addition, I would like to thank the University of Rostock and the Volkswagen Stiftung, the University of Uppsala and the Nobel Committee, the University of Oslo, the CTEQ/IPPP Summer School 2001, and the THEP group at Lund University.

`Mathematica` is a copyrighted program, trademark of Wolfram Research, Inc.

Version numbers for publically available programs used in this work are `-PYTHIA` v.6.155, `ISAJET` v.7.51, `HERWIG` v.6.2, and `At1Fast` v.2.53.

Internal Supervisor (NBI):

John Renner Hansen

Niels Bohr Institute (HEP), University of Copenhagen

Blegdamsvej 17 DK-2100 Copenhagen Ø

renner@nbi.dk

External Supervisor (Lund):

Torbjörn Sjöstrand

Dep. of Theoretical High Energy Physics, Lund University,

P.O. Box 118 SE-221 00 Lund

Torbjorn.Sjostrand@thep.lu.se

Peter Z. Skands

Abstract

In the Minimal Supersymmetric Standard Model (MSSM), the simultaneous appearance of lepton and baryon number violation causes the proton to decay much faster than the experimental bound allows. Customarily, a discrete symmetry known as R -parity is imposed to forbid these dangerous interactions. This work begins by arguing that there is no deep theoretical motivation for preferring R -parity over other discrete symmetries and continues by adopting the MSSM with baryon number conservation replacing R -parity conservation. For the purpose of studying the influence of the consequent lepton number violating interactions, 1278 new decay channels of supersymmetric particles into Standard Model particles have been included in the PYTHIA event generator.

The augmented event generator is then used in combination with the **AtlFast** detector simulation to study the impact of lepton number violation (\cancel{L}) on event topologies in the ATLAS detector, and trigger menus designed for \cancel{L} -SUSY are proposed based on very general conclusions. The subsequent analysis uses a combination of primitive cuts and neural networks to optimize the discriminating power between signal and background events. In all scenarios studied, it is found that a 5σ discovery is possible for cross sections down to 10^{-10} mb with an integrated luminosity of 30 fb^{-1} , corresponding to one year of data taking with the LHC running at “mid-luminosity”, $L = 3 \times 10^{33} \text{ cm}^{-2} \text{ s}^{-1}$.

Contents

1	Introduction	5
1.1	Outline	8
2	Supersymmetry	9
2.1	What <i>is</i> Supersymmetry?	9
2.2	Properties of SUSY	11
2.2.1	Sparticles and Mixing	13
2.2.2	Supersymmetry Breaking	15
2.3	Motivations for SUSY	16
2.3.1	The Hierarchy Problem	16
2.3.2	Other Motivations	18
2.4	R -breaking Supersymmetry	19
2.4.1	Experimental Indications of R -Violation?	20
3	L-violating Decays of SUSY Particles	23
3.1	The Model	23
3.2	The L -Violating Lagrangian	25
3.3	Purely Leptonic Decays	26
3.3.1	Scalar Decays	26
3.3.2	Kinematics and Phase Space Topologies	27
3.3.3	Neutralino Decays	30
3.3.4	Chargino Decays	31
3.4	\cancel{L} Decays Involving (s)quarks.	31
3.4.1	Gluino Decays	32
3.5	The Monte Carlo method and PYTHIA	32
4	The ATLAS Detector and ATLFAST	36
4.1	The Beam	37
4.2	Inner Detector	37
4.3	Calorimeters	38
4.3.1	EM Calorimeters	38
4.3.2	Hadronic Calorimeters:	38
4.4	Calorimetry in ATLFAST:	39
4.5	Muon System	41
5	Analysis of ATLAS \cancel{L}-SUSY Discovery Potential	43
5.1	Points of Analysis	44
5.2	Trigger Selection	46
5.2.1	\cancel{L} -SUSY Triggers at Mid-Luminosity	46
5.2.2	Final Remarks	49
5.3	Discriminating Variables	49
5.3.1	Missing Transverse Energy	53
5.3.2	Hard Leptons and Jets	56
5.3.3	LSP Decay Signature	60

5.3.4	Thrust	62
5.3.5	Oblateness and Circularity	63
5.4	Pattern Recognition with Neural Networks	67
5.4.1	What Neural Networks Do	67
5.4.2	Network Layout and Network Learning:	68
5.4.3	Network Training	70
5.4.4	Optimal Brain Damage	71
5.5	Results	73
6	Outlook and Conclusion	78
6.1	Outlook	78
6.2	Conclusion	79
A	Decays of SUSY particles: Conventions and References	81
B	Phase Space Integrations in Dalitz Variables	81
B.1	Numerical Integration Procedure for Virtual Contributions	82
B.2	Numerical Integration Procedure for Total Exclusive Contributions	83
C	\cancel{e}^--SUSY in PYTHIA. User's Reference.	85
C.1	Switches & Parameters set by the user in the PYTHIA calling program	85
C.2	Subroutines and functions handling R -violation inside PYTHIA	86
C.2.1	Warnings and error messages:	87
C.3	Resonant decay treatment	87
D	Trigger Shapes	88
D.1	Background Rates	88
D.2	Signal Efficiencies	92
	References	95

List of Figures

1	Schematic of the ATLAS detector.	6
2	A graphical illustration of supermultiplets	12
3	Proton decay via L and B violating SUSY vertices.	19
4	Neutrinoless double β decay	21
5	Deep Inelastic Scattering at HERA	21
6	\cancel{e}^- decay of a slepton to two leptons	27
7	Contributions to $\tilde{\chi}_m^0 \rightarrow \bar{\nu}_i \ell_j^+ \ell_k^-$	28
8	Kinematics of a three-body decay containing a resonance	29
9	Phase space topologies	30
10	The ATLAS Inner Detector system	37
11	The ATLAS Hadronic Tile Calorimeter	39
12	The ATLAS muon system	42
13	Missing E_T for SM and SUSY processes.	54

14	Fit to the \cancel{E}_T tail of low p_T QCD events.	56
15	Lepton multiplicities in the SM and SUSY.	57
16	Jet multiplicities in the SM and SUSY.	57
17	Lepton versus jet multiplicity in the SM and mSUGRA P_9	58
18	p_T distribution for hardest object in SM and SUSY.	59
19	LSP decay signature for SM and SUSY.	61
20	Thrust distributions for SM and SUSY.	63
21	Oblateness distributions for SM and SUSY.	64
22	Decay of a very massive resonance	65
23	Circularity distributions for SM and SUSY.	66
24	The logistic function	69
25	Layout of the neural networks	70
26	Sketch of the MSSM network	72
27	Learning Curves for the LLE network	74
28	Network outputs for background events	75

List of Tables

1	Supermultiplets and superfields in the MSSM	13
2	$\sin^2 \theta_W$ – measured value and predictions from supersymmetric and SM GUTs.	18
3	Assumed reconstruction efficiencies for muons and electrons	41
4	Selected points in the mSUGRA space	44
5	Selected points in the $\lambda - \lambda'$ space	45
6	Trigger rates and efficiencies for $L = 3 \times 10^{33} \text{cm}^{-2} \text{s}^{-1}$	48
7	Numbers of generated SM events for the analysis	51
8	Numbers of generated SUSY events for the analysis	52
9	Event numbers passing cuts on \cancel{E}_T	55
10	Event numbers passing cuts on N_{jets} and N_{leptons}	58
11	Event numbers passing cuts on p_T^{hard}	59
12	Event numbers passing cuts on P_{4C}	62
13	Event numbers passing cuts on thrust.	62
14	Event numbers passing cuts on oblateness.	65
15	Event numbers passing cuts on circularity.	66
16	Inputs to the neural net	69
17	Event numbers remaining after network cuts	75
18	ATLAS Discovery Potential	77
19	Numbers of generated events for the trigger study	89

Once, this Earth was haunted by the flaming angels of elusive gods and by magic that seemed to move the heavenly spheres. These mythic tales seem but superstitious fantasy, despite their depth of colour, to the rational and sane of an enlightened society. And yet this universe appears to the inquisitive mind still so enigmatic, so full of the very mystery that breathed life and beauty into our earliest imagination that man's greatest tragedy would be to dull his senses and not still, despite the limits of his Earthly mind, seek to grasp the nature of that which brought him forth.

1 Introduction

The Herculean task of recapitulating the history of the science of physics or even that small part of it which has direct connection to this work is better left to other authors, yet for the inexperienced reader, I here will briefly set the stage on which the present work has been performed.

The essence of the school of thought initiated by Thales and his two contemporaries in sixth century (BC) Ionian Miletus, Anaximander and Anaximenes, can be expressed as a belief that the world is not governed by the wills and vanities of Gods but instead by immutable and “natural” laws arising from fundamental relationships between some basic elements of Nature. This thought, formulated as the Democritian hypothesis that Nature, at the most fundamental level, consists of a set of indivisible basic elements, still dominates the science of physics. Today, the twilight of possible discoveries is found deep within the atomic nucleus and even deeper, within the nucleons themselves, at the smallest length scales yet probed by any experiment. In the continued quest for Democritus’ elements, we have reached objects which, if size they have, are smaller than a billionth of a billionth of a meter across, around a billionth the size of a normal atom. We do not yet know whether these objects have any internal structure. They are the quarks and leptons (6 of each) which constitute all matter known to us and the bosons which carry the three fundamental forces of Nature known to us. The fourth force, gravity, is still lacking a complete description.

Combined, these particles and the interactions between them (excepting gravity) are incorporated in a theoretical framework known as the Standard Model of particle physics (the SM). We know that this model cannot be the whole story as it contains some internal inconsistencies, and therefore a number of speculations on the possible existence of more hitherto undiscovered properties of Nature has arisen. That Nature could contain a special symmetry known as supersymmetry is one of these speculations, and our belief in it is spurred on by its providing an elegant solution to a fundamental problem in the Standard Model connected with the nature of mass and by its being a key ingredient in many of the attempts to provide a quantum description of gravity. These theoretical speculations are not without relevance to the world of experimental physics. There are many who believe that the Large Hadron Collider (LHC) which is scheduled to commence operations at CERN in 2006 will see the first experimental indications of supersymmetry in Nature. This machine, the result of the combined efforts of thousands of engineers and physicists around the globe, will collide protons against protons at hitherto unprecedented energies, allowing us to probe the extremely small length scales at which supersymmetry, if it is indeed a property of Nature, should reveal itself. The exact nature of supersymmetry and its consequences are described in the main body of this text, yet first two very important aspects of present day high energy physics deserve to be introduced.

1) The Experiment: The ATLAS detector is one of four detectors being constructed for the LHC. Its name is obtained by a rather contrived abbreviation of *A Toroidal LHC Apparatus*. It will be located in a newly excavated cavity in the tunnel that used to house the LEP accelerator 140 metres below ground level at the CERN laboratory on the French-Swiss border near Geneva. At the point where ATLAS will be located, the two beams of the LHC, circulating in opposite directions at very close to a billion kilometers per hour, will be brought to cross, and approximately a billion collisions of protons against protons will take place per second. For someone interested in Supersymmetry or other

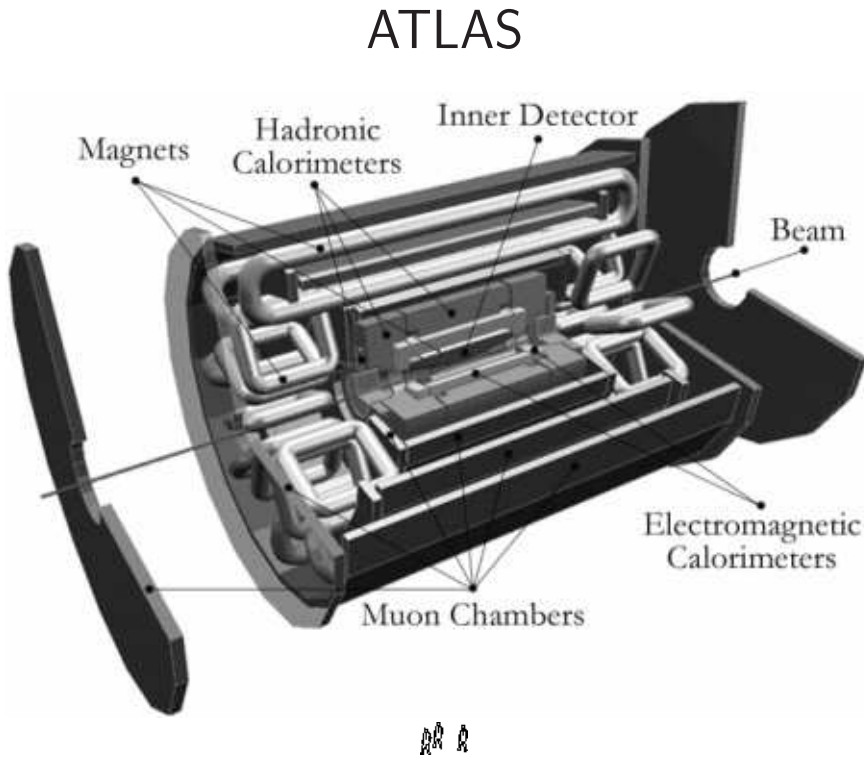


Figure 1: Schematic of the ATLAS detector. When completed, the construction will be about four stories in height and occupy a ground area equivalent to half a football field.

rare physics, this number is crucial. Even with this colossal event rate (and assuming of course that Supersymmetry exists), less than *once per ten* seconds will the processes studied in this work occur. That means that we must somehow be able to tell the difference between a “supersymmetric event” and a “normal” one to a very high precision. If we are wrong more than approximately 1 time in 100 million, we will effectively be blind to supersymmetry. With the aid of sophisticated computer simulations of both normal physics and supersymmetric physics, a significant part of this thesis has been to study how well we can expect to isolate the “signal” from the “background” processes.

From the technical point of view, the ATLAS detector itself follows the by now classic “cylindrical onion” design for collider detectors, beginning with a vertex detector closest to the beam pipe surrounded by tracking detectors immersed in a strong magnetic field, these again being surrounded by calorimeters and finally muon chambers.

Briefly stated, the purpose of the vertex detector is to measure where the produced particles are coming from. The tracking detectors then measure where the (charged) particles are *going*. A strong magnetic field is applied to bend these tracks, allowing the momenta of the particles making the tracks to be measured. It is thereafter the task of the calorimeters to completely stop the particles, neutral ones as well as charged, and in the process give off a signal proportional to the energy of each particle, completing the energy-momentum measurement for the charged particles. The last particles to get caught are the muons. Their high penetration ability makes special measures necessary, and so the outermost part of the detector is the muon chambers. Another magnetic field is

applied here (see fig. 1). The resulting bending of the muon tracks yields a more accurate measurement of the muon momenta.

A last, quite remarkable thing about ATLAS is the extreme data rates which will be output from the experiment with approximately 1 billion events per second, each consisting of about 1MB of data [1]. Using both hardware close to the detector and software farther away from it (quite possibly even on another continent), this tremendous data stream is reduced in real time to a level where “only” 1 PetaByte, or one million GigaBytes, are expected on disk per year. A very interesting new type of network structure called “GRID” is being developed to handle and distribute the data output from the detector over the internet to local computing centers around the world.

2) Simulating the Experiment: A multibillion dollar accelerator like the LHC is not constructed without detailed prior studies of its capabilities. In present-day high energy experiments, an enormous amount of more or less well understood physical processes occur from the initial state in time when two particles approach each other at ultra-relativistic speeds inside the beam pipe of some high-energy accelerator to the point, after the interaction, when particle tracks, energy depositions, detector status etc. are read out from the detector whose purpose it is to record as detailed information as possible about the ‘event’ that has taken place. Furthermore, the probabilistic nature of quantum mechanics ensures that any given initial state can result in a truly enormous number of possible final states. It is therefore a central and highly non-trivial task for the experimentalist to reconstruct what *actually* happened in each event recorded, and to design a detector that enables a distinction between “interesting” and “uninteresting” events, i.e. events that possibly contain traces of what is being searched for and events where only “trivial” processes have occurred. Simply constructing a machine capable of producing new particles is not enough - one must also be sure that one can actually *see* that the new particles were there. The theorist faces similar problems. To enable a comparison with experiment, the theory must deliver predictions of experimental observables. It is therefore not enough simply to study and calculate the elementary interactions contained in a given theory; these are only very rarely directly visible to the experiment. In most cases, a full, analytical calculation (using pen and paper) of everything that goes on between some initial state and some final state is simply out of the question. The amount of physical processes that would have to be calculated is simply too enormous, and for many of them, we do not even have exact solutions of the underlying theory. It is here that Monte Carlo generators come into the picture. The power of computers to perform repetitive tasks according to specific rules combined with the statistical Monte Carlo method has become an indispensable tool in comparing theory with experiment. It is the aim of Monte Carlo generators like PYTHIA and detector simulations like *AtlFast* to provide computer simulated ‘events’ that mimic those which would be recorded in a real detector, allowing us to bridge the gap between high energy theories and high energy experiments.

In Monte Carlo generators, the elementary processes that occur and about which one wishes to extract information are dressed with all the ‘other things’¹ that occur before, during, and after the high-energy interaction, thus simulating a real interaction between physical particles. Add to this a simulation of how the detector apparatus works (*no* detector catches everything), and the generated event has all the likeliness of a real event,

¹Of course, what is noise and background to one physicist can be highly interesting phenomena to another.

except that in *this* case we have full knowledge of what the fundamental process was. It is then possible for the experimentalist to make his best guess on what went on, based on the output from the detector simulation, and compare that with what the generator says *really* went on. This can be done any number of times for any number of physics scenarios, and it is then possible to test the efficiency of the detector and data analysis before the experiment is constructed, enabling an optimization of detector design, particle identification algorithms etc. The limitation is, of course, that it is impossible to include *all* possible effects that can occur in a physical interaction, and so one should never blindly trust simulated results without a critical analysis of whether all important effects have been taken into account. Exercising caution on this point, Monte Carlo simulations can be extremely useful in interpreting observed phenomena, in constructing a good detector and in finetuning the analysis strategies used in the actual experiment. In this work, the PYTHIA Monte Carlo generator is used to simulate a special class of supersymmetric theories which were previously not available in the generator and its output is combined with a crude simulation of the ATLAS detector. The potential for ATLAS to find experimental evidence for these theories is then analyzed for several specific variants of the theories.

1.1 Outline

In section 2, a brief account of the theoretical considerations fuelling the widespread belief in supersymmetry is given, together with an introduction to that particular class of supersymmetric theories called R -parity violating which comprises the subject of this thesis. The details of the overall supersymmetric framework adopted in this work and the L -violating decays of supersymmetric particles together with their implementation in PYTHIA are discussed in section 3. In section 4, some technical aspects of the ATLAS detector are discussed, with some emphasis on the detector and reconstruction parameters as they appear in `AtlFast`.

Section 5 begins with a presentation of the mSUGRA points and L -violating scenarios chosen for the analysis. The main part of the analysis is then presented, beginning with proposals for trigger menus optimized for \cancel{L} -SUSY at “mid luminosity” running of the LHC (i.e. $L = 3 \times 10^{33} \text{cm}^{-2}\text{s}^{-1}$). Based on the events surviving these triggers, an analysis of the significance with which a discovery can be made at ATLAS for Lepton number violating mSUGRA scenarios is then presented, assuming 30fb^{-1} integrated luminosity, corresponding to one year of mid-luminosity running. This analysis begins with a presentation of various kinematical and inclusive variables on which loose cuts are made, designed to have a high acceptance for as many of the various scenarios investigated as possible. Processing the remaining events through neural networks trained to discriminate between SM and SUSY events yields the final event numbers used to estimate the discovery potential, i.e. the statistical significance with which a discovery can be made, for each of the 50 separate mSUGRA models investigated. These numbers, representing the main result obtained in this work, can be found in table 18.

Finally, in section 6, we give an outlook on work remaining to be done together with a summary of the main conclusions reached within the body of this thesis.

2 Supersymmetry

For the past twenty years, high energy physics has experienced a unique state of affairs. Following the revolutions of relativity and quantum mechanics in the early parts of the 20'th century, Dirac's theory of the electron, the discoveries of antimatter and neutrinos, and the discovery that hadrons (e.g. protons and neutrons) are composed of quarks, a unified framework describing the electromagnetic, weak, and strong interactions emerged in the 70's, the so-called Standard Model of particle physics.

For the past twenty years, this model has successfully explained and predicted an astounding amount of experimental data. Only one piece is missing: the Higgs boson. In the Standard Model, this boson must exist since the known particles would otherwise be massless, and so the Standard Model would fall if the Higgs does not exist. Due to the immense success of the SM, it is widely believed that it is only a matter of time until this last piece of the puzzle is found, yet such a discovery would as much mark the doom as it would mark the final verification of the SM. If a fundamental Higgs boson exists, deeper problems appear for which one must go beyond the SM to find a resolution. The most severe of these problems is known as the *hierarchy problem*, and we shall discuss it in detail in section 2.3.1. For now, it suffices to note that despite the great success of the SM, it contains many unexplained parameters and has internal inconsistencies which can only be resolved by a more general framework. The central question, if we are ever to identify the *nature* of this "New Physics", then becomes at what energy scale we will see the predictions of the Standard Model begin to fail. The answer to this lies in the hierarchy problem itself, and I shall summarize below why there is good reason to believe that this energy scale cannot be much higher than the scales which will be probed by high energy experiments over the next few decades. Several ideas have been proposed for what the new physics could be. The possibilities range from extending the Standard Model with new particles, new interactions, higher symmetries of one form or another, or new spatial dimensions. Of these, Supersymmetry has become by far the most extensively considered, and I shall present some of the reasons for this in what follows.

2.1 What *is* Supersymmetry?

Among the most fundamental properties of any physical theory are the *symmetries* which the theory respects, since symmetries are so intimately connected with the existence of conservation laws. One of the most fundamental theorems in both classical as well as quantum mechanics is the famous *Noether's Theorem* stating that for each symmetry which nature respects there exists a corresponding charge or current which must be conserved. Another reason that symmetries are of prime interest is that they provide connections between one part of the theory and another, namely the parts which the symmetry relates to each other. For these reasons, a crucial task has been (and is) to discover which symmetries are respected, or, if violated, to what extent, by nature. In very general terms, there are two possible kinds of symmetries: *internal* symmetries and *space-time* symmetries. The theory of relativity, for example, tells us that Lorentz invariance is respected as a symmetry in space and time. Rotational invariance, translational invariance, and temporal invariance are other examples of space-time symmetries in that all of them imply a symmetry between one spatio-temporal point and another. Dropping a ball today in Copenhagen and dropping it tomorrow in Tokyo, having first turned yourself by 90 degrees, should not affect the speed at which it hits the ground. In contrast, the symmetries which we believe

to be responsible for the natural forces are examples of internal symmetries. A familiar example is the invariance of the performance of an electrical circuit to a global change of phase. As can be gleaned from this example, internal symmetries have to do with degrees of freedom associated with the fields themselves and not space-time, c.f. the phase of the electric field. As is well known, the theoretical framework on which the Standard Model is built is quantum field theory where particles are viewed as *quanta* of a *field*. These fields possess internal degrees of freedom not unlike the phases just mentioned, and the existence of internal symmetries require that the physics be invariant under changes to these degrees of freedom. Such internal degrees of freedom which have no effect on physical observables are known as gauge degrees of freedom, and it was with the realization that gauge symmetries can give rise to the fields associated with the natural forces that quantum electrodynamics was first conceived. Turning now to Supersymmetry, it will be useful to keep the distinction between space-time and internal symmetries in mind.

The story of Supersymmetry began in 1967 when Coleman and Mandula [2] proved a very important theorem which now bears their name. It deals with what *kind* of space-time symmetries are at all possible in any quantum field theory, at least any theory where the particles interact. They found that our theories already contain their full share of bosonic space-time symmetries, the combination of which is described by the so-called Poincaré symmetry group. I shall come back to the significance of the word *bosonic*. Effectively, the existence of an additional symmetry of this type would constrain the degrees of freedom in any interaction so much that the equivalent to no interaction at all takes place. Such a non-interacting theory obviously has very little to do with the real, very interacting universe, and thus it ceases to be physically interesting. The Poincaré group already contains its full share of (bosonic) symmetries. But in the context of supersymmetry, the word *bosonic* becomes all-important. That a symmetry is bosonic is technical slang for a symmetry for which *the order* in which two transformations are performed cannot be distinguished, i.e. a symmetry whose generators commute. It is, for example, quite impossible to tell the difference between two sheets of paper, one first moved 1 cm and then moved 2 cm, the other first moved 2 cm and then moved 1 cm (in the same direction). They both end up in exactly the same place. Thus, translational invariance is an example of a bosonic symmetry. To get on to supersymmetry, note that the word bosonic is customarily used about one of the two fundamentally different types of spin a particle can have. Bosons have integer spins (0,1,2,...) while fermions have half-integer spins (1/2,3/2,5/2,...). This difference causes the two types of particles to behave in very different ways, and their mathematical description is, likewise, very different. Bosons can be described using ordinary, commuting complex numbers while fermions require a description based on anti-commuting numbers, so-called Grassmann numbers for which $BA = -AB$.

The case of fermionic symmetry generators in quantum field theory (i.e. anticommuting operators carrying half-integer spin) was considered in 1975 by Haag, Lopuszanski, and Sohnius [3]. Their discovery was that any number of *fermionic* symmetry generators could be introduced in the theory without ruining it, provided they satisfied a rather constrained algebra; an algebra they called the supersymmetry algebra².

These considerations found their motivation simply in understanding what symmetries were at all possible in a general, physical quantum field theory, and nothing was said as

²As usual, an “algebra” is simply a set of commutation (and anticommutation) rules between operators, in this case the generators of the usual space-time symmetries and the supersymmetry generators.

to whether these symmetries were actually realized in nature or not, yet since that time, supersymmetry (SUSY) has risen to become the most extensively considered extension of the current theory, the so-called Standard Model (SM) of particle physics. The motivations for believing that supersymmetry does indeed belong among the basic properties of Nature are many, and there is some reason to expect that we shall soon possess the ability to test this belief in high energy accelerator experiments around the globe, most notably at the future Large Hadron Collider (LHC) at CERN, scheduled to commence operations around 2006.

Supersymmetry has been extensively considered in the literature, and a wealth of good textbooks and reviews on the subject are readily available. Thus, for detailed discussions, the reader is referred to e.g. [4] or, for the more algebraically minded, [5, 6]. It is understood that this by no means represents an exhaustive list. In the present writing, I merely outline the most important motivations and properties of supersymmetry. For completeness, the most important alternatives are mentioned as well.

2.2 Properties of SUSY

As already mentioned, the operators generating SUSY transformations carry spin $\frac{1}{2}$. It should then not be surprising that they transform a spin state $|S\rangle$ into $|S \pm \frac{1}{2}\rangle$, implying that a fermion is transformed into a boson and vice versa. Supersymmetry is thus a symmetry between fermions and bosons, and unbroken supersymmetry implies (among other things) that these states have equal masses. The non-observation of supersymmetric particles to date therefore implies that supersymmetry must be a broken symmetry at our energy scales, if it exists at all. Otherwise we would have seen these “spin-partners” of the known particles long ago. How supersymmetry may be broken will be discussed in section 2.2.2, but first we must get slightly technical. Postulating for the moment that this symmetry really exists, which fields and interactions should the SUSY Lagrangian contain?

The first question to be addressed in answering this question is *how many* anticommuting SUSY generators one should introduce. To this there is a natural limitation. In 4-dimensional space-time, only one supersymmetry is allowed if the theory is to have parity violation and chiral fermions. Violation of parity symmetry, or space-inversion, was first established by Wu et al. in 1957 with the famous measurement that the electrons emitted in β decay of Cobalt-60 nuclei are correlated with the nuclear spin direction, a parity non-invariant situation [7]. Chiral fermions means fermions that come with definite *handednesses* as we know it from the SM. Theories with only one supersymmetry are known as $N = 1$ SUSY, and in the rest of this text, I let $N = 1$ be implicit when talking about supersymmetry. We are now left with *one* supersymmetry whose spin $\frac{1}{2}$ generators are customarily denoted Q and Q^\dagger [5], i.e.

$$Q|\text{boson}\rangle = |\text{fermion}\rangle \quad \text{and} \quad Q|\text{fermion}\rangle = |\text{boson}\rangle \quad (1)$$

That a theory is supersymmetric simply means, in all generality, that these operators leave its Lagrangian invariant – that the physics is the same before and after particles and superpartners are interchanged.

The next question to consider is what the particle content of the theory looks like; what kind of multiplets should we include? A “multiplet” of a symmetry simply denotes a collection of any number of fields which are transformed into each other by the symmetry such that one never goes “outside” the multiplet by acting with the symmetry operators.



Figure 2: A graphical illustration of supermultiplets. a) The fermion and the scalar in a chiral supermultiplet. b) The vector boson and the fermion in a vector supermultiplet. Both are related to each other by a supersymmetry transformation.

If there is only one field (which is then, itself, invariant to the symmetry operation), one speaks of a singlet. If there is a pair of fields which are transformed into each other, one speaks of a doublet, etc. For brevity, and to avoid a (technical) repetition of a well-known issue, the reader is referred to [8] for details regarding supermultiplets. For our purposes, it suffices to note that ($N = 1$) supersymmetric theories can be built up from just two types of fundamental multiplets: *gauge* (or *vector*) multiplets and *chiral* (or *matter*) multiplets. A chiral multiplet contains a chiral (i.e. left-handed or right-handed) fermion together with a complex scalar. This is illustrated in figure 2a. Thus, the fermions of the SM can be accommodated in chiral supermultiplets, each receiving a scalar SUSY partner called *squarks*, *sleptons*, and *sneutrinos* where the ‘s’ is short for scalar. A gauge multiplet contains a vector boson together with a chiral fermion (fig. 2b). The gauge bosons of the SM can thus be accommodated in gauge supermultiplets with the requirement that they each have a supersymmetric fermion partner (the so-called *gauginos*). So far, each SM field (excepting the Higgs - see below) has been put inside a multiplet with one other field, and so we have arrived at an exact doubling of the SM particle spectrum. More supermultiplets could of course exist where *both* fields have not been seen experimentally, yet I here restrict the attention to the minimal model where only those multiplets that are strictly necessary are included.

The Higgs sector is slightly more complicated and deserves some mention. Due to the Higgs being a scalar, it can only reside in a *chiral* supermultiplet together with a fermion which would have hypercharge $Y = \frac{1}{2}$ or $Y = -\frac{1}{2}$. This might sound very innocent, but in fact, it is a disaster. Together with the third component of weak isospin, T_3 , the hypercharge assignments of the SM particles uphold a delicate balance where the traces $\text{Tr}\{Y^3\}$ and $\text{Tr}\{T_3 T_3 Y\}$ are both zero when taken over all fermions. Introducing new, non-zero hypercharge spoils that relation, giving rise to an anomaly [9] which would lead to unphysical divergences in the theory. If, however, *two* Higgs supermultiplets are introduced with different hypercharge signs, the cancellation is reestablished, and so there must be at least two Higgs (super-) doublets for SUSY to work. Indeed, the requirement of two Higgs doublets finds its motivation from two other sources as well; if the Lagrangian is to respect supersymmetry and gauge invariance of hypercharge, the coupling of the ordinary Higgs doublet to up-type quarks is forbidden. Thus, two Higgs multiplets are needed to provide mass terms for both up- and down-type quarks (and leptons) [10]. Also, two Higgs doublets are needed to provide all the SU(2) gauge bosons and their superpartners with masses.

This completes the specification of the minimal particle content for a supersymmetric extension of the Standard Model. In this work, we shall consider exclusively that version

NAME	SPIN 0	SPIN 1/2	SPIN 1	SUPERFIELD NOTATION
squarks & quarks (3 families)	$(\tilde{u}_L \ \tilde{d}_L)$	$(u_L \ d_L)$	-	Q
	\tilde{u}_R^*	u_R^\dagger	-	\bar{u}
	\tilde{d}_R^*	d_R^\dagger	-	\bar{d}
sleptons & leptons (3 families)	$(\tilde{\nu} \ \tilde{e}_L)$	$(\nu \ e_L)$	-	L
	\tilde{e}_R^*	e_R^\dagger	-	\bar{e}
Higgs & higgsinos	$(H_u^+ \ H_u^0)$	$(\tilde{H}_u^+ \ \tilde{H}_u^0)$	-	H_u
	$(H_d^0 \ H_d^-)$	$(\tilde{H}_d^0 \ \tilde{H}_d^-)$	-	H_d
gluino & gluon	-	\tilde{g}	g	-
winos & W bosons	-	$\tilde{W}^\pm \ \tilde{W}^0$	$W^\pm \ W^0$	-
bino & B boson	-	\tilde{B}^0	B^0	-

Table 1: Supermultiplets in the MSSM. The states appearing in each supermultiplet are collected in “superfields” in section 3 when Lagrangians are written down.

of SUSY known as the Minimal Supersymmetric Standard Model (MSSM) (albeit with the modifications that \mathcal{R} introduces) which only contains the SM particles (plus one additional Higgs doublet) together with their superpartners. This choice is made due to the relative simplicity of the MSSM and due to the lack of any real motivation for introducing more multiplets than absolutely needed. The total particle content of this model (with the superfields to which each particle belongs) is shown in table 1.

2.2.1 Sparticles and Mixing

As is familiar from the SM, the spectrum of physical particles (mass eigenstates) is not necessarily identical to the set of states appearing in the interaction Lagrangian (current eigenstates). In general, particles whose conserved quantum numbers are identical will mix with each other. The well-known phenomenon of quark mixing (see e.g. [11]) such as causes $K - \bar{K}$ and $B - \bar{B}$ mixing provides an important example of this. When extending the SM with SUSY particles, more mixing appears, and it is important that the conventions and nomenclature are firmly established before calculations are carried out. The conventions employed in SPYTHIA, HERWIG, and ISASUSY can be found in Appendix A for reference.

Scalars: Both the left-handed and right-handed versions of the SM quarks and leptons have scalar SUSY partners. Yet due to their scalar nature, it is impossible for these particles to possess any intrinsic ‘handedness’ themselves. The only difference between e.g. the \tilde{e}_L and the \tilde{e}_R is that they belong to different supermultiplets. Apart from that, they have exactly the same quantum numbers, and so they can mix with each other. In the language of ordinary quantum mechanics, we are dealing with a 2-fold degenerate subspace of states. Of course, any two orthonormal states will provide us a basis for this space, yet two physically motivated choices suggest themselves: the L - R basis and the *mass* basis, the former being a description in terms of current eigenstates and the latter in

terms of the mass eigenstates, \tilde{e}_1 and \tilde{e}_2 . Assuming for simplicity that there is no mixing between sfermions of different generations (see below), there appears a 2×2 mixing matrix between the mass and current eigenstates for each sfermion pair, \tilde{s} (in the convention of [12, 13]):

$$\begin{pmatrix} \tilde{s}_L \\ \tilde{s}_R \end{pmatrix} = \begin{bmatrix} \cos \theta_s & + \sin \theta_s \\ - \sin \theta_s & \cos \theta_s \end{bmatrix} \begin{pmatrix} \tilde{s}_1 \\ \tilde{s}_2 \end{pmatrix} \quad (2)$$

In a model without right-handed (SM) neutrinos, there is of course only one $\tilde{\nu}$ for each generation (i.e. no sneutrino mixing).

As mentioned, it is the *current* eigenstates (the chiral SM fields and their superpartners, $\tilde{s}_{L,R}$) which appear in the interaction Lagrangian. Since it is not these states but rather the mass eigenstates (being eigenstates of the Hamiltonian and thus of the time-development operator) which propagate through spacetime, one is most often interested in calculating production and decay properties of *mass* eigenstates³, resulting in the appearance of mixing factors in the matrix elements in section 3. A more general calculation taking inter-generational mixing into account can be found in [15], yet the magnitude of such mixing is highly constrained by the non-observation of large Flavour Changing Neutral Current rates and so we shall discount this possibility here (Flavour Changing Neutral Currents are quark transitions where the quark flavour changes, but the charge does not. The lowest order SM contributions are loops containing virtual, heavy particles, and so new physics effects (new loop particles) would enter at the same order in the couplings and thus could be extremely visible).

Neutralinos: There are four neutral fermions in the MSSM: the partners of the neutral U(1) and SU(2) gauge bosons, \tilde{B}^0 , \tilde{W}^0 (or, equivalently, $\tilde{\gamma}$, \tilde{Z}), and the partners of the two neutral Higgs scalars, \tilde{H}_u^0 , and \tilde{H}_d^0 . These states mix to form the four mass eigenstates $\tilde{\chi}_1^0$, $\tilde{\chi}_2^0$, $\tilde{\chi}_3^0$, $\tilde{\chi}_4^0$. In analogy with the scalar case, the mixing is parametrized by a 4×4 mixing matrix, N_{ij} [16]:

$$\begin{pmatrix} \tilde{\chi}_1^0 \\ \tilde{\chi}_2^0 \\ \tilde{\chi}_3^0 \\ \tilde{\chi}_4^0 \end{pmatrix} = N_{ij} \begin{pmatrix} -i\tilde{B}^0 \\ -i\tilde{W}^0 \\ \tilde{H}_u^0 \\ \tilde{H}_d^0 \end{pmatrix} \quad (3)$$

Note that [16] uses the notation $\lambda' = B^0$ and $\lambda^3 = W^0$. The analogous mixing matrix, N' , for the $(\tilde{\gamma}, \tilde{Z}, \tilde{H}_u^0, \tilde{H}_d^0)$ basis can be obtained simply by rotating the \tilde{B}^0, \tilde{W}^0 components by the Weinberg angle (see e.g. [17]) so that:

$$N'_{j1} = N_{j1} \cos \theta_W + N_{j2} \sin \theta_W \quad (4)$$

$$N'_{j2} = -N_{j2} \sin \theta_W + N_{j1} \cos \theta_W \quad (5)$$

Depending on what coupling is considered one may see either of these used in the literature. This should not lead to confusion when keeping in mind that N and N' express the same mixing, albeit on different bases.

³An important exception is in neutrino physics where one stays in the current state basis and mixing is replaced by oscillation. See e.g. [14].

Charginos: The charginos, $\tilde{\chi}_i^\pm$ ($i = 1, 2$), are defined as the mass eigenstates arising from the mixing of the charged Winos and Higgsinos. Naturally, states of different electric charge cannot mix, and so two separate mixing sectors appear [16]:

$$\begin{pmatrix} \tilde{\chi}_1^+ \\ \tilde{\chi}_2^+ \end{pmatrix} = V \begin{pmatrix} -i\tilde{W}^+ \\ \tilde{H}_u^+ \end{pmatrix} \quad \begin{pmatrix} \tilde{\chi}_1^- \\ \tilde{\chi}_2^- \end{pmatrix} = U \begin{pmatrix} -i\tilde{W}^- \\ \tilde{H}_d^- \end{pmatrix} \quad (6)$$

2.2.2 Supersymmetry Breaking

It was stated above that supersymmetry must be broken since unbroken supersymmetry implies an unobserved mass degeneracy between each SM particle and its respective superpartner. An important part of constructing a viable supersymmetric model is therefore to specify some model for *how* supersymmetry is broken. At present, this issue is unresolved and there is no outlook to convergence on any one model in the near future. At first glance, a spontaneous breaking mechanism would probably seem most natural, yet it is generally very difficult to obtain an acceptable mass spectrum in such models. The problem is that while the superpartner of *one* of the chiral states of the SM fermions is heavier, the superpartner of the other chiral state tends to be *lighter* than its SM counterpart, again in contradiction with the experimental non-observation of SUSY particles. Several more or less well-motivated alternatives exist: Explicit (soft) breaking, Supergravity (SUGRA), Anomaly-mediated SUSY breaking (AMSSB), and Gauge-mediated SUSY breaking (GMSSB). We shall here focus on the most popular model, the minimal Supergravity model (mSUGRA).

In Supergravity models, supersymmetry is imposed *locally* rather than globally. The resulting gauge field is interpreted as the gravitational one - an economic solution since it introduces only a field we already know might exist, the gravitational one, to break supersymmetry. The model is an example of a more general class of breaking mechanisms called “hidden sector breaking models” where supersymmetry is broken by some unobservable (called “hidden”) physics which only interacts with “the visible sector” (i.e. you, me, and all fields which we can interact with) through some “messenger field”, in this case gravity. This keeps the breaking flavour-blind as required from the absence of low energy Flavour Changing Neutral Currents and, since gravity is weak, it keeps the degree of breaking small which is generally required if Supersymmetry is to solve the hierarchy problem (see below). Adopting this scenario in phenomenological applications, a number of further assumptions are usually made, as will also be the case in the present work. They find their inspiration in Grand Unified Theories (GUTs) by which one justifies the plausibility of setting classes of masses and couplings equal at the GUT scale, and after the inclusion of which one prepends a small “m” (for *minimal*) to the SUGRA name. Some theorists argue against this practice due to generally declining interest in GUTs, yet it is often the only practically feasible thing in view of the the several hundred dimensional parameter space one would otherwise face. What is needed in order to specify a complete mSUGRA model is just five parameters:

1. m_0 : A common mass for all scalars in the theory, i.e. sfermions and higgs scalars, at the GUT scale.
2. $m_{\frac{1}{2}}$: A common mass for all fermions in the theory, i.e. the SM fermions, the gauginos, and the higgsinos, at the GUT scale.

3. A_0 : A common trilinear coupling (trilinear just meaning that three fields are coupling together).
4. $\tan\beta$: The ratio of vacuum expectation values for the two Higgs doublets. Its value is constrained between approximately 5 and 40.
5. $\text{sign}(\mu)$: μ is the mass parameter for the higgsinos. In general, this parameter could have an arbitrary complex value [8], but a non-vanishing imaginary part generally results in large, unobserved low energy CP violating effects, the most severe being an electric dipole moment for the neutron. It is therefore customary to assume μ real, with only the sign remaining to be specified since the magnitude is given by the other parameters.

One should note that the choice of basis is not unique, and so one often sees slightly different quantities parametrizing the space. It remains, however, that the degrees of freedom are inherently four real numbers and one sign. Graphically speaking, these parameters describe the physics we would see if we could probe the ultra-short GUT length scales. At lower energies, the physics “looks different”, in analogy with the shielding of the electron charge by quantum fluctuations very near the charge. The physics at different length/energy scales is related by the procedure of renormalization, specifically the famous Renormalization Group Equations (RGE’s). In mSUGRA (and in any other high-energy field theory), these equations are used to evolve the parameters from the input scale down to the observable scale. In physical language, the quantum fluctuations (loops) which are too highly energetic to be resolved by the probing energy ($\mathcal{O}(1\text{ TeV})$ for the LHC) are “put inside” the masses and couplings, causing each parameter of the theory to be a function of the energy scale. This is the reason one speaks of “running” couplings and masses. In this work, the minimal supergravity scenario will be assumed with the additional condition that $A_0 = 0$, mainly to limit the dimensionality of the SUSY parameter space, yet a small study of the consequences of this assumption is also performed (see section 5). For each of the scenarios studied, the input parameters along with the mass spectrum at the electroweak scale are given in table 4 in section 5.

2.3 Motivations for SUSY

2.3.1 The Hierarchy Problem

When attempting to lend credence to an extension of the Standard Model, it is perhaps of importance to note that the SM by itself cannot be quite right. Although the theory is in truly astonishing agreement with experiments at the hitherto accessible energy scales, the SM Higgs sector poses important problems when extrapolating the theory to higher energy scales. Virtual particles coupling to the Higgs field yield corrections to the Higgs mass squared which depend quadratically on the momentum cutoff used to regulate the theory. The only physical interpretation that can give meaning to such a cutoff is that it represents the energy scale at which some new physics steps in to halt the divergent behaviour. At the Planck scale, *some* new physics *must* step in, as this scale by definition is the scale at which quantum gravity effects become sizeable (at least in 4 dimensions), but if the ultimate validity scale of the Standard Model is interpreted as either the Planck scale (10^{19} GeV) or some other very large energy scale, then, naturally, the quantum corrections to the Higgs mass would make it nowhere near the electroweak scale. However, the Higgs mass *must* be of order the electroweak scale: if the theory is to be perturbative for W

and Z bosons, m_H must be less than about 1 TeV (see e.g. [18]), and from below, the theoretical limit from vacuum stability, $m_H > 1 \text{ GeV}$ [18], has been superseded by the LEP limit, $m_H > 113 \text{ GeV}$ [19]. The discrepancy between these two fundamental scales of Nature is known as the *hierarchy problem*. How can the electroweak mass scale be so low when the Planck scale is so high?

In a supersymmetric scenario, the hierarchy problem would exist no more as long as the mass differences between SUSY particles and SM particles do not exceed $\mathcal{O}(1 \text{ TeV})$ [20]. Since the supersymmetric particles by construction have the same couplings as their SM counterparts, every correction to the Higgs mass from an SM particle would receive an identical contribution from a supersymmetric particle, but with opposite relative sign (due to the sign difference between fermions and bosons), and thus the quadratic divergence is cancelled. When SUSY is broken, this cancellation is not exact (the masses are not the same), and so the cutoff mentioned above is effectively replaced by the SUSY breaking mass scale. If this scale is close to the electroweak scale ($M_{\text{SUSY}} \leq \mathcal{O}(1 \text{ TeV})$), then so would the Higgs mass be, in accordance with experiment. Note that it is only the technical part of the hierarchy problem which is solved by this. The electroweak scale can be made stable, but there is no explanation for its actual size. Supersymmetry only began to gain widespread acceptance around 1981/82 when a mechanism was discovered [21] which could generate the large gap between M_X and m_{EW} in a natural way: radiative breaking of electroweak symmetry. The Higgs mass parameter squared which enters the Higgs potential starts out positive at the GUT (or Planck) scale, but via radiative (= loop and therefore suppressed) corrections it is gradually driven smaller and smaller until it finally drops below zero, triggering the symmetry breaking. If this mechanism is the one used by Nature, then the two fundamental scales are connected by an exponential relation (see e.g. [22]), giving a natural explanation for their wide separation.

Some recent alternative solutions to the hierarchy problem which should be noted are the brane world scenarios in which the SM fields, excepting gravity, are confined to a 4-dimensional subspace (a “3-brane”) in a higher-dimensional world. Two dominant models exist. The first [23] forces the Planck scale down by simply introducing large extra dimensions. The high effective Planck scale $M_P = \sqrt{\hbar c/G}$ is then interpreted as being due to the spreading of gravity in more dimensions, causing the G we measure to be lower than the fundamental gravitational coupling, and so the fundamental Planck scale could be much smaller, possibly of the order of the electroweak scale, nullifying the hierarchy problem. Another important scenario has a single small extra dimension [24] where an exponentially decaying scale factor (the *warp factor*) in the extradimensional geometry is used to explain M_P/M_W . With two branes (one of which contains the SM fields) spaced some distance apart in this “fifth dimension”, the warp factor would cause an exponentially different length scale between the two, generating the weak scale and the Planck scale in a natural way. One could raise the objection that what is done in this model is simply to state that while M_P/M_W is a very large number, the logarithm of that number is much smaller, and so more “natural”. This may not be a wrong approach, but in this model, one still needs to justify why the slightly unnatural exponential appears in the extradimensional geometry, and so the hierarchy problem seems to be only partly solved by this model, in close analogy with what was the case for SUSY before radiative symmetry breaking was invented. References to other extradimensional models for explaining the hierarchy problem can be found in [25]. It should be noted that while these scenarios do not as they stand require SUSY, there is good reason to believe that branes and SUSY do go together. The brane scenarios do not themselves include a description of quantum

World Average	0.2312	± 0.0002	[29]
SM GUT	0.206	± 0.01	[30]
SUSY GUTs	0.196	$- 0.262$	[31]

Table 2: $\sin^2 \theta_W$ – measured value and predictions from supersymmetric and SM GUTs.

gravity, and thus they must be embedded in a larger, more fundamental framework. The most plausible of these at present being superstrings (see below), it does seem that branes are likely to indirectly require SUSY. For recent (legible) discussions on embedding branes in superstring scenarios, see [26, 27]. In this work, the effects of an eventual higher dimensionality of the underlying theory are assumed negligible.

Yet another alternative solution to the hierarchy problem is provided by the so-called Technicolour models which nullify the problem by simply not having a Higgs scalar at all (see e.g. [28]). These models are rather ill-favoured at present, and so I omit a presentation of them here.

2.3.2 Other Motivations

In GUT scenarios, one imagines that the gauge groups of the SM unify at some high energy scale. Extrapolating the SM itself to these scales does not result in a unification of the gauge couplings whereas the introduction of supersymmetry can produce exact coupling unification. On the experimental side, SUSY GUTs received a great amount of attention when the measurement of the weak mixing angle, θ_W , at LEP was found to be in agreement with predictions based on supersymmetric SU(5) GUTs, but not with predictions from SM-based GUTs, as shown in table 2. Thus, from a GUT viewpoint, supersymmetry is well motivated. One must keep in mind, though, that the simple MSSM (with R -parity conservation) gets in conflict with proton decay when embedded in the most general GUTs. This is not the case for SUSY with e.g. baryon number conservation, as will be discussed in depth in section 3.1. Going one step higher in energy (and one step deeper into speculation), conventional string theory was found to contain unphysical anomalies which are cancelled when the theory is made supersymmetric (hence the “super” in superstrings), and thus also in string theory, supersymmetry finds a possible motivation.

From a purely theoretical viewpoint, SUSY finds one more motivation. The essence of the Haag-Lopuszanski-Sohnius theorem [3] is that the largest symmetry possible in an interacting field theory is the combination of some internal gauge symmetries and (possibly local) supersymmetry (where supersymmetry here includes the usual Lorentz group). The gauge symmetries can of course be arbitrarily complicated, but the Lorentz group can only be extended with supersymmetry. It is then possible to make a (very) loose argument that the theory, in the absence of evidence to the contrary, should be of the most general type possible and thus include supersymmetry.

The last indication I shall be concerned with is the light Higgs scenario which has received an explosion of interest caused by a few events in the LEP 2 data sample. Assuming (a discussion of the justification of this assumption is beyond the scope of this work) that the LEP results of $m_H = 115 \text{ GeV}$ are confirmed or that some other not much greater Higgs mass is found, the effective SM Higgs potential becomes unstable at $\mathcal{O}(10^6) \text{ GeV}$, resulting in an unobserved instability of the electroweak vacuum [32]. When supersym-

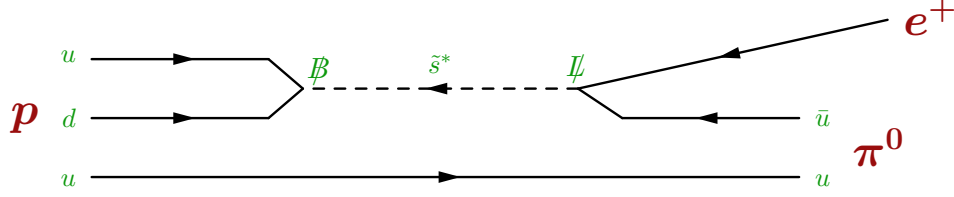


Figure 3: Proton decay, $p \rightarrow \pi^0 e^+$, via one baryon number violating vertex and one lepton number violating vertex through the propagation of a (heavy) sparticle. On a more general note, it is not difficult to realize that something baryonic has to change into something leptonic for proton decay to be kinematically allowed, and so L and B *must* both be broken for this to happen.

metry is introduced, a light Higgs boson does not lead to this instability, and so a light Higgs would be suggestive of the existence of supersymmetry. This scenario is presently awaiting confirmation from the Tevatron and the LHC.

2.4 *R*-breaking Supersymmetry

In the above, I have essayed to outline the most important motivations for supersymmetry. There is, however, a snake in this apparent paradise which immediately makes its presence known; the most general SUSY Lagrangian is utterly incompatible with experiment. It contains renormalizable Lepton and Baryon number violating interactions [9] which, being suppressed only by $\frac{1}{(\text{sparticle mass scale})^2}$ (from the propagation of heavy SUSY particles, see fig. 3), result in a proton lifetime much lower than the experimental limit of $\tau_{\text{proton}} \geq 10^{31} \text{ yr}$ [29]. The bounds on the B and L violating couplings from this measurement are so strict that at least one of them must be almost exactly zero [33]. The only natural way for this to come about is if there were a symmetry in the theory that would exactly forbid these reactions. Thus, in a supersymmetric scenario, there must be some extra symmetry to protect the proton, but *which* symmetry? A very sober discussion of this question can be found in [34]. Generally, there are three types of discrete symmetries which draw special attention to themselves; R -parity, B -parity (Baryon parity), and L parity. They will be discussed in detail in section 3.1. The latter two are slightly favoured since B and L violating operators of dimension 5 from supersymmetric GUT- and string-inspired models must be extremely suppressed relative to their “natural” values in the R -parity conserving models [35], requiring the introduction of additional symmetry, whereas both B and L parity automatically forbid all relevant baryon or lepton number violation, respectively. However, R -parity is considered much more often in the literature due to its providing a natural dark matter candidate and due to its comparatively much simpler phenomenology.

In order to outline the difference, the dominant aspects of R -conserving phenomenology are now briefly described. As the name suggests, the Lagrangian is required to be invariant under a discrete symmetry known as R -parity [36]:

$$\hat{R}\mathcal{L} = \mathcal{L} \quad (7)$$

where \hat{R} is an operator acting on products of fields by returning the product of the R -parities of each field (i.e. R -parity is a multiplicative quantum number) defined by:

$$R = (-1)^{3B+L+2S} \quad (8)$$

Here, B (L) is baryon (lepton) number, and S is the spin. Due to the $\frac{1}{2}$ spin difference between SM and SUSY fields, the SM fields have $R = 1$ whilst the SUSY particles have $R = -1$. With the requirement that the Lagrangian be invariant under R , all combinations of fields which change sign under this operation are forbidden. This clearly implies that SUSY fields must always come in pairs (since $-1 \times -1 = +1$). Furthermore, as the B and L violating terms appearing in the general SUSY Lagrangian are without exception *odd* under R (see e.g. [33]), they are forbidden by this symmetry, and thus the proton is saved. In addition to this, a dark matter candidate is gained: the decay chain of any sparticle ends with an odd number of the so-called Lightest Supersymmetric Particle (LSP) which is stable (and neutral, for cosmological reasons). Being heavy, it is an ideal candidate for the dark matter type known as Weakly Interacting Massive Particles (WIMPs). The experimental searches for R conserving scenarios thus rely on pair production and missing energy (from LSP's escaping the detector) as strong signals.

The most important differences that should be noted between R conserving and R breaking phenomenologies have to do with the LSP. In \mathcal{R} the LSP can decay, often with a lifetime short enough for the decay to proceed inside the detector, and thus the missing energy signal can be greatly diminished. In addition, there is no longer any requirement from cosmology that the LSP should be neutral, and so the list of possible LSP candidates becomes larger. It should be mentioned, though, that while R -breaking generally results in the loss of the LSP as a dark matter candidate, viable R -breaking models exist in which the LSP is a gravitino having a lifetime longer than the age of the Universe, thus restoring its validity as a dark matter candidate [37]. This open question must be resolved by experiment.

2.4.1 Experimental Indications of R -Violation?

Neutrino Masses: Combining the measurements of the Super-Kamiokande detector in Japan [38] with the very recently published (June 2001) results of the Sudbury Neutrino Observatory in Canada [39], one now has conclusive evidence for the existence of neutrino oscillations, implying non-zero neutrino masses. This would mean that lepton family number and/or total lepton number is not conserved (Lepton family number is broken by Dirac mass terms while total lepton number is broken by Majorana mass terms. For a description of the difference, see [14]). The exact nature of the mass (Dirac or Majorana) is difficult to determine. The most commonly used technique is to search for neutrinoless double β decay of nuclei, since this process is forbidden unless there is a Majorana neutrino. These experiments are not easy, however, and the determination of the nature of the neutrino mass will most likely have to wait for at least another generation of neutrinoless double β decay experiments. On the theoretical side, neutrino mass models are enormously abundant at present, and there is no outlook to consensus in the near future. In connection with R -parity violation, I merely note that Majorana masses can arise from one-loop self-energy diagrams containing SUSY particles with \mathcal{R} couplings. The resulting mass hierarchy is not well constrained, but at least a neutrino mass pattern consistent with both atmospheric and solar neutrinos can be generated (see e.g. [40, 41]). There are, however, no strong arguments either for or against this hypothesis. Naturally small neutrino masses can arise in GUT- and string-inspired scenarios without breaking R -parity (see section 3.1). However, *if* there are Majorana neutrinos present (i.e. total lepton number broken), then Baryon parity still seems a good candidate for the proton-protecting symmetry (proton decay occurs only when B and L are violated *simultaneously*).

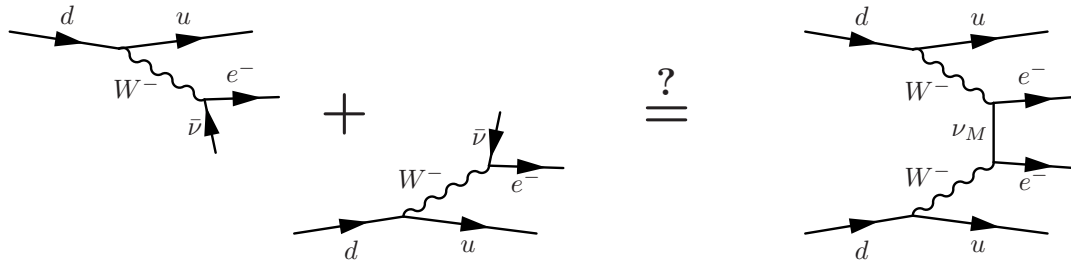


Figure 4: Combining two diagrams for ordinary β decay *cannot* result in neutrinoless double β decay since the arrow on the neutrino propagator cannot simultaneously point in both directions *unless* the neutrino is its own antiparticle (= a Majorana particle). Note: the two d quarks in the last diagram are imagined taken from two separate neutrons, and the “+” between the two first diagrams should not be taken too literally.

The HERA High Q^2 Anomaly: Part of the experimental programme for the H1 and ZEUS experiments at the HERA ep collider (which is currently under upgrading) is to search for so-called leptoquarks, meaning particles carrying quark as well as lepton quantum numbers. Although SUSY does not imply the existence of such particles, \mathcal{R} -SUSY can produce similar signatures in the detector due to the violation of lepton or baryon number. Before describing the anomaly, let us first explain what Q^2 means. This is the standard symbol for the momentum transfer squared in so-called Deep Inelastic Scattering (DIS, see fig. 5). At HERA, Q denotes the size of the momentum exchange occurring between the incoming electron or positron and the proton constituent it interacts with. The HERA High Q^2 Anomaly was an excess of events with a positron in the final

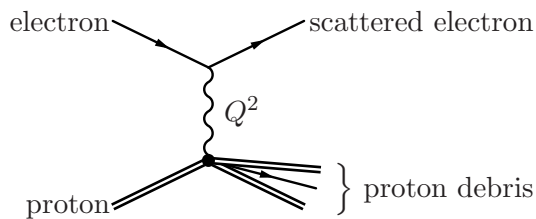


Figure 5: Illustration of Q^2 at HERA. As can be seen, this process is similar to ordinary scattering except that the proton here breaks up, hence the name Deep Inelastic Scattering.

state at high (previously unexplored) momentum transfers reported by the H1 and ZEUS collaborations at HERA [42, 43] based on e^+p data taken during 1994-1997. An unexpected bump (≈ 10 events) was seen in the jet-positron invariant mass around 200 GeV, with a small difference in the peak position between the two experiments. One interpretation of this excess was to ascribe it to the resonant production of a \tilde{u} squark in the process $e^+d \rightarrow \tilde{u}$ (see e.g. [44]) with the \tilde{u} decaying to a final state including a positron, and thus the signal could be interpreted as an indication of R -Violation. While this interpretation is still not completely excluded, further data did not support the hypothesis, and related processes which should occur in e^-p collisions (produced by HERA from 1997 till now) were not seen [45], and so the HERA High Q^2 Anomaly is at present relegated to one of history’s many statistical fluctuations.

The KARMEN Time Anomaly: The KARMEN experiment, designed to search for electron neutrinos appearing in $\nu_\mu \rightarrow \nu_e$ and $\bar{\nu}_\mu \rightarrow \bar{\nu}_e$ oscillations, while having found no evidence for oscillations, has found something else – evidence [46] for an unexpected anomaly in the time-of-flight distributions of pion decay products. The experiment works by shooting protons on a stationary target, giving pions which are quickly stopped in the target material. The decay $\pi^+ \rightarrow \mu^+ \nu_\mu$ then gives a source of mono-energetic muon neutrinos, and the subsequent muon decay $\mu^+ \rightarrow e^+ \nu_e \bar{\nu}_\mu$ provides the muon antineutrinos, these neutrinos on average being produced a muon lifetime, $2.2 \mu\text{s}$, later than the neutrinos from the pion decay.

In the time distribution, one thus expects to see an initial pulse (the ν_μ 's) at close to zero time after the proton pulse hits target, due to the short lifetime of the pion, followed by a smooth exponential falloff (the $\bar{\nu}_\mu$'s and ν_e 's) with a time constant characteristic of muon decay, $2.2 \mu\text{s}$. The surprise is that there seems to be sitting a small gaussian on top of this exponential falloff at around $3.6 \mu\text{s}$ after the beam hits target. This effect was first observed in 1995 and was since reconfirmed by a new run with improved shielding to protect against cosmic rays. It is thus not the case for this anomaly that its statistical significance has decreased. The first run resulted in 83 ± 28 events in the gaussian fit, and the second in a total of 103 ± 34 events [47].

The interpretation of the KARMEN collaboration is that the bump is due to the process $\pi^+ \rightarrow \mu^+ X^0$, where X^0 is some unknown particle which must be neutral since it survives through 7 metres of steel. Based on the measured time of flight, its mass must be 33.91 MeV , just below the kinematical threshold to produce it in pion decay at all. The likelihood analysis results in less than 1 to 10^4 chance that this is a statistical fluctuation. Several potential solutions can be excluded (see [48] for a brief review), yet two simple possibilities remain: sterile neutrinos and three-body neutralino decay through R -Violation, specifically the λ'_{211} coupling. In models like SUGRA in which the neutralino and chargino masses are related, the latter is already excluded from very stringent limits on chargino masses [48], but it *is* allowed in unconstrained supersymmetric models and is consistent with all experimental data as well as cosmological nucleosynthesis [49]. The experimental bounds are nicely reviewed in [50, chp.4] where both the limit from the invisible Z width and limits from precision electroweak measurements are discussed at a pedestrian level. Other collaborations have explored and excluded parts of the KARMEN signal region, yet “No experiment currently approved is likely to have sufficient sensitivity to confirm or rule out the X^0 ” [47]. This is where the case rests.

To conclude in as fair a manner as possible, there are in my opinion at present no significant experimental indications of either a conserved or a broken R -parity.

Having made these remarks, it is deemed likely that R -breaking supersymmetry will be of interest to experiments planning to explore SUSY at second generation accelerators such as the LHC. With the PYTHIA Monte Carlo generator being one of the most widely used, the motivation for the present work also becomes clear.

3 L-violating Decays of SUSY Particles

3.1 The Model

A brief list of the assumptions that underlie the specific scenario of \mathcal{R} -SUSY adopted in this work is now given, together with attempts to explain and justify each of them in turn. A considerable emphasis is given to the theoretical motivations for and against the various proton-protecting symmetries one can introduce, and several important yet often understated arguments are presented.

The particle content is that of the MSSM. In the absence of any experimental indications to guide us, the choice of minimal particle content is made strictly for reasons of simplicity.

Lepton number conservation is violated. Since this assumption is in some sense the crucial and somewhat controversial step taken in this thesis, I will present the arguments for it in some detail. Stated briefly, the advantage of abandoning R -parity in favour of e.g. baryon parity is that the MSSM then no longer comes in direct experimental conflict with proton decay when embedded in GUT scenarios.

As discussed above, simultaneous violation of both B and L would lead to fast proton decay, and so *some* additional symmetry must be introduced. The choice of taking lepton number violated and baryon number conserved in the supersymmetric interactions has been made for the following reason: in theories where a discrete symmetry (such as B , L , or R) arises from a broken, continuous gauge symmetry, there have been put forth strong indications [34] that only B and R do not lead to so-called ‘discrete gauge anomalies’ [51]. Here, a brief digression to explain the concept of an anomalous symmetry is probably in order.

We know from classical field theory that every symmetry of the Lagrangian implies the conservation of a corresponding current, the Noether current. When this conservation is not respected by quantum corrections, i.e. when the divergence of the Noether current is non-zero when calculating e.g. loop corrections, we speak of an anomaly. The fact that L -symmetry contains anomalies in some models simply means that even if we take the Lagrangian invariant under transformations generated by Lepton number, quantum corrections will not respect the conservation of this generator, and thus proton decay clearly *will* take place (this is still the case when L is a discrete symmetry [34]). We can then conclude that B and R are the strongest candidates *if* the symmetry that protects the proton is indeed the discrete remnant of some broken gauge symmetry. That this is most likely the case can be seen when taking quantum gravity effects into account.

It has been pointed out [52] that for any discrete symmetry which is *not* of gauge origin, the effect of taking wormholes into account is to produce an effective action at low energy which does not respect the selection rule arising from the symmetry. An intuitive example is that a group of particles in an R -odd state may be engulfed by a baby universe, causing a measurement in the parent universe to register a deficit of R . In more precise language, quantum mechanical tunneling, represented by the formation of a wormhole, can transport an R -odd state into a disconnected space (the baby universe) where it will not be measured. On the other hand, a very compact and elegant argument (see e.g. [53]) can be used to show that discrete *gauge* symmetries are absolutely stable under quantum gravity effects [54], i.e. proton decay *will not* be mediated even by quantum gravity effects if and

only if the symmetry has a gauge origin. From these arguments, taking the uncertainties involved in treating quantum gravity⁴ and my own lack of superior judgement on this point into account, I restrict myself to the conclusion that the discrete symmetry protecting the proton is *most likely* of gauge origin, and thus B and R parity are the preferred candidates.

That both R -conservation, B -conservation, and L -conservation should be considered is indisputable, but I will make the point that B - and L -parity seem to be more favoured from a GUT and string theoretical viewpoint: In quantum field theory, only operators of mass dimension ≤ 4 are renormalizable, and thus they are the only ones considered in ordinary applications. In theories which go beyond the SM where superheavy particles appear at some high mass scale (such as the GUT or string scale), non-renormalizable B and L violating operators, i.e. operators of higher mass dimensions, appear in the effective low-energy Lagrangian much like in the early EW theory of four-fermion interactions (see e.g. [9, 10]). These terms have forms like e.g. $\psi^2\varphi^2$, where the fermionic operator, ψ , has dimension $(\text{mass})^{\frac{3}{2}}$ and the scalar operator φ is of mass dimension 1. On dimensional grounds, noting that the terms in the Lagrangian must be of dimension 4 to give a dimensionless action, these operators will be suppressed by $d-4$ powers of the superheavy mass scale [55], and so they can safely be neglected in ordinary applications, yet due to the very strict bounds from proton decay, B and L violating operators of $d=5$ that appear in supersymmetric GUTs [56] are not sufficiently suppressed by even the Planck scale alone, and they will generate nucleon decay at an ‘unacceptable rate’ [34, 35] unless they are suppressed by several (7–8) orders of magnitude from their “natural” values, as defined by [35, eq. (17)].

Early arguments ran along the line of [10] that any supersymmetric GUT with R -parity will require a natural, but very accurate adjustment of parameters. In later analyses [34, 35] it is explicitly argued that both B and L conservation, *but not* R -parity conservation, can save the proton from higher-dimension B - and L -violating terms in Supersymmetric GUTs. It should be mentioned that in the B -parity case (where Lepton number is violated), decays such as $\mu \rightarrow e\gamma$ would not be expected to occur at rates above current experimental limits [35].

The main conclusion is that in any supersymmetric extension of the SM where baryon and lepton number violation can occur at *some* scale below the Planck scale with $d = 5$ operators in the effective Lagrangian that are not additionally suppressed ($d = 5$ operators are very hard to avoid in a supersymmetric scenario due to the many scalars), conservation of baryon number (and violation of lepton number) or conservation of lepton number in the supersymmetric interactions are possible, and R -parity is excluded. This means that practically the only chance for Supersymmetry to provide a natural Dark Matter candidate in such models is if the gravitino has a lifetime longer than the age of the universe.

From this discussion, it also becomes clear that R -conserving models can generate naturally small neutrino masses through higher-dimension operators suppressed by some large mass scale.

Inter-generational mixing of squarks and sleptons is neglected. The only mixing matrices that appear for the SUSY particles are the $\tilde{f}_L - \tilde{f}_R$ mixing matrices discussed above. This choice has been made due to the observed absence of large Flavour Changing Neutral Currents (see 2.2.1) and due to the SPYTHIA generator in its present form not being able to handle this kind of mixing.

⁴In [52], the author mentions that his method (summation over wormholes) may or may not be correct.

It is assumed that all SUSY decays happen on resonance. This is a more technical assumption to do with the decay treatment in PYTHIA (see section C.3). It means that all decay widths and consequent branching fractions of sparticles are only evaluated once (at the pole mass of the decaying particle) during program execution, saving considerable CPU time. This has the drawback that finer features of the decay distributions are integrated out and care has to be taken to ensure energy conservation when thresholds are present near the resonance.

In the analysis performed in section 5, minimal Supergravity will be assumed (see section 2.2.2), and the evolution equations of ISASUSY are used to evolve couplings and masses from the GUT scale to the electroweak. We make one additional simplifying assumption. The common trilinear coupling, A_0 , which controls the sfermion mixing sector is assumed vanishing. A study of the effects of non-zero A_0 was performed at points 2, 9, and 12 (see table 4 for the definitions of these points). Varying A_0 between 0 and 500 GeV did not result in significant changes of the semi-inclusive branchings (e.g. $\text{BR}(\tilde{\chi}^0 \rightarrow qq\nu)$) for the \mathbb{R} modes, and so the influence of this parameter on the frequency with which sparticles decay in L -conserving channels versus \mathbb{L} -channels is concluded minimal. Since this is primarily what determines whether we will be able to see \mathbb{L} -SUSY in our detectors, the impact of this assumption on the analysis presented in section 5 is likewise concluded minimal. It cannot be guaranteed, however, that this parameter may not shift the conventional SUSY discovery signals around between clean and less clean modes. It is clear that such effects cannot be taken into account by the present analysis.

3.2 The L -Violating Lagrangian

There are three lepton-number violating terms in the superpotential, one which is bilinear in the superfields and two which are trilinear. The bilinear term may be rotated away by a simple change of basis for the fields with no consequences on the physics, the choice of basis being arbitrary. This is advantageous for calculating lowest order decay rates such as we are interested in here. In other applications, such as loop calculations and renormalization group evolution, other bases are more appropriate (see e.g. [57]) to better keep track of the parameters or to obtain expressions for which experimental bounds are in more direct correspondence. In our basis, the superpotential takes on the form [13]:

$$W_{\mathbb{L}} = \frac{1}{2}\lambda_{ijk}\varepsilon^{ab}L_a^iL_b^j\bar{e}^k + \lambda'_{ijk}\varepsilon^{ab}L_a^iQ_b^j\bar{d}^k \quad (9)$$

where L and Q are the lepton and quark superfields respectively (see table 1), i, j, k are generation indices (e.g. e, μ , or τ for leptons) and a, b are $SU(2)_L$ indices (up-type or down-type, neutrino or charged lepton)⁵. From this potential, the following terms in the Lagrangian (corresponding to the Lepton number violating vertices in the theory) are obtained (see e.g. [5, 57]):

$$\begin{aligned} \mathcal{L}_{\mathbb{L}} = & \frac{1}{2}\lambda_{ijk} \left(\bar{\nu}_{Li}^c e_{Lj} \tilde{e}_{Rk}^* - e_{Li} \bar{\nu}_{Lj}^c \tilde{e}_{Rk}^* + \nu_{Li} \tilde{e}_{Lj} \bar{e}_{Rk} - \tilde{e}_{Li} \nu_{Lj} \bar{e}_{Rk} + \tilde{\nu}_{Li} e_{Lj} \bar{e}_{Rk} - e_{Li} \tilde{\nu}_{Lj} \bar{e}_{Rk} \right) \\ & + \lambda'_{ijk} \left(\bar{\nu}_{Li}^c d_{Lj} \tilde{d}_{Rk}^* - \bar{e}_{Ri}^c u_{Lj} \tilde{d}_{Rk}^* + \nu_{Li} \tilde{d}_{Lj} \bar{d}_{Rk} - e_{Li} \tilde{u}_{Lj} \bar{d}_{Rk} + \tilde{\nu}_{Li} d_{Lj} \bar{d}_{Rk} - \tilde{e}_{Li} u_{Lj} \bar{d}_{Rk} \right) \\ & + \text{hermitian conjugate (h.c.)} \end{aligned} \quad (10)$$

⁵Thus, e.g. $L_1^1 = (\bar{\nu}_e, \nu_e)$, $L_2^1 = (\bar{e}_L, e_L)$, $Q_2^2 = (\bar{s}_L, s_L)$, and $Q_1^3 = (\bar{t}_L, t_L)$.

All of these terms contain two (SM) fermions and one (SUSY) scalar, and thus the oddness under R is here directly visible. Also, it is clear that each scalar can decay in a number of ways to two SM fermions via these couplings. The neutralino and chargino decays (and for that sake gluino) must proceed via intermediate scalar particles, resulting in three-particle decays and interference between several contributing diagrams.

We begin by considering diagrams corresponding to the terms multiplied by λ_{ijk} (the first line in the above equation). These terms involve only non-coloured fields, and so they have more clean signatures relative to the λ' terms (the second line) where the strong interaction is at play. These terms will be treated in section 3.4.

3.3 Purely Leptonic Decays

One property that should be noticed about the λ coupling is that it must be antisymmetric in its first two indices, i and j . If λ is decomposed into a symmetric and an antisymmetric part, then it is easy to see that the symmetric part multiplied by $L_a^i L_b^j$ will be symmetric in a and b and thus will give zero when multiplied by ε^{ab} . This antisymmetry puts some restrictions on the number of possible decay channels.

3.3.1 Scalar Decays

The antisymmetry of the λ coupling can quickly be used to rewrite the first line of eq. (10) as:

$$\begin{aligned} \mathcal{L}_{\mathbb{I}}^\lambda = & \frac{1}{2} \lambda_{ijk} (\bar{\nu}_{Li}^c e_{Lj} \tilde{e}_{Rk}^* + e_{Lj} \bar{\nu}_{Li}^c \tilde{e}_{Rk}^* + \nu_{Li} \tilde{e}_{Lj} \bar{e}_{Rk} + \tilde{e}_{Lj} \nu_{Li} \bar{e}_{Rk} + e_{Lj} \tilde{\nu}_{Li} \bar{e}_{Rk} + \tilde{\nu}_{Li} e_{Lj} \bar{e}_{Rk}) \\ & + \text{h.c.} \end{aligned} \quad (11)$$

The purely leptonic decay modes allowed by the couplings in the above Lagrangian can then be read off:

1. $\tilde{e}_{j\alpha}^- \rightarrow \bar{\nu}_i \ell_k^-$ (terms 3 and 4)
2. $\tilde{e}_{k\alpha}^- \rightarrow \nu_i \ell_j^-$ (h.c. of terms 1 and 2)
3. $\tilde{\nu}_j \rightarrow \ell_i^+ \ell_k^-$ (terms 5 and 6)

where roman indices are generation indices and α runs over the two mass states of the sleptons.

It is well known from kinematics that the simple shape of the $1 \rightarrow 2$ phase space allows us to express the width of \tilde{a} decaying to b and c (see e.g. [29]) as:

$$\Gamma(\tilde{a} \rightarrow bc) = \frac{|\overline{M}(\tilde{a} \rightarrow bc)|^2 p_{CM}}{8\pi M_{\tilde{a}}^2} \quad (12)$$

with the final-state momentum in the decay rest frame

$$p_{CM}^2 = \frac{1}{4M_{\tilde{a}}^2} (M_{\tilde{a}}^2 - (m_b + m_c)^2) (M_{\tilde{a}}^2 - (m_b - m_c)^2) \quad (13)$$

The leading order matrix elements for these decays are excessively simple to obtain. An example showing a decay proceeding via the third term in eq. (10) is depicted in fig. 6a. The slepton mixing matrix giving the ‘left-handed’ part of the mass state \tilde{e}_{j2} is denoted by

$L_{12}^{\tilde{e}_j}$ (see section 2.2.1). A convenient and intuitive way of writing $|M|^2$ graphically which I would like to advocate is shown in fig. 6b with Feynman factors written explicitly for each particle and vertex (I follow the conventions of [58], using u for spinors representing particles and v for spinors representing antiparticles).

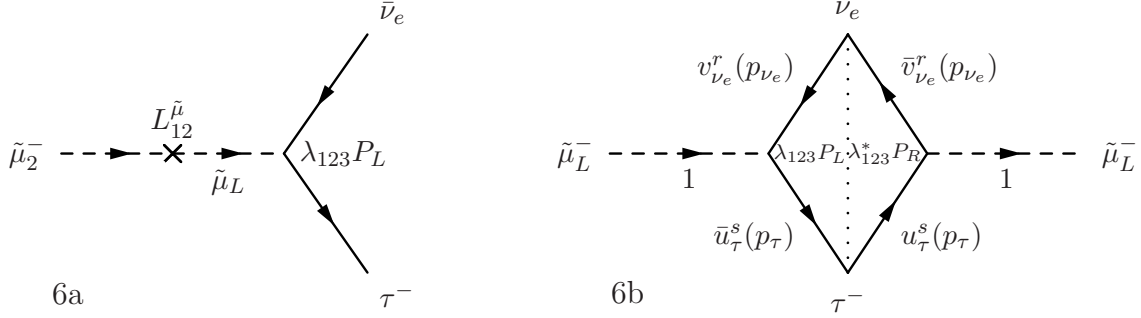


Figure 6: An example: a) the \not{L} decay of a slepton mass state to two leptons with the mixing shown symbolically as a cross. b) the folding of the diagram, for simplicity shown without the mixing factor.

Taking a look at figure 6b, we can simply write down $|M|^2$ for the process $\tilde{e}_{j\alpha}^- \rightarrow \bar{\nu}_i e_k^-$:

$$|M(\tilde{e}_{j\alpha} \rightarrow \bar{\nu}_i e_k)|^2 = |\lambda_{ijk}|^2 |L_{1\alpha}^{\tilde{e}}|^2 (\bar{u}_{e_k}^s(p_{e_k})(1 - \gamma_5)v_{\nu_i}^r(p_{\nu_i})) (\bar{v}_{\nu_i}^r(p_{\nu_i})(1 + \gamma_5)u_{e_k}^s(p_{e_k})) \quad (14)$$

where $i, j, k \in (e, \mu, \tau)$ and $\alpha \in (1, 2)$. Summing over the spin states of the outgoing fermions (and keeping the neutrino mass for generality) yields:

$$\begin{aligned} |\overline{M}(\tilde{e}_{j\alpha} \rightarrow \bar{\nu}_i e_k)|^2 &= |\lambda_{ijk}|^2 |L_{1\alpha}^{\tilde{e}}|^2 \text{Tr}\{(\not{p}_{\nu_i} - m_{\nu_i})\frac{1-\gamma_5}{2}(\not{p}_{e_k} + m_{e_k})\frac{1+\gamma_5}{2}\} \\ &= \frac{1}{2}|\lambda_{ijk}|^2 |L_{1\alpha}^{\tilde{e}}|^2 (p_{\nu_i}^\mu p_{e_k}^\nu \text{Tr}\{\gamma_\mu \gamma_\nu\}) \\ &= 2|\lambda_{ijk}|^2 |L_{1\alpha}^{\tilde{e}}|^2 (p_{\nu_i} \cdot p_{e_k}) \end{aligned} \quad (15)$$

Noting that $p_e \cdot p_\nu = \frac{1}{2}(M_{\tilde{e}}^2 - m_e^2 - m_\nu^2)$ we get the final form:

$$|\overline{M}(\tilde{e}_{j\alpha} \rightarrow \bar{\nu}_i e_k)|^2 = |\lambda_{ijk}|^2 |L_{1\alpha}^{\tilde{e}}|^2 (M_{\tilde{e}_j}^2 - m_{e_k}^2 - m_{\nu_i}^2) \quad (16)$$

Estimating the other matrix elements of this kind proceeds along exactly the same lines (also for \not{L} decays involving (s)quarks), resulting in the general form:

$$|\overline{M}(\tilde{a} \rightarrow bc)|^2 = C_{bc}^a (M_{\tilde{a}}^2 - m_b^2 - m_c^2) \quad (17)$$

where \tilde{a} can be any SUSY scalar, and the coefficients C_{bc}^a are given in [13]. This form of the matrix agrees with the result obtained in [13].

3.3.2 Kinematics and Phase Space Topologies

As none of the SUSY fermions have \not{L} couplings themselves, the leading order contributions to the \not{L} decays of neutralinos, charginos and gluinos proceed via intermediate scalar states with (for the purely leptonic processes) one L -conserving vertex where the SUSY fermion decays to a slepton-lepton pair and one \not{L} vertex where the slepton decays to two

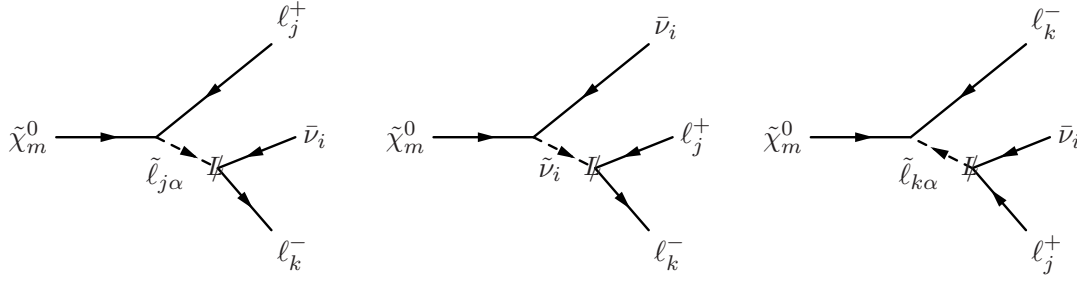


Figure 7: Feynman diagrams contributing to $\tilde{\chi}_m^0 \rightarrow \bar{\nu}_i \ell_j^+ \ell_k^-$. The index α runs over the slepton mass eigenstates, $\tilde{\ell}_{1,2}$. An explicit $//$ symbol adorns the vertices where the lepton number is violated.

leptons. An example, showing all contributions to the neutralino decay $\tilde{\chi}_m^0 \rightarrow \bar{\nu}_i \ell_j^+ \ell_k^-$ is given in figure 7. With α running over the two mass eigenstates of the sleptons, a total of five interfering diagrams enter the calculation of the squared amplitude. Combined with the more complicated phase space, the treatment becomes much more cumbersome than for the scalar decays in the previous section. The full calculations have been performed in [13], but one must take care when performing numerical integrations over kinematical variables as is typically the case in event generators. Therefore, a brief digression to define and comment kinematical variables is now appropriate.

Any quantum mechanical transition probability depends sensitively on the (energy-momentum) spectrum of the final states available for the system. In the continuous limit of free particle final states, this dependence is cast in the form of the Lorentz Invariant Phase Space, and we must now consider how to integrate over this space, as we wish to obtain the total widths of the decays we shall presently consider. In a general three-body decay occurring between unpolarized states, there are two kinematical degrees of freedom. For example, one can specify the sharing of (four-) momentum between two of the three final states, the third then being given by momentum conservation. A commonly used parametrization is the Dalitz parametrization (see e.g. [29]) where two parameters with dimensions of (mass)² are used to parametrize the degrees of freedom:

$$(0 \rightarrow 1, 2, 3) : \quad m_{12}^2 \equiv (p_1 + p_2)^2 \quad m_{23}^2 \equiv (p_2 + p_3)^2 \quad (18)$$

This is also the parametrization chosen by [13] where the widths of the decays we are presently interested in have been calculated. However, $|\overline{M}|^2$ cannot in general be expected to be a smooth function of either of these variables due to resonant peaks caused by the presence of the intermediate scalar particles, and so we must understand the possible topologies we can face in our way across phase space.

In the CM of the decaying particle, the momentum vectors of the decay products must lie in a plane, due to momentum conservation. Figure 8 shows a decay proceeding through a short-lived resonance in this plane, along with specifications of Dalitz variables. When m_{23}^2 approaches the mass of the intermediate particle, it is almost on its mass shell (i.e. it is almost a real particle and not a quantum fluctuation). This fact results in a great enhancement of the decay width in the region of phase space where $m_{23}^2 \approx m_{res}^2$, the shape of the enhancement being the familiar Breit-Wigner profile⁶.

In this case, we can use our knowledge of which variable contains the resonance to deduce that $|\overline{M}|^2$ should be a smooth function of m_{12}^2 whereas m_{23}^2 would require a more

⁶Also known as the Lorentz profile, the Cauchy curve or even the Witch of Agnesi.

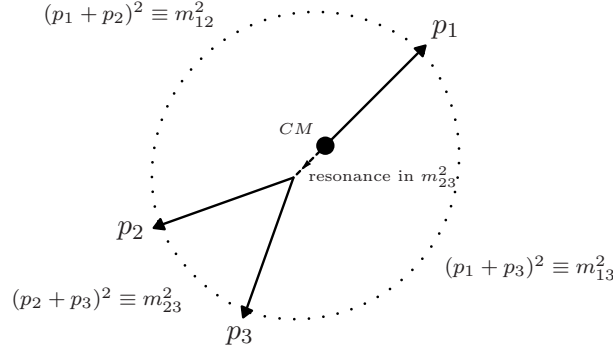


Figure 8: A three-body decay proceeding through an intermediate state, as seen in the plane spanned by the momentum vectors of the outgoing particles in the CM of the decaying particle.

careful (and CPU-time consuming) treatment. This procedure works perfectly well for decays where only one diagram contributes, but in the cases considered here, multiple diagrams contribute with different resonances in different variables and interference between them, making the game more complicated. If, for example, one of the resonances is in m_{13}^2 and we are integrating over m_{12}^2 and m_{23}^2 , then due to the general relation for Dalitz variables

$$M_0^2 = m_{12}^2 + m_{23}^2 + m_{13}^2 - m_1^2 - m_2^2 - m_3^2 \quad (19)$$

the resonance in m_{13}^2 will show up as a diagonal band in a plot of m_{12}^2 versus m_{23}^2 , possibly cutting across the integration interval. Fortunately, by using eq. (19), we can simply change integration variables and then again have a resonance which appears in only *one* of the integration variables. This is important, as the resonance can now be dealt with using a one-dimensional technique rather than a two-dimensional one (see Appendix B.1). This treats all but a few contributions. The remaining ones are terms where two different resonances in two different variables interfere with each other. Rewriting the integral so that the resonant variables become the integration variables results in a “resonance cross”, possibly inside the integration region. The various topologies are illustrated in figure 9.

The standard expression for the width of an unpolarized three-body decay expressed in Dalitz variables is [29]:

$$\Gamma(0 \rightarrow 1, 2, 3) = \frac{1}{32M_0^3} \int_{m_{12,\min}^2}^{m_{12,\max}^2} dm_{12}^2 \int_{m_{23,\min}^2}^{m_{23,\max}^2} dm_{23}^2 |\overline{M}|^2 \quad (20)$$

with the kinematical limits⁷

$$\begin{aligned} m_{12,\min}^2 &= (m_1 + m_2)^2 & m_{23,\min}^2 &= (E_2^* + E_3^*)^2 - \left(\sqrt{E_2^{*2} - m_2^2} + \sqrt{E_3^{*2} - m_3^2} \right)^2 \\ m_{12,\max}^2 &= (M_0 - m_3)^2 & m_{23,\max}^2 &= (E_2^* + E_3^*)^2 - \left(\sqrt{E_2^{*2} - m_2^2} - \sqrt{E_3^{*2} - m_3^2} \right)^2 \end{aligned} \quad (21)$$

This expression has the drawback that the variables to be integrated over and their order is already specified. We must be more general if we are to navigate through phase space

⁷The corresponding expression in [13] for the m_{23}^2 limits suffers from a minor typographical error.

THE ORIENTATION OF RESONANCES IN PHASE SPACE

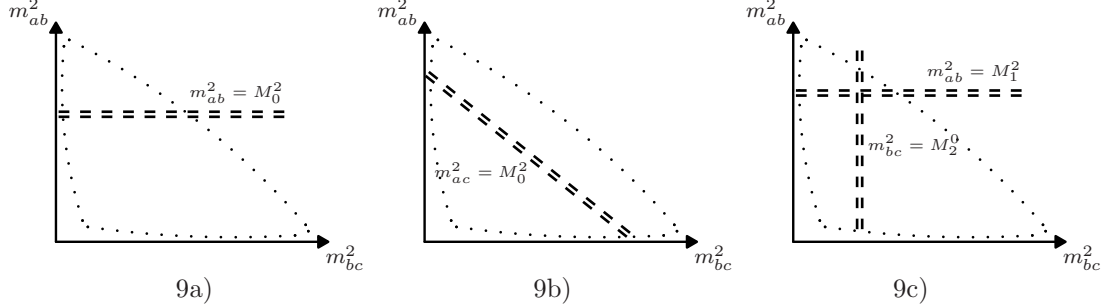


Figure 9: Various three-body phase space topologies. The dotted lines denote the kinematical limits for the integration, and the dashed lines show the placement of the resonances (it is here assumed that the resonances lie inside the integration region). The numerical integration over m_{bc}^2 can be performed trivially in the first case only. In the second, one of the integration variables must be rotated to m_{ac}^2 .

safely and with a minimum of effort. Therefore, a brief derivation of all expressions for phase space integrations in any combination and order of Dalitz variables is given in Appendix B, along with details on the numerical integrations performed in **PYTHIA**.

As we are now fully equipped to select the most advantageous path through phase space, the discussion of the decay matrix elements can proceed.

3.3.3 Neutralino Decays

In models where supersymmetry is broken by supergravity, the Lightest Supersymmetric Particle (LSP) is most often the lightest neutralino. It goes without saying then that a major impact of *R*-violating SUSY is that this particle can now decay into Standard Model particles. Neutralino decays are highly relevant to accelerator searches for *R*-parity violation, and they form the most important part of the analysis presented in section 5.

Considering the couplings in the Lagrangian, there is only one type of purely leptonic decay mode possible: $\tilde{\chi}_m^0 \rightarrow \bar{\nu}_i \ell_j^+ \ell_k^-$. Due to the Majorana nature of the neutralinos (the neutralinos are their own antiparticles), the charge conjugate channels are equally possible, i.e. $\tilde{\chi}_m^0 \rightarrow \nu_i \ell_j^- \ell_k^+$. Since there are five contributing diagrams (see fig. 7), the amplitude can symbolically be written in the form:

$$A(\tilde{\chi}_m^0 \rightarrow \bar{\nu}_i \ell_j^+ \ell_k^-) \propto \lambda_{ijk} \left(\mathcal{A}(\tilde{\nu}_i) + \sum_{\alpha=1}^2 \mathcal{A}(\tilde{\ell}_{j\alpha}) + \sum_{\alpha=1}^2 \mathcal{A}(\tilde{\ell}_{k\alpha}^*) \right) \quad (22)$$

$$\begin{aligned} \Rightarrow |A(\tilde{\chi}_m^0 \rightarrow \bar{\nu}_i \ell_j^+ \ell_k^-)|^2 &\propto |\lambda_{ijk}|^2 \left(|\mathcal{A}(\tilde{\nu}_i)|^2 + \sum_{\alpha=1}^2 |\mathcal{A}(\tilde{\ell}_{j\alpha})|^2 + \sum_{\alpha=1}^2 |\mathcal{A}(\tilde{\ell}_{k\alpha}^*)|^2 + \right. \\ &\quad \left. + 2\text{Re} \left\{ \sum_{\alpha=1}^2 \mathcal{A}(\tilde{\nu}_i) \mathcal{A}^*(\tilde{\ell}_{j\alpha}) + \sum_{\alpha=1}^2 \mathcal{A}(\tilde{\nu}_i) \mathcal{A}^*(\tilde{\ell}_{k\alpha}^*) + \sum_{\alpha=1}^2 \sum_{\beta=1}^2 \mathcal{A}^*(\tilde{\ell}_{j\alpha}) \mathcal{A}(\tilde{\ell}_{k\beta}^*) \right\} \right) \end{aligned} \quad (23)$$

The first line of eq. (23) contains the pure resonance terms whereas the second line contains

interference terms which are expected to be numerically small relative to the terms in the first line⁸.

The matrix elements for the decays considered in this work, including $L - R$ sfermion mixing, have been presented in [13], and there is little point in presenting explicit formulae here, except to note that they all follow the general layout of eq. (23).

3.3.4 Chargino Decays

The chargino decays are comparatively simpler, due to a generally smaller amount of contributing diagrams, but on the other hand, there are more possible channels. For the purely leptonic modes, there are three types of processes, all of which have been implemented in PYTHIA:

1. $\tilde{\chi}_m^+ \rightarrow \bar{\nu}_i \ell_j^+ \nu_k$
2. $\tilde{\chi}_m^+ \rightarrow \nu_i \nu_j \ell_k^+$
3. $\tilde{\chi}_m^+ \rightarrow \ell_i^+ \ell_j^+ \ell_k^-$

See Appendix [13] for detailed formulae. In all cases, the type of decay is the same as for the neutralinos: an L -conserving vertex where the chargino splits into a lepton-slepton pair (the slepton can be off mass shell) and an L -violating vertex where the slepton decays to two leptons.

3.4 \not{L} Decays Involving (s)quarks.

Several additional channels arise from the terms involving the λ' coupling in eq. (10), but besides involving different (s)particles, the matrix elements are similar to the ones previously discussed. The relevant mixing factors, colour factors, and complete formulae are given in [13]. These channels are:

1. $\tilde{\nu}_i \rightarrow \bar{d}_j d_k$
2. $\tilde{u}_{j\alpha} \rightarrow e_i^+ d_k$
3. $\tilde{e}_{i\alpha}^- \rightarrow \bar{u}_j d_k$
4. $\tilde{d}_{k\alpha} \rightarrow \nu_i d_j$
5. $\tilde{d}_{j\alpha} \rightarrow \bar{\nu}_i d_k$
6. $\tilde{d}_{k\alpha} \rightarrow e_i^- u_j$

where the indices have been chosen so that the coupling in all cases is λ'_{ijk} . Roman indices are generation indices and α runs over mass states.

For the neutralinos and charginos, there are 108 decay modes involving the λ' coupling for each neutralino/chargino, including the conjugate modes in the neutralino case. These decays are:

1. $\tilde{\chi}_m^0 \rightarrow \bar{\nu}_i \bar{d}_j d_k$

⁸This is due to the important triangle inequalities for complex numbers (see any standard text on complex analysis).

2. $\tilde{\chi}_m^0 \rightarrow \ell_i^+ \bar{u}_j d_k$
3. $\tilde{\chi}_m^+ \rightarrow \bar{\nu}_i \bar{d}_j u_k$
4. $\tilde{\chi}_m^+ \rightarrow \ell_i^+ \bar{u}_j u_k$
5. $\tilde{\chi}_m^+ \rightarrow \ell_i^+ \bar{d}_j d_k$
6. $\tilde{\chi}_m^+ \rightarrow \nu_i u_j \bar{d}_k$

where m is the neutralino/chargino number and i, j, k are generation indices. Again, the contributing diagrams are of the same type as before, and the matrix elements [13] are almost identical.

3.4.1 Gluino Decays

Since gluinos tend to be heavy in most supersymmetric scenarios, there is almost no chance that the LSP is a gluino. \cancel{R} decays of gluinos are therefore not at present implemented in PYTHIA. I estimate that this does not severely affect the analysis of the ATLAS \cancel{L} -SUSY discovery potential presented in section 5. The gluino, being heavy, has a large number of other, unsuppressed, decay channels. On this ground, the total branching into \cancel{L} modes can be expected to be small. The impact on the present analysis is therefore also likely to be small, at least in the part of SUSY parameter space where the gluino is so heavy that it has a number of unsuppressed R -conserving decay channels at its disposal.

3.5 The Monte Carlo method and PYTHIA

The necessity to make compromises has one major implication: to write a good event generator is an art, not an exact science. *T. Sjöstrand [59].*

The original work performed in this thesis has noot been to present an introduction to supersymmetry or to review the motivations (or lack of same) for the discrete symmetries thought to protect the proton. Nor has it been to calculate Feynman diagrams to obtain the decay matrix elements. When these calculations and arguments for and against have now been presented, it has been with one specific goal in mind – to argue for what I believe is the necessity of studying \cancel{L} -SUSY scenarios, and to present enough phenomenological as well as computational background to facilitate this study. The original work, then, that has so far been contained within these pages is the F77 source code for the subroutines which have been added to PYTHIA in the course of this work. Since this material is intended for general use, a few comments are necessary regarding the parameters that an eventual user would have to be familiar with. These comments can be found in Appendix C. Here, I constrain my attention to a brief introduction to MC generators in general.

The name “Monte Carlo” is associated with a particular statistical method which, due to its inherent win-or-loose technique, in turn received its name from the famous Monegasque gambling house on the French Riviera (for a review of the MC technique, see [60]). Turning immediately to the practical implementation of the technique in particle physics applications, it is worth to note that most generators on the market today include the following (here listed in the order they occur in an experiment):

1. **Pre-Interaction Era.** The colliding particles (i.e. the incoming protons for the LHC) are described by parton distribution functions, $f_{i/h}(x, \mu_F^2)$, giving the probability of

finding, inside hadron h , a parton of type i carrying momentum fraction x of the hadron momentum. The dependence on μ_F is slightly trickier to explain. When thinking of parton distributions, it is important to bear in mind that a hadron is not a static thing. Rather, it is a continually evolving dynamical system with interaction time scales between its constituents of order the inverse of the hadronic size (1 fm). As seen by a high-momentum probe, this time scale is very long, and so the hadron will effectively *seem* static during a hard interaction. This is what allows us to describe it in terms of parton distributions, i.e. as an essentially frozen object consisting of free, individual quarks and gluons. Recalling, however, that each of these is subject to quantum fluctuations, and that as we increase the wavelength (or, equivalently, the energy) with which we probe the hadron, we resolve more and more of these fluctuations, we begin to run into trouble. What, exactly, should we think of as being part of the hadronic structure, and what should we think of as short-distance phenomena associated with the hard interaction? This is exactly what the *factorization scale*, μ_F , defines. Partons which are softer (= less energetic) than μ_F are defined (by us) to be part of the hadron structure and should be part of the parton distributions while partons with higher energies belong in the hard interaction cross section. The reason μ_F is called the *factorization scale* is now easy to see. We have effectively factorized the total cross section for whatever process we are considering into a soft part and a hard part:

$$\sigma = \sum_{i,j} \int dx_1 dx_2 f_{i/1}(x_1, \mu_F^2) f_{j/2}(x_2, \mu_F^2) \times \sigma_{\text{hard}}^{ij}(x_1 p_1, x_2 p_2, Q^2 / \mu_F^2)$$

sum over possible partons	integration over momentum fractions of the partons	probability of finding partons i and j inside hadrons 1 and 2, respectively with momentum fractions x_1 and x_2 , respectively, at scale μ_F	\times	cross section for hard interaction, including anything going on above μ_F
---------------------------------	--	---	----------	--

(24)

Note that the factorization scale is not really a physical parameter. In a perfect world, the cross section would be independent of it. Usually, it is set equal to Q^2 , and the same is true for the renormalization scale used for α_s in the calculation. One therefore most often sees parton distributions expressed as $f(x, Q^2)$.

Also note that parton distributions are inherently non-perturbative quantities which cannot be calculated from first principles in QCD. Rather, some plausible functional forms are assumed for them with the exact parameters (coefficients and exponents) being fitted to data.

What is left to describe is now the hard scattering cross section, $\sigma_{\text{hard}}^{ij}$. This can easily involve multiple emissions of gluons and/or photons from the incoming partons, collectively referred to as Initial State Radiation (ISR). Since matrix elements are usually only available for small numbers of in- and outgoing particles with complexity rapidly increasing as a function of the number of particles involved, this radiation is described in MC generators by a succession of $1 \rightarrow 2$ splittings, thus not taking interference effects between successive emissions into account (including higher order splittings is a tricky issue and still lacks a satisfying solution). An extremely useful technical trick which is used in all MC generators today is to evolve this shower backwards in time, starting from the hard interaction and ending with the proton constituents.

2. **Hard Interaction Era.** This is in some sense the simplest step in the MC generation, described by (typically lowest order) matrix elements giving the differential cross

sections for the interaction of two partons to produce a given final state. As an example, PYTHIA sports all kinds of conceivable processes with 1 or 2 in- and outgoing partons. At more than 2, only select processes are implemented, and it is a rare occurrence indeed to see a hard matrix element with 5 or more in- or outgoing particles in an MC generator.

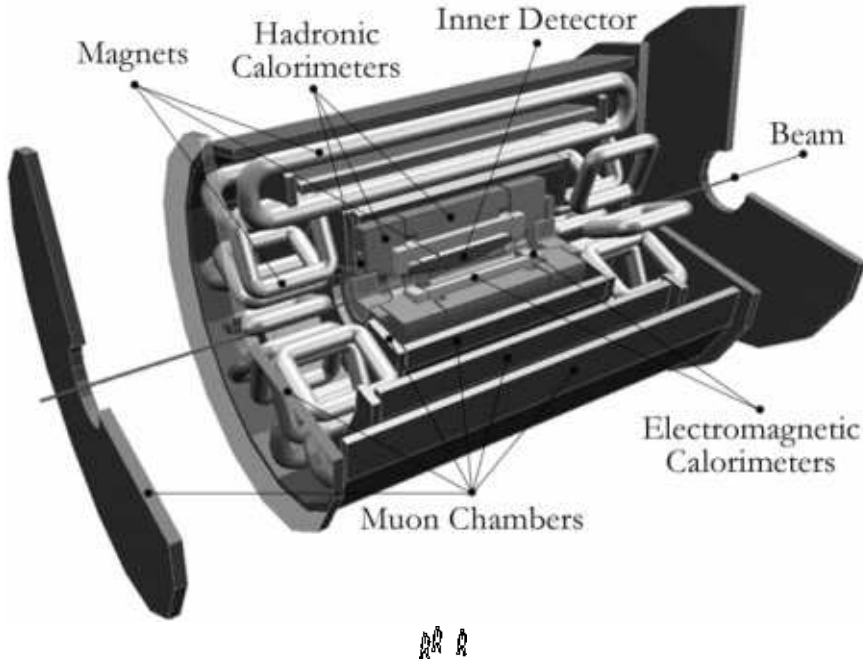
3. **Post-Interaction Perturbative Era / Parton Shower Era.** In analogy with Initial State Radiation, the partons coming out from the hard interaction radiate off gluons and photons through bremsstrahlung. In the case of gluons being radiated, they themselves will also radiate. This process, in MC language, is known as the parton shower. These radiations decrease the average parton energy while increasing multiplicity until the parton virtualities reach a cutoff value of $Q_0 = 1 - 2 \text{ GeV}$. Idealistically, perturbation theory applies until the energies become comparable to the hadronic scale given by $\Lambda_{QCD} \approx 200 \text{ GeV}$, equivalent to the length scale being about the hadronic size (confinement scale) of 1 fm. However, it would clearly be nonsense to trust first order calculations all the way to this scale. A reasonable choice, then, is to stop the perturbative phase when the strong coupling becomes larger than approximately 0.5, exactly at around 1 GeV.
4. **Post-Interaction Non-Perturbative Era / Hadronization Era.** When the partons have become sufficiently soft, hadronization (or *fragmentation*) takes place. From the border of the perturbative region and down, we enter the never-land of not analytically solvable QCD. In one end, we have the perturbative QCD of quark states that are treated as more or less free, and in the other confined quarks inside bound hadronic states. Several phenomenologically inspired models have been proposed to bridge this gap, in turn giving us an understanding of the physics that takes place, one of the more successful being the Lund “string fragmentation” model used in PYTHIA. In the string picture, coloured objects (basically quarks and gluons) are colour-connected by strings to each other, the strings being inspired by narrow flux tubes behaving somewhat like a spring or a rubber band. As such, a string carries a potential energy of its own, and this energy can be used e.g. to create new quark pairs from the vacuum. In graphical language, when the string is stretched too hard, it breaks. It is, of course, the colour connection which breaks, since the newly created quarks are also coloured. What ultimately happens is that more or less collinear⁹ partons with similar momenta join to form colour singlets, and the non-perturbative strong coupling at this soft scale ensures that we can now only talk about bound systems of quarks and gluons inside colourless hadrons.
5. **Hadronic Era.** Having now fully crossed the quark-hadron duality boundary, the description changes from the partonic one to one involving only hadronic states, in addition of course to any charged leptons, neutrinos, and photons that may have been produced. Unstable particles (mostly hadrons and taus) decay to lighter particles, decreasing the average particle mass while increasing multiplicity.
6. **Visible Era.** Long-lived hadrons (pions and kaons), electrons, muons, neutrinos, and photons traverse the detector (possibly also the SUSY LSP) and are recorded by the detector apparatus to the best of its ability, this ability depending on where the

⁹Collinear: going in the same direction.

particles hit, how energetic they are, and how strongly they interact. This step takes place outside the event generator itself, in the detector simulation.

In this work, the five first points are handled by a slightly modified version of `PYTHIA6.1` combined with the more precise supergravity evolution of `ISASUSY` (in `ISAJET-7.51`). This includes full simulation of the standard (R -conserving SUSY + SM) production cross sections (`SPYTHIA`) as well as shower descriptions, fragmentation etc. The novelty is that all SUSY particles (excepting the gluino) can now decay to SM particles via Lepton number violating couplings. Without R -Violating production cross sections, the amount of R -Violation going on is necessarily underestimated. Since the major difference is that single sparticle production could now take place, it is reasonable to suppose that this underestimation is significant only in the very heavy parts of parameter space.

4 The ATLAS Detector and ATLFast



Among the most important factors shaping the general design of ATLAS are the beam particles (protons), the energy (14 TeV), the luminosity ($10^{34} \text{ cm}^{-2} \text{ s}^{-1}$), and the cost (2.2 billion DKR). The composite nature of the proton makes it impossible to predict what the CM energy of any given hard interaction will be. Even though the proton-proton CM energy is known, the parton-parton CM energy can be anything below that number, and so one must reconstruct it on an event-by-event basis. If many particles escape detection, the CM energy will be poorly determined, and so a significant effort goes into making ATLAS as hermetically sealed as possible. The high energies of the collisions determine to some extent the physical dimensions of the detector, the other limiting factors being cost and material resistance to the radiation damage caused by the high luminosity. Another technical factor is the astounding amount of data which will be produced by the detector. With approximately 100 million interactions per second, the amount of data generated corresponds to having to handle each and every person on earth talking in a dozen telephones simultaneously. The so-called “triggers” play an essential role in bringing this data stream down to a manageable level. The triggers are cuts which are applied (in several stages, depending on complexity) before events are written to disk, i.e. non-triggered events are irrevocably lost. Thus, the triggers must stay well below the physics cuts so that potentially interesting events are kept.

The main features of the design and the physics goals of the detector are clearly established. ATLAS is first and foremost a Higgs-machine. Second, it is a TeV-scale explorer with the emphasis on Supersymmetry. For a general overview of the detector and its design, see the ATLAS Physics TDR¹⁰ [1]. I shall here be mainly concerned with the coarse, overall features of the design such as play a role in the *At1Fast* detector simulation: angular coverage, resolution and electron/muon/jet identification. Where comments are

¹⁰TDR: Technical Design Report

not explicitly made to the contrary, it is the **AtlFast** v.2.53 default parameters which have been used in this work.

4.1 The Beam

The LHC operates with two proton beams accelerated to 7 TeV each. At these energies, beam energy loss from synchrotron radiation is completely inhibitive for building circular e^+e^- colliders, at least in as “small” a ring as the LEP/LHC tunnel, and so the choice of protons is unavoidable for this machine. The design luminosity of the machine is $10^{34} \text{ cm}^{-2}\text{s}^{-1}$. With a total cross section of about 100mb, this corresponds to an event rate of 1GHz, i.e. a billion interactions per second. This “design” luminosity was initially foreseen to be reached after three years of low-luminosity running, starting at $10^{33} \text{ cm}^{-2}\text{s}^{-1}$. Due to postponements of the scheduled startup, however, the low-luminosity period has now been replaced by a shorter period of “mid-luminosity” running, starting at $3 \times 10^{33} \text{ cm}^{-2}\text{s}^{-1}$, i.e. with approximately 300 million interactions per second. Presumably, ATLAS will still have collected a total of about 30 fb^{-1} of integrated luminosity after that period. Following this, the machine will run at full luminosity, collecting a planned total of 300 fb^{-1} by 2010/2011. These numbers, of course, play a crucial role in what kind of physics (how low cross sections) the detector will be sensitive to. Their implications are discussed more closely in section 5.2 on cross sections and trigger selections.

4.2 Inner Detector

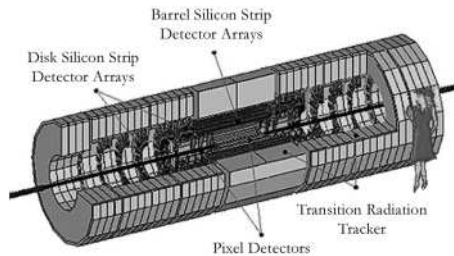


Figure 10: Schematic drawing showing the placements of the Inner Detector Components. A female physicist is shown for size comparison.

The primary functions of the 7.8 metres long and 1.1 metres radius Inner Detector are track reconstruction for charged particles and precise reconstructions of both the interaction vertex (where the hard interaction occurred) and secondary vertices (where a particle has decayed) in the event. Three distinct subsystems make up the design, all of them with a high tolerance against the tough radiation levels [61]: Silicon pixel detectors, Silicon strip detectors (called the *SCT: Semi-Conductor Tracking*), and Transition Radiation Trackers (TRT). The total cost for these components lies around 400 million DKR, to be compared with the total cost for ATLAS of 2.2 billion DKR.

Particle tracks down to $\approx 9.4^\circ$ from the beam pipe can be measured by the Inner Detector system. Often, one sees *pseudorapidity* used rather than the angle itself:

$$\eta \equiv -\ln \tan(\theta/2) \quad (25)$$

where θ is the angle from the beam axis to the radius vector of the point considered. For massless particles, this quantity is equal to the rapidity and transforms additively under Lorentz boosts along the beam direction (by convention, the z direction):

$$\mathcal{L}_z(\Delta\eta)\eta = \eta + \Delta\eta \quad (26)$$

where \mathcal{L}_z symbolically expresses a Lorentz boost in the z direction. For hadron colliders, where the CM of the interacting partons is related to the CM of the incoming hadrons by exactly a z -boost (neglecting the small transverse momenta of the partons), a quantity with such simple transformation properties is more convenient to work with. In this unit, the beam directions are given by $\eta = \pm\infty$ and the direction transverse to the beam by $\eta = 0$. The above statement that particle tracks down to 9.4° are measured translates to $|\eta| < 2.5$. In reality, only particles with transverse momenta, $p_T^2 = p_x^2 + p_y^2$, above a given threshold can be reconstructed (**At1Fast** default: $p_T > 0.5 \text{ GeV}$). Momenta are measured (SCT and TRT) with an accuracy of approximately $\sigma(p)/p \approx 6 \times 10^{-4} p [\text{GeV}]$, and vertex positions (pixels) with radial resolution $\approx 14 \mu\text{m}$ and longitudinal resolution $\approx 87 \mu\text{m}$ [61].

4.3 Calorimeters

Weighing around 4000 tons, there is ample material in the ATLAS calorimeter system to accomplish its purpose: to completely stop particles and measure the energy they give off as they are decelerated. This is done using absorbing materials in which the particles lose energy through collisions interlaced with scintillating media or other signal devices where the particles give off a signal proportional to their energy, enabling energy loss (dE/dx) and shower profile measurements, highly discriminating variables in particle identification.

4.3.1 EM Calorimeters

Electrons and photons are stopped rather more easily than hadrons, and so the innermost calorimeter in any detector is the Electromagnetic Calorimeter. In cylindrical detectors like ATLAS, this is divided into a barrel part and an end-cap part. In ATLAS, the barrel calorimeter, being 6.8 m long and 4.5 m in outer diameter, covers $|\eta| < 1.475$ i.e. angles larger than 26° from the beam-pipe while the end-cap region covers $1.375 < |\eta| < 3.2$ ($\Rightarrow 4.5^\circ < \theta < 28^\circ$) [62]. Lead and liquid Argon are used as absorber and scintillator, respectively. The individual cells (numbering in the hundred thousands) are constructed in varying sizes (as measured in cartesian coordinates) and are mounted facing the center of the detector such that their $\eta \times \phi$ areas remain constant throughout the subdivisions of the detector with the best resolution ($\Delta\eta \times \Delta\phi = 0.025 \times 0.025$ corresponding to about 4 by 4 centimetres at $\eta = 0$) in the $|\eta| < 2.5$ region where also the Inner Detector is active. This high-precision part of the calorimeter can be used to separate e.g. pions, electrons, and photons while the coarser granularity outside means that only measurements of E_T and reconstruction of jets is undertaken in that region. The rather crude parametrization of this structure included in **At1Fast** will be described below.

4.3.2 Hadronic Calorimeters:

The ATLAS hadronic calorimetry consists of three subdetectors: the Hadronic Tile Calorimeter in the central region (barrel and extended barrel, $|\eta| < 1.7$), the End-Cap (Liquid Argon) Calorimeter in the intermediate region ($1.5 < |\eta| < 3.2$), and the Forward (Liquid Argon) Calorimeter covering pseudorapidity down to $|\eta| < 4.9$ [62].

The Tile Calorimeter has an outer diameter of 8.5m and is about 13m long. A division into a barrel ($|\eta| < 1$) and two extended barrel parts ($0.8 < |\eta| < 1.7$) [63] with a small gap between is necessary simply because the electronics of the inner parts of ATLAS have to feed out somewhere. Both use steel as the absorbing material, interspersed with scintillating plates. The granularity lies at a planned $\Delta\eta \times \Delta\phi = 0.1 \times 0.1$, the default for the toy calorimeter used in **At1Fast** for the central regions of the detector.

Each of the LAr end-caps consists of two copper wheels (2.5 cm and 5cm thickness, respectively) about 2 metres in radius. Up to $|\eta| = 2.5$, the granularity is 0.1×0.1 whereafter it becomes 0.2×0.2 up to $|\eta| = 3.1$ [64]. Lastly, the most challenging of the calorimeters are the Forward Calorimeters. Situated a mere 4.7 metres from the interaction point at high pseudorapidities, the radiation levels here are considerable. The advantages are equally considerable, however, in terms of providing uniform coverage up to $|\eta| = 4.9$. For technical reasons, the calorimeter cannot be very long and so must be very dense instead. Three sections, one of copper and two of tungsten, are included in the design [64]. As a side remark, Liquid Argon detectors aren't cheap. All in all, the cost of the Liquid Argon Calorimeters is estimated at slightly less than 600 million DKR, roughly a fourth of the total cost for ATLAS, 2.2 billion DKR [65].

4.4 Calorimetry in ATLFAST:

The complex structure described above would be much too cumbersome to fully model in a fast simulation. Instead, **At1Fast** uses a toy calorimeter where the size of the simulated calorimeter cells in $\eta \times \phi$ coordinates is 0.1×0.1 in the central region ($|\eta| < 3$ [66]) and 0.2×0.2 outside (down to $|\eta| = 5$). Based on the energy contents of these cells, so-called *clusters* are searched for – groups of cells close together having larger than nominal energy, i.e. suspected remnants of jets, electrons, or photons. Technically, this is done using the “Snowmass Accord” [67]: Begin by defining a cone of a certain radius in $\eta - \phi$ space,

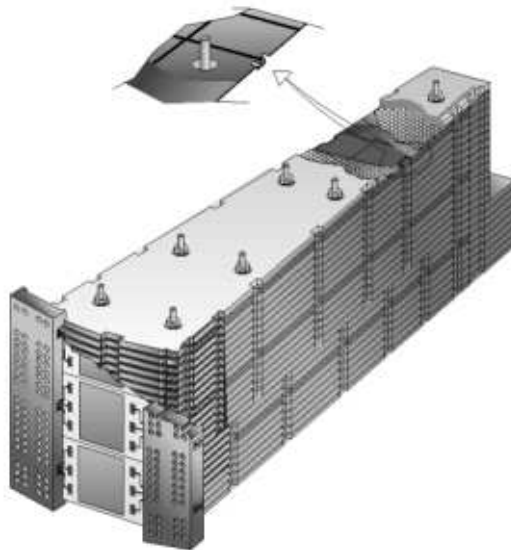


Figure 11: Schematic of a module of the Hadronic Tile Calorimer. The center of the detector lies towards upper right.

$\Delta R = \sqrt{\Delta^2\eta + \Delta^2\phi}$ (**At1Fast** default: $\Delta R = 0.4$), sum up the p_T inside it, and calculate the position of the E_T -weighted cluster axis by:

$$E_T^{cluster} = \sum_{i \in cone} E_T^i \quad (27)$$

$$\phi^{cluster} = \frac{1}{E_T^{cluster}} \sum_{i \in cone} E_T^i \phi^i \quad (28)$$

$$\eta^{cluster} = \frac{2}{E_T^{cluster}} \sum_{i \in cone} E_T^i \eta^i \quad (29)$$

and shift the cone position around until the cone and cluster axes line up. Here, ϕ^i, η^i is the position of the i 'th calorimeter cell and we now use E_T instead of p_T since the calorimeters measure energies rather than momenta. This is a slightly pedantic custom since these two quantities are equal for masses that are small compared to the energy, as is the case for hard leptons and jets. The Snowmass definition, however, does not specify how to deal with overlapping clusters, and so a more refined procedure is applied in practice. If two clusters overlap, then merge them into one if there is a lot of E_T in the overlap region, else split the energy between if there is only little E_T .

In **At1Fast**, only clusters with $E_T^{cluster} > 10$ GeV are included in the jet/electron/photon reconstruction. This reconstruction is fairly accurate with errors around 0.04rad [66] for the difference between the initiating parton direction and the center of the reconstructed cluster. The reconstruction of E_T is not quite as good, due to energy depositions outside the defined cluster cone. Denoting the difference between the estimated and original parton transverse energies by $\Delta E_T = E_T^{est.} - E_T^{par.}$, a large tail towards negative $\Delta E_T/E_T^{par.}$ appears with an rms deviation of around 0.2 for the WH , $H \rightarrow u\bar{u}$ sample process ($m_H = 100$ GeV) studied in [66]. Since these jets can be loosely categorized as “quark jets from a heavy object”, it is not expected that this error will change greatly for the case of hadronic decays of SUSY particles. It is, however, believed that this error can be corrected for on average when the jet energies are recalibrated. In such procedures, one estimates the true parton energy from that estimated by the cone algorithm by [68]:

$$E^{par.} = \frac{E_{jet}^{est.} - E_O}{R_{jet}S} \quad (30)$$

where E_O is an offset correcting for noise in the detector and energy depositions not associated with the parton jet itself (i.e. the underlying event and pile-up), R_{jet} is a correction for the calorimeter jet energy response and energy lost in cracks, and S is the fraction of energy associated with the jet but not contained within the reconstruction cone. See [68] for an excellent and more detailed review of the techniques used in jet energy determinations.

Finally, electrons, photons, and jets are reconstructed from the identified clusters (muons generally leave so little energy in the calorimeters that the cluster criteria are impossible to meet). Electrons, muons, and photons which sit relatively alone in the detector are exceedingly important to measure since they will often be the direct decay products of the hard interaction products. A particle produced in the decay of a fast-moving low-mass particle will generally tend to follow its mother, whereas a particle produced by a high-mass particle which is more or less at rest, will generally sit without much surrounding activity in the detector. Such particles are given the name *isolated*, and since we shall

Particle	Eff($p_T < 50$ GeV)	Eff($p_T > 50$ GeV)
Electron	70 %	80 %
Muon	95 %	95 %

Table 3: Assumed reconstruction efficiencies for muons and electrons.

require all leptons in the analysis to be isolated, we now present the isolation criteria used in **AtlFast** for electrons and muons.

Electron candidates from the Inner Detector (i.e. with $|\eta| < 2.5$) with $p_T > 5$ GeV are connected to clusters in the calorimeters with a maximum distance between the cluster and the electron of $\Delta R = 0.1$. The isolation criteria used as defaults in **AtlFast** are a separation from any other clusters by at least $\Delta R = 0.4$ and an energy deposition of maximally $E_T = 10$ GeV in a cone of $\Delta R = 0.2$ around the electron. For the sample process $H \rightarrow e^+e^-e^+e^-$ studied in [66], the efficiency of these criteria was 95.3%, in good agreement with results from full simulation.

For muons, the inner detector is used in combination with the muon system by default. A muon with $|\eta| < 2.5$ and $p_T > 6$ GeV is a candidate for isolation. By default, the same isolation criteria in terms of energy depositions and cone sizes as for electrons are applied. For the sample process $H \rightarrow \mu^+\mu^-\mu^+\mu^-$ studied in [66] the efficiency was 97.8% for **AtlFast**, significantly better than what was obtained by full simulation [1, table 8-1]: approximately 85% (yielding an efficiency for each muon of roughly $(0.85)^{1/4} = 0.96$). In this work, an attempt at obtaining more believable numbers has been made by including by hand estimated electron and muon reconstruction efficiencies. Using the same electron reconstruction efficiency for all energy ranges would be much too crude. Instead, two numbers, depending on the electron p_T , are used. The assumed electron and muon reconstruction efficiencies, representing educated guesses based on the ATLAS Physics TDR [1, table 7-1 and table 8-1], are given in table 3.

In the end, any clusters which have not been associated with electrons, muons, or photons, are labelled as reconstructed jets if their E_T is larger than 15 GeV. Furthermore, when the detector is running at high luminosity, some pile-up is expected in the calorimeters, i.e. events begin to overlap, worsening the energy resolution. For precision physics, i.e. measurement of the Higgs mass and any exclusive measurements, the degraded resolution can be a serious problem. For the study at hand, note that we wish only to determine if there is and, if so, what type of supersymmetry there is using strictly inclusive quantities, and so a larger smearing of the energy should not significantly affect the result (yet this remains to be verified).

4.5 Muon System

The ATLAS muon spectrometer is composed of three layers of Cathode Strip Chambers (CSC) close to the interaction point and close to the beam axis and Monitored Drift Tube (MDT) chambers over the rest of the coverage (up to $|\eta| = 2.7$). The chambers are arranged symmetrically around the beam axis in the barrel region and vertically in the end-cap region. Schematic drawings of the arrangement of the chambers on the sides and on the ends of the detector are shown in figure 12. The system is immersed in a magnetic field provided by superconducting air-core toroid magnets with the resulting bending of

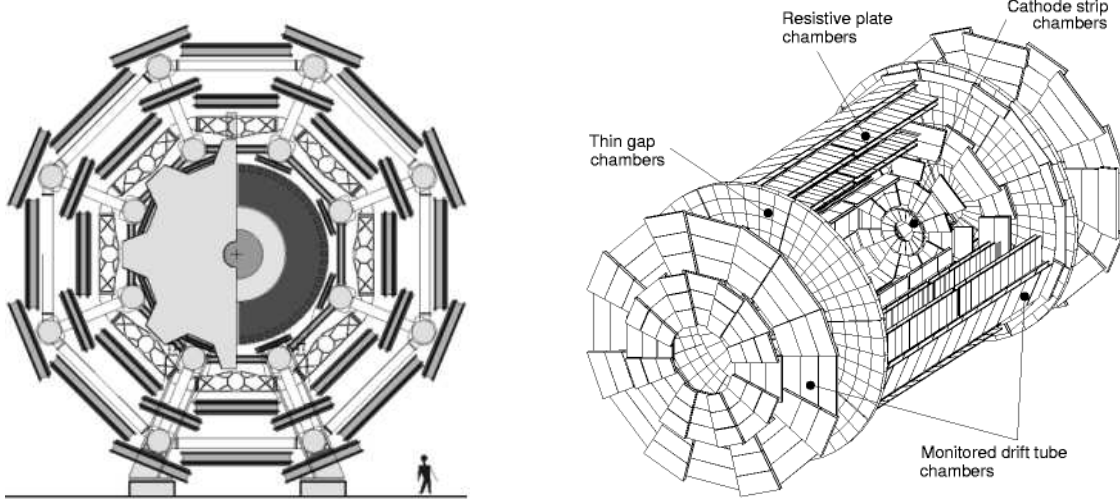


Figure 12: End view and perspective view of the ATLAS muon chambers.

the muon tracks yielding more precise momentum determinations than could be obtained using the Inner Detector alone. Since one of the main purposes of the muon spectrometer is to enable a mass measurement for very narrow Higgs signals, it is quite important that a mass resolution of about 1% can be obtained this way. The foreseen resolution, as given in the Technical Design Report for the Muon Spectrometer lies at $\Delta p_T/p_T \approx 2\%$ for muons of p_T between 20 and 100 GeV. For 1000 GeV muons, this resolution worsens by a factor of roughly 5 [69].

In addition to the performance at high p_T , low- p_T muons from B decays require a system containing as little “dead” material as possible. This is among the main reasons that an air core design for the magnets was chosen, resulting in muons down to 3 GeV surviving to be measured by the muon system, the hadron calorimeter being the largest absorber on the way.

Also included in the muon spectrometer is a muon trigger system, extending to $|\eta| < 2.4$, increasing the precision of the muon trigger and the identification of which of the pulsed beam segments, or “bunches”, of the LHC (spaced by 25 ns [1]) the event belonged to. In addition, the trigger information, though less precise, can be used to supplement the measurements made in the precision chambers with an extra coordinate.

5 Analysis of ATLAS \cancel{L} -SUSY Discovery Potential

There is at present no experimental evidence either for or against supersymmetry in nature, although some significant exclusion limits have been achieved at LEP. This picture is expected to change drastically over the next few decades, hopefully already within the next ten years. It has been argued above that supersymmetry can only solve the hierarchy problem if the sparticle masses are not significantly larger than the TeV scale. This range is within reach of second generation hadron machines such as the LHC, and so we expect to see direct production and decay of supersymmetric particles relatively soon if supersymmetry exists. On the other hand, the *non-observation* of supersymmetric processes will disfavour low-energy supersymmetry almost to the point of exclusion, giving us a powerful clue that we must look to some alternate mechanism for solving the hierarchy problem. Whatever the case, it is not unreasonable to suppose that the resolution of the hierarchy problem will give *some* observable effects at the TeV scale, and so we find ourselves almost guaranteed that interesting experimental results will be obtained in the not too distant future. This section deals with the possible observable consequences of lepton number violating supersymmetry at the ATLAS detector, one of four detectors being built for the LHC and scheduled to go online in 2006.

The organization of the section is as follows: In 5.1, we define the points in mSUGRA space and the scenarios for the L -violating couplings we will be using in the analysis. Next, in 5.2 we propose trigger menus dedicated to searches for \cancel{L} -SUSY at mid-luminosity running of the LHC ($L = 3 \times 10 \times 10^{33} \text{ cm}^{-2}\text{s}^{-1}$). At this luminosity, pile-up is expected, meaning that several events are recorded simultaneously by the detector, degrading the energy resolution. Since there are no tools presently available to parametrize this for mid-luminosity running, we account for this effect in a very crude manner by simply scaling the simulated event rates by a common factor.

In 5.3 and 5.4, the main part of the analysis is presented, concentrating on what can be achieved with an amount of data corresponding to an integrated luminosity of 30 fb^{-1} . It is divided into two parts, one based on cuts and one based on neural networks. The purpose of the first part is to choose cuts on several kinematical and inclusive variables which isolate a fairly broad event sample enriched in supersymmetric events with no emphasis on any particular scenario, except of course that lepton number is assumed violated. The purpose of the second part is to process this event sample with neural networks trained to recognize particular scenarios. Due to the large luminosity at the LHC, it has not been possible to generate an event sample of comparable magnitude to 30 fb^{-1} of data taking for the highest cross section backgrounds. For Z/W production and moderate p_T QCD processes, each generated event thus corresponds to hundreds of events expected in data. For these event samples, the large rejection factors reached will eventually cause only a very few or zero events to remain after cuts. At this point, we estimate the event numbers by 95% confidence upper limits, fitting to the event distribution below the cut or by using Poisson statistics on the number remaining after the cut (see [29, 70]). Rejection factors for these events are in principle unknown but can be pessimistically estimated using the rejection factors for the high p_T QCD sample and the double gauge events. Lastly, in 5.5 the results of the cut-based analysis combined with the neural network classification are presented.

	\mathbf{P}_2	\mathbf{P}_7	\mathbf{P}_9	\mathbf{P}_{12}	\mathbf{F}_2
GUT Parameters					
$\tan \beta$	5	10	20	35	10
m_0	170	335	100	1000	2100
$m_{\frac{1}{2}}$	780	1300	300	700	600
$\text{sign}(\mu)$	+	+	+	−	+
A_0	0	0	0	0	0
Mass Spectrum					
h^0	118	123	115	120	119
A^0, H^\pm, H^0	110	1663	416	944	2125
$\tilde{\chi}_1^0$	325	554	118	293	239
$\tilde{\chi}_2^0, \tilde{\chi}_1^+$	604	1025	217	543	331
$\tilde{\chi}_3^0$	947	1416	399	754	348
$\tilde{\chi}_4^0, \tilde{\chi}_2^+$	960	1425	416	767	502
\tilde{g}	1706	2752	707	1592	1442
$\tilde{e}_R, \tilde{\mu}_R$	336	584	156	1031	2108
$\tilde{\tau}_1$	334	574	126	916	2090
$\tilde{e}_L, \tilde{\mu}_L$	546	917	231	1098	2126
$\tilde{\tau}_2$	546	915	240	1051	2118
$\tilde{\nu}$	541	913	217	1095	2125
\tilde{q}_R	1453	2333	612	1612	2328
\tilde{b}_1	1403	2262	566	1412	2010
\tilde{t}_1	1189	1948	471	1241	1592
\tilde{q}_L	1514	2425	633	1663	2343
\tilde{b}_2	1445	2312	615	1482	2310
\tilde{t}_2	1443	2286	648	1451	2018

Table 4: Selected points of analysis in the mSUGRA parameter space.

5.1 Points of Analysis

For reasons of simplicity, we concentrate on a few points in the mSUGRA parameter space. These points have not been chosen among the ones initially suggested in the ATLAS Physics TDR. This is partly due to the exclusion of all these points by LEP (essentially from bounds on the Higgs mass), and partly since it is interesting to enable a direct comparison between the capabilities of the LHC and other, future experiments such as CLIC (Compact Linear Collider), a 3 TeV electron-positron collider currently under study at CERN. On these grounds, the analysis is performed on a selection of points defined by the CLIC physics study group. A general drawback to any selection of points defined within the MSSM framework is of course that they are constructed to make the lightest neutralino the LSP. In an R -Violating scenario, this condition does not apply, and so one should bear in mind that the full parameter space can never be analyzed using just MSSM points, though an attempt at defining new points for R -Violating scenarios would go beyond the scope of this work. The 5 mSUGRA points shown in table 4 have been selected among 14 points defined by the CLIC physics study group on the basis that they represent the broadest possible range within those points. Let it be emphasized that I am not aiming to do precision physics in this work, but rather to estimate the sensitivity

	a	b	n
LLE : Purely Leptonic Lepton Number Violation			
λ_{ijk}	10^{-2}	10^{-4}	$\sqrt{\hat{m}_{e_i}\hat{m}_{e_j}\hat{m}_{e_k}}$
λ'_{ijk}	0	0	0
LQD : Minimally Leptonic Lepton Number Violation			
λ_{ijk}	0	0	0
λ'_{ijk}	10^{-2}	10^{-4}	$\sqrt{\hat{m}_{e_i}\hat{m}_{q_j}\hat{m}_{d_k}}$
LLE + LQD : Mixed Lepton Number Violation			
λ_{ijk}	10^{-2}	10^{-4}	$\sqrt{\hat{m}_{e_i}\hat{m}_{e_j}\hat{m}_{e_k}}$
λ'_{ijk}	10^{-2}	10^{-4}	$\sqrt{\hat{m}_{e_i}\hat{m}_{q_j}\hat{m}_{d_k}}$

Table 5: Selected points of analysis in the $\lambda - \lambda'$ parameter space. The models with natural couplings (column n) will be referred to as “nLLE”, “nLQD”, and “nLLE + nLQD” in following sections. If the couplings get significantly smaller than 10^{-4} , the LSP lifetime can become so large that it decays outside the detector, mimicking the R -conserving scenarios. For example, for the mSUGRA point F_2 , setting all λ couplings to 10^{-6} and all λ' couplings to zero results in a decay length for the LSP of $\tau c = 40\text{m}$. In the intermediate range, one may see the effects of neutralino decay either as a secondary vertex or as a decay inside the fiducial volume of the detector. Naturally, such spectacular signatures would greatly lessen the effort required to discover SUSY, yet we abstain from studying such scenarios here so as not to be overly optimistic in our results.

for \mathbb{Z} -SUSY for various mass hierarchies. It is therefore not interesting whether we are sensitive to one or another particle or which exact numerical values the masses have. What is interesting is how sensitive we are for light/medium/heavy masses for the lightest neutralino in particular and for various possibilities for the other masses. In this light, there is a great redundancy in the 14 CLIC points, and thus the 5 points given in table 4 have been chosen for their mutual differences.

In addition, values for the R -Violating couplings must be specified. The experimental upper bounds lie around $10^{-1} - 10^{-2}$ for most couplings [71], depending on the masses of the squarks and sleptons, with heavier masses allowing larger couplings. For the cases of purely leptonic (LLE), mixed (LLE+LQD), and minimally leptonic (LQD) Lepton number violation, three models are investigated beyond the MSSM without modification. Firstly, two points with common values for all couplings, and secondly a model with generation-hierarchical couplings defined by [35]:

$$\begin{aligned}
|\lambda_{ijk}|^2 &= \hat{m}_{e_i}\hat{m}_{e_j}\hat{m}_{e_k} & ; & \quad \hat{m} \equiv \frac{m}{v} = \frac{m}{126\text{GeV}} \\
|\lambda'_{ijk}|^2 &= \hat{m}_{e_i}\hat{m}_{q_j}\hat{m}_{d_k}
\end{aligned} \tag{31}$$

where m_{q_j} represents the mass of “a quark of generation j ”. Due to the mass splittings of the quarks, this definition is inherently ambiguous. A way to resolve the ambiguity suggested by [72] is to set m_j equal to the arithmetic mean of m_{u_j} and m_{d_j} where u and d stand for up-type and down-type respectively:

$$m_{q_j} = \frac{1}{2}(m_{u_j} + m_{d_j}) \tag{32}$$

This procedure is the one implemented in PYTHIA. The resulting coupling scenarios are given in table 5.

An additional noteworthy remark is that while small \cancel{R} couplings have little or no impact on the masses and couplings at the electroweak scale, large \cancel{R} couplings (as compared to the other couplings in the theory) can have significant effects through loops when evolving the Renormalization Group Equations (RGE's) from the input scale to the TeV scale. This is currently not included in PYTHIA. The \cancel{R} couplings are simply switched on at the low scale and the interplay between the \cancel{R} couplings and other physics is neglected. Order-of-magnitude-wise, this assumption breaks down for $\lambda^{(\prime)} > 10^{-2}$, and so some effort should be devoted to including the full RGE's in simulations of \cancel{R} -SUSY. Also, the CLIC points assume a vanishing trilinear coupling at the GUT scale, i.e. $A_0 = 0$. In connection with this work, a small study of the direct consequences of that assumption upon the results presented here was performed (see section 3.1) with the conclusion that the semi-inclusive branching ratios (e.g. $BR(\tilde{\chi}_1^0 \rightarrow qq\nu)$) depend only very weakly on this parameter ($\mathcal{O}(5\%)$), and so the main signatures (number of leptons, number of jets, etc.) should be only mildly affected by changes to this parameter.

5.2 Trigger Selection

The cross sections for SUSY production at the LHC for the points studied in this work range from 10^{-8} – 10^{-12} mb. For comparison, the cross section for e.g. Z/W production is 10^{-3} mb, and the total interaction cross section (excepting elastic and diffractive processes which do not give rise to hard jets, leptons, or neutrinos) is around 70mb, mostly consisting of small-angle QCD interactions. Background rejection is thus extremely essential. In an ideal world, all data recorded by the experiment would be written to disk for later scrutiny. With the extreme event rates and sizes (approximately 1 billion events per second and approximately 1MB per event[1]) at the LHC, such a strategy is entirely out of the question, moreover it is completely uncalled for. The extreme rates are only necessary to enable us to *reach* the very small Higgs and New Physics production cross sections. As already mentioned, the vast majority of events are QCD processes with small momentum transfers. Relative to how much statistics we need to study *those* processes, we get a huge over-abundance. We can then accept to limit the data flow by cutting away a significant fraction of those events and writing only a very small subset of them to disk, along with events which contain possible traces of low cross section physics. To accomplish this reduction, an extensive trigger system is being developed for ATLAS which will identify the (possibly) interesting events and reject uninteresting ones. For SUSY, typical signatures that can be triggered on include a lot of missing transverse energy (\cancel{E}_T) and large (hard) jet and lepton multiplicities¹¹. The usefulness of the “classical” SUSY \cancel{E}_T signature will in general be decreased in \cancel{R} scenarios due to LSP decay, but it remains of some discriminating power. On the other hand, the LSP decays to jets, leptons, and/or neutrinos, and so the signature is merely transformed, not lost. We can use this to define a set of triggers that will reject the QCD background (which typically has small \cancel{E}_T and jet/lepton multiplicities) but keep the majority of those events that might have been caused by the production and decay of supersymmetric particles.

5.2.1 \cancel{L} -SUSY Triggers at Mid-Luminosity

The acceptable rate of events that can be written to disk is about 100Hz. The sum rate of *all* the triggers which will be implemented in ATLAS must therefore stay below this

¹¹Large multiplicity = many particles.

number. This includes triggers for Higgs physics, B physics, Z/W physics, and all kinds of New Physics triggers, of which \cancel{R} -SUSY is only one. A reasonable aim for the trigger rate for the \cancel{R} -SUSY triggers is therefore about 1Hz. Since no detailed trigger rate studies for mid-luminosity running are yet available, I here present some crude estimates for the trigger rates for various trigger possibilities. It should be understood that there are quite significant uncertainties associated with these, as one might well imagine when already uncertain quantities are extrapolated over orders of magnitudes in their domain. The jet rates, especially, are not well under control, although interesting work is in progress [73, 74, 75]. It has not been possible here to perform a systematic study of the effects of varying QCD parameters on the trigger rates, yet it is useful in the following to keep in mind that the multi-jet rates can be uncertain by factors of 2 or more [66].

The only processes which have rates above the 1Hz domain are QCD $2 \rightarrow 2$ processes and Z/W production, the former with a cross section around 70mb (but strongly peaked distributions), the latter with a cross section around 10^{-3} mb with more broad distributions and so more likely to be triggered on (By “ Z/W ” production is meant the sum of Z , including photon interference, and W production). In this crude study, we shall not focus on where in the trigger system which triggers are placed (i.e. LVL1, LVL2, or LVL3). This is a technical issue which requires more detailed knowledge of the detector performance at mid-luminosity than is currently available in **AtlFast**. Specifically, running at mid- and high luminosity means that there can be several interactions recorded simultaneously by the detector (pile-up), leading to some smearing of event distributions. Since the whole point is that most events should lie *outside* the trigger domain than inside it, more events will be smeared *into* the trigger domain than out of it, increasing the trigger rates when pile-up is at play. This is currently only parametrized in **AtlFast** for high luminosity. We here adopt a crude best-guess approach, performing the simulation for low luminosity, i.e. without pile-up, and multiplying the resulting trigger rates by 5 instead of 3 to get from $L = 10^{33} \text{ cm}^{-2}\text{s}^{-1}$ to $L = 3 \times 10^{33} \text{ cm}^{-2}\text{s}^{-1}$. This number is based on the scaling exhibited by the trigger rates presented in [1, chp.11] from $L = 10^{33} \text{ cm}^{-2}\text{s}^{-1}$ to $L = 10^{34} \text{ cm}^{-2}\text{s}^{-1}$ where factors between 1 and 5 are found between triggers at equal thresholds after dividing out the factor 10 caused by the luminosity difference. The triggers for which this direct comparison was possible were the inclusive electron, electron/photon, and $\cancel{E}_T + 2\text{jets}$ triggers. Since we are here interested in going from $L = 10^{33} \text{ cm}^{-2}\text{s}^{-1}$ to $L = 3 \times 10^{33} \text{ cm}^{-2}\text{s}^{-1}$, a factor of 5/3 was deemed suitable. These rates should then to be understood as corresponding to LVL3 trigger rates. Suitable intermediate trigger levels will presumably be studied in more detail and with full detector simulation by the ATLAS trigger/DAQ community in the near future.

Returning to the issue at hand, we now propose 11 trigger menus for SUSY searches in \cancel{E}_T scenarios (bearing in mind the many possible signatures in these scenarios). Granting that the LSP might be the neutralino even in \cancel{E}_T scenarios, it is tempting to define triggers based on the neutralino decay channels, $q\bar{q}\nu$, $q\bar{q}\ell$, and $\ell\bar{\ell}\nu$. This would work well at all of the SUSY points analyzed here since all of them have a neutralino LSP, but one should keep in mind that the lightest neutralino need not be the LSP when R is violated. Let us therefore go back to the terms in the superpotential that we are after: LLE and LQD , i.e. a coupling between three (s)leptons and a coupling between two (s)quarks and one (s)lepton, where only one of the particles coupling in each case will be a sparticle. From this very general standpoint, obvious trigger strategies suggest themselves.

In the case of the first coupling (LLE), we are searching for a number of leptons (depending on whether one or two supersymmetric particles were produced and whether

Trigger	Background Rate	MSSM Efficiency	LLE Efficiency	LQD Efficiency
mu45I + mu45I	0.2 Hz	1 — 5 %	10 — 40 %	1 — 10 %
e45I + e45I	0.1 Hz	1 — 5 %	1 — 35 %	1 — 10 %
mu15I + e15I	0.1 Hz	2 — 5 %	20 — 60 %	2 — 15 %
mu40I + me75	0.3 Hz	10 — 25 %	40 — 75 %	10 — 35 %
e40I + me75	0.2 Hz	10 — 20 %	15 — 70 %	10 — 35 %
j100 + mu40I	0.5 Hz	10 — 20 %	45 — 70 %	10 — 40 %
j100 + e40I	0.5 Hz	5 — 15 %	15 — 65 %	10 — 35 %
j100 + me175	0.3 Hz	50 — 80 %	35 — 80 %	25 — 80 %
3j50 + mu20I	0.1 Hz	5 — 15 %	45 — 60 %	12 — 40 %
3j50 + e30I	0.1 Hz	5 — 10 %	15 — 55 %	10 — 35 %
3j75 + me125	0.1 Hz	30 — 65 %	30 — 70 %	40 — 90 %
Total Rate /Combined Efficiency	2.1 Hz	60 — 90 %	90 — 99.9 %	60 — 96 %

Table 6: Estimated trigger rates for background processes and trigger efficiency ranges for the various MSSM points and \cancel{L} -SUSY scenarios studied for $L = 3 \times 10^{33} \text{cm}^{-2} \text{s}^{-1}$ (summary of plots in appendix D). The trigger symbols are described in the text. The total trigger rate is slightly smaller than the sum of the individual rates, since one event can fulfil several trigger criteria. One sees how much cleaner the signatures of the purely leptonic (LLE) coupling are compared to the signatures involving quarks (LQD) where higher thresholds, due to the hadronic environment, mean smaller efficiencies.

they decayed into two- or three-body channels), possibly accompanied by \cancel{E}_T . We do not here consider an all-neutrino signature since this would be equivalent to the R -conserving SUSY \cancel{E}_T signature. We require: at least two isolated electrons and/or muons or one isolated e or μ accompanied by \cancel{E}_T .

For the LQD term, we expect jets accompanied by leptons or \cancel{E}_T . The triggers proposed are: at least 3 jets accompanied by either \cancel{E}_T or at least one isolated μ or e , or at least 1 jet, accompanied by the same with higher thresholds. Each trigger was studied for several possibilities and combinations of trigger thresholds. The complete scans around the selected threshold values are shown and commented in Appendix D. Here, event rates for the selected values of the trigger cuts are given in table 6 where also the efficiencies with which these triggers allow signal events to pass are listed. The nomenclature for each trigger item is such that e.g. ‘mu20I’ and ‘e40I’ mean ‘a muon with $p_T > 20 \text{ GeV}$ which is isolated’, and ‘an isolated electron with $p_T > 40 \text{ GeV}$ ’, respectively. ‘3j100’ and ‘me80’ mean three reconstructed jets of (each) more than 100 GeV p_T and more than 80 GeV missing transverse energy, respectively. To save space, the signal trigger efficiencies are given as ranges (min—max), obtained by dividing the scenarios studied into three categories and scanning for the minimum and maximum efficiencies within each category. These categories are: the MSSM (for reference), purely leptonic \cancel{L} (i.e. decays proceeding via the λ couplings (LLE)), and mixed quark-lepton L -violation (the λ' couplings (LQD)).

Scenarios where both types of couplings are non-zero generally lie inbetween the two extremes, depending on the relative coupling strengths. The efficiency ranges reached by combining all the triggers are shown in the bottom of the table.

5.2.2 Final Remarks

Though these trigger proposals are designed explicitly with \mathcal{R} -SUSY in mind, they show a certain overlap with triggers proposed for more conventional physics. The di-muon and 3 jets + lepton triggers, for example, have also been proposed for various Higgs searches. The di-electron trigger as well as 3 jets + electron are proposed to catch $t\bar{t}$ decays. Finally, the conventional SUSY searches also make use of multi-lepton, jets + \cancel{E}_T , and multi-jet signatures [76]. It is therefore not unthinkable that the triggers here proposed can be incorporated to some extent into the conventional trigger programme, possibly enabling a relaxation of the trigger thresholds for the remaining objects.

Finally, though no study of the mutual redundancy among these trigger objects has been performed, one sees from table 6 that e.g. the di-electron trigger and the 3-jet + electron trigger have low efficiencies, this mainly due to the low electron reconstruction efficiency which is required to be sure one is not mistakenly believing a jet to be an electron (see [1, table 7-1] for estimated jet rejection factor as function of electron reconstruction efficiency). As a suggestion for future analyses, it might be worthwhile to investigate what happens if one dispenses with these two triggers, replacing them with e.g. two-jet + leptons or two-jet + \cancel{E}_T triggers instead, yet caution in such undertakings is advisable. The presence of electron triggers is, for example, essential in catching scenarios where the first generation \cancel{L} couplings are dominant. This is the reason why as little dependence on lepton flavour as possible has been strived for in the menus here proposed.

5.3 Discriminating Variables

We now come to the cut-based analysis. The purpose here is to define a set of discriminating variables, i.e. variables capable of distinguishing in a statistical sense between the SM and the various SUSY scenarios. Once defined, the idea is to use these variables and our knowledge of their distributions in SM and non-SM scenarios to isolate a sample of events with maximal possible enrichment of SUSY events and minimally contaminated by SM events. At this point, we do not seek to distinguish between or aim the analysis towards any particular SUSY scenarios, except that we assume the LSP to decay through violation of lepton number.

In the following pages, a number of kinematical and inclusive variables are presented. The distributions of each variable in the SM and in the mSUGRA models determine at which values of the variables cuts should be placed. In a conventional analysis of this type, one would seek to maximize the statistical significance with which a signal can be extracted by adapting the analysis to maximize quantities like S/B , $S/(S+B)$, or $S/\sqrt{S+B}$, where S and B are the number of signal events and the number of background events, respectively, remaining after the analysis. Obviously, this requires knowledge about the shapes of both signal and background distributions in each of the discriminating variables. In the present case, we wish to study *a class* of models rather than individual models, and so no unique shape can be assigned to the signal we are looking for, other than general qualities such as, for example, an excess of leptons in the purely leptonic \cancel{L} -SUSY scenarios. We are therefore not in a position to optimize the analysis with respect to exactly quantifiable

estimators. Of course, an analysis could be performed and optimized point by point, yet such a strategy would have to be carried out on a more general set of mSUGRA points, so as not to over-tune the analysis to exactly the points considered, risking to loose sensitivity to points not studied. Moreover, more is perhaps learned by generalizing and looking for common discriminators than spending a large effort studying closely hundreds of scenarios which may have nothing to do with what the experiment finds. This is the real motivation why the last part of the analysis is done using neural networks. They serve to approximate dedicated search strategies for specific scenarios.

Let us begin by considering which backgrounds are most important. Firstly, QCD $2 \rightarrow 2$ processes and Z/W production have the highest cross sections. As before, we mean by Z/W the sum of Z and W production. Secondly, one must expect that the more mass there is in an SM event, the more dangerous it is when trying to look for heavy physics. $t\bar{t}$ production, $ZZ/ZW/WW$ production, and Higgs production are examples of heavy SM backgrounds. Again, by $ZZ/ZW/WW$ production is meant the sum of ZZ , ZW , and WW production. The Higgs is not expected to be extremely dangerous, since its mass will presumably be known before LHC SUSY searches begin, and since the cross sections are low (e.g. $\sigma(Z/W + h^0) = 2.5 \times 10^{-9}$ mb for $m_H = 115$ GeV). With respect to the large lepton and jet multiplicity as well as large \cancel{E}_T , one could well ask how significant triple gauge production could be as background. Unfortunately, these production cross sections are not yet implemented in PYTHIA, and so we are forced to give a rough estimate based on the α_{EW}^2 suppression, i.e. a factor 10^{-4} relative to $ZZ/ZW/WW$ production. This brings the cross section down to about 10^{-11} mb. Special cuts designed to catch pairs of jets or leptons with Z or W invariant masses and requiring that the p_T of a jet or a lepton be larger than ≈ 50 GeV (see below) would most likely bring this contamination down by at least a factor ten more. Furthermore, we shall see that even the double gauge events give a negligible contribution to the background at the end of the analysis, and so I conclude it safe to disregard this background when the SUSY cross section is larger than 10^{-12} mb. For lower cross sections than this, it would be advisable to conduct a dedicated study of how the triple gauge background can be dealt with, but in such regions, the total number of SUSY processes recorded by the ATLAS detector will also be so small that the LHC is at the limit of its capabilities (see point 7 in the table below), and so for such studies to be meaningful, full detector simulation as well as much more dedicated (i.e. specialized) search strategies are necessary.

The numbers of events used in the analysis are shown in tables 7 and 8 together with cross sections, the number of generated events passing trigger thresholds, and the number of events expected after an integrated luminosity of 30 fb^{-1} has been collected. As can be seen, the number of events expected for P_7 is only around 100. This is most likely too low for ATLAS to see anything, yet the mass hierarchy in the model is interesting, and so we include it in the analysis to give an example of the performance of this type of model under the tested cuts.

QCD processes with the p_T of the hard interaction in its rest frame below 100 GeV were not possible to include in the analysis, since none of the events generated for the trigger studies passed the selected trigger thresholds. Though the statistical uncertainty on 0 events clearly does not make sense to define, a conservative estimate on the maximal number of events passing triggers can be obtained by noting that a Poisson distribution with mean $\mu = 2.99$ has less than 5% probability of resulting in 0 events, and so we estimate the event numbers by scaling 3 events out of each of the generated $p_T < 100$ GeV samples to 30 fb^{-1} of data taking. This brings us to conclude that at most 1.9×10^7 events

SM Process	σ [mb]	N_{gen}	N_{trig}	$N(30 \text{ fb}^{-1})$	$N_{\text{trig}}(30 \text{ fb}^{-1})$
QCD $2 \rightarrow 2$					
$p_T < 100 \text{ GeV}$	70	—	—	2×10^{15}	$< 10^5$
$p_T = 100 - 150 \text{ GeV}$	1.42×10^{-3}	1.0×10^8	320	4.26×10^{10}	$(1.4 \pm 0.1) \times 10^5$
$p_T > 150 \text{ GeV}$	2.88×10^{-4}	3.1×10^7	5.6×10^3	8.64×10^9	1.7×10^6
Z/W	1.19×10^{-3}	1.8×10^8	4.1×10^4	3.57×10^{10}	8.1×10^6
$t\bar{t}$	6.08×10^{-7}	5.9×10^6	8.1×10^5	1.82×10^7	2.6×10^6
$ZZ/ZW/WW$	1.16×10^{-7}	5.9×10^6	1.5×10^5	3.48×10^6	8.9×10^4

Table 7: Cross sections and event numbers for SM processes. N_{gen} is the total number of generated events, and N_{trig} is the number passing trigger thresholds. The fourth column simply contains the cross section multiplied by 30 fb^{-1} and the last is the number of generated events passing trigger thresholds scaled to 30 fb^{-1} of data taking: $N_{\text{trig}}(30 \text{ fb}^{-1}) = N_{\text{trig}} \times N(30 \text{ fb}^{-1})/N_{\text{gen}}$. For the lowest p_T QCD sample, none of the generated events passed triggers. The estimate of less than 10^5 events is discussed in the text. For the intermediate p_T QCD sample, the number of generated events passing triggers was so low that the associated statistical uncertainty is shown with the scaled number. No correction for pile-up is included in these numbers.

in the region $1 \text{ GeV} < p_T < 10 \text{ GeV}$, 5.0×10^6 events in the region $10 \text{ GeV} < p_T < 75 \text{ GeV}$, and at most 4.9×10^4 events in the region $75 \text{ GeV} < p_T < 100 \text{ GeV}$ could pass trigger thresholds with a 5% chance that we would not have seen them in the trigger analysis. Though these numbers are statistically sound, the estimates for the two lowest p_T samples are likely to be gross overestimates. That particles from the first class of events should be able to gain enough p_T through parton showering, hadronization, and detector resolution alone to pass any of the triggers here used borders on the impossible. With respect to events from the second class ($10 - 75 \text{ GeV}$), we note that the \cancel{E}_T triggers used *begin* at 75 GeV with the further requirement of hard, isolated leptons and that the jet triggers require either 3 jets of each $50 \text{ GeV } p_T$ or 1 jet with $p_T = 100 \text{ GeV}$, and so it is also here excessively unlikely to see events passing into the active trigger range. Towards the high end of the p_T region, though, and for the third class of events, there are clearly some events in the far extremes of the distributions which will pass trigger thresholds. Estimating the upper bound on this number to be ten times that estimated for the third class of events alone seems the best guess possible at the moment, and so we arrive at an estimated maximum of 10^6 $p_T < 100 \text{ GeV}$ QCD events which are not included in the analysis. Assuming, pessimistically, that these events will have the same rejection factors under the cuts applied below as the $p_T = 100 - 150 \text{ GeV}$ QCD sample, we will see that an additional 10^6 low- p_T QCD events will not significantly affect the conclusions of the analysis.

No attempt at including the effects of pile-up has been implemented in the analysis. Generally speaking, pile-up results in smearing of the measured calorimeter energies. Acknowledging that this would shift more events into the active trigger range than out of it, we made a guess at an overall factor of 5/3 for the trigger study, i.e. the rates obtained for $L = 3 \times 10^{33} \text{ cm}^{-2}\text{s}^{-1}$ without smearing were multiplied by this number to obtain a

mSUGRA Point	σ [mb]	N_{gen}	N_{trig}	$N(30 \text{ fb}^{-1})$	$N_{\text{trig}}(30 \text{ fb}^{-1})$
P_2	1.3×10^{-10}			3900	
MSSM		10^5	8.9×10^4		3500
LLE		10^5	9.9×10^4		3900
nLLE		10^5	9.8×10^4		3800
LQD		10^5	9.4×10^4		3700
nLQD		10^5	9.4×10^4		3700
P_7	3.9×10^{-12}			114	
MSSM		10^5	8.2×10^4		94
LLE		10^5	9.9×10^4		113
nLLE		10^5	9.9×10^4		113
LQD		10^5	9.8×10^4		111
nLQD		10^5	9.7×10^4		111
P_9	2.4×10^{-8}			720000	
MSSM		8.2×10^5	6.7×10^5		590000
LLE		8.4×10^5	8.0×10^5		690000
nLLE		8.2×10^5	7.3×10^5		640000
LQD		8.4×10^5	5.9×10^5		510000
nLQD		8.4×10^5	5.7×10^5		490000
P_{12}	1.1×10^{-10}			3300	
MSSM		10^5	8.8×10^4		2900
LLE		10^5	9.9×10^4		3300
nLLE		10^5	9.7×10^4		3200
LQD		10^5	8.8×10^4		2900
nLQD		10^5	8.6×10^4		2800
F_2	1.1×10^{-10}			3300	
MSSM		10^5	6.1×10^4		2000
LLE		10^5	9.7×10^4		3200
nLLE		10^5	8.8×10^4		2900
LQD		10^5	7.1×10^4		2300
nLQD		10^5	6.0×10^4		2000

Table 8: Cross sections and event numbers for mSUGRA. Since single sparticle production is not included, the choice of a scenario with or without $\cancel{L}\cancel{L}$ does not affect the production cross sections. The LLE/LQD models correspond to the models in column *a* of table 5 and the nLLE/nLQD to column *c*. The models in column *b* are generally so similar to the ones in column *a* that they have been left out of this table. The same goes for the LLE+LQD models which simply interpolate between the LLE and LQD scenarios. No correction for pile-up is included in these numbers.

more realistic estimate. This was done noting that:

$$R(thres) \propto \int_{thres}^{\infty} dp_T \phi_{smeared}(p_T) = C(thres) \int_{thres}^{\infty} dp_T \phi(p_T) \quad (33)$$

i.e. the rate passing a certain threshold is proportional to the integral from that threshold to infinity of the smeared distribution of events, which can be written as a (threshold-dependent) constant times the integral of the unsmeared distribution, or in simpler words:

a number can always be written as a constant times another number. In the last section, we assumed $C(thres) = 5/3$. In the analysis, however, we are looking at the distributions themselves rather than their integrals. Simply pre-weighting each background event by $5/3$ rather than 1, independent of p_T , does not give a reliable estimate, since most of the events smeared into the trigger range will lie just above the p_T thresholds. Also, smearing will cause some signal events to look like they have lower p_T and some to look like they have higher p_T . The net effect of smearing on the signal distributions is currently not clear. Therefore, rather than attempting some best-guess strategy which would in any case end up rather poor, we do not attempt to include smearing at all in the present analysis. This will cause the number of background events to be underestimated, most notably at low p_T . This is not deemed a serious effect since the rejection factors from the cuts placed are close to 100% for low p_T events. The cause for worry lies at higher p_T where smearing will cause background and signal events to look more alike, making the purities of the signals extracted in the analysis too optimistic. As we shall see, however, we will not be close to the 5σ discovery border in any of the scenarios, meaning that the effects of pile-up will not significantly alter the conclusions reached.

One further note: Due to limited space, it is of course impossible to show detailed plots and results for every variant of the λ couplings for every point in mSUGRA space here, but it helps to notice that we are trying to discriminate between particles maximally as heavy as the top and particles which are typically heavier. The greatest degree of confusion therefore must arise when the sparticles are relatively light, and so we show detailed results only for P_9 in the following subsections. Since the P_9 production cross section is relatively higher than the cross sections for the other points, this means that the absolute number of events passing cuts is something of a maximum, yet keep in mind that P_9 is typically the point where any cut takes away the largest fraction of SUSY events. In order to still give an impression of the spread between the various other SUSY scenarios, less detailed plots are shown with the full range of models included.

5.3.1 Missing Transverse Energy

In R -conserving scenarios, LSP's escaping detection give rise to a powerful signature in \cancel{E}_T . Even when R is violated, escaping neutrinos can give an enhancement relative to the SM processes. The total background distribution after 30 fb^{-1} and its composition is illustrated for $\cancel{E}_T < 400$ in figure 13a. Note that the double gauge events are so few in number that they are not even visible in the plot. This is a feature which carries through to the end of the analysis. The mSUGRA P_9 \cancel{E}_T -distributions for MSSM, LLE, and LQD scenarios are shown in 13b. As can clearly be seen, the background with the highest cross sections, single gauge production, has an \cancel{E}_T distribution which is sharply peaked at 0 while the $t\bar{t}$ and high p_T QCD processes have more broad distributions. The sharp rises at $\cancel{E}_T = 75\text{ GeV}$ and $\cancel{E}_T = 175$ are due to the me75 and me175 triggers becoming active.

In figure 13c, the full range of supersymmetric models investigated are plotted for LLE, LQD, and the MSSM, respectively. As mentioned above, these plots are not intended to give detailed information, only to illustrate the spread between the various scenarios. Smoothed curves have been used rather than histograms since it would otherwise be impossible to disentangle the various models. In the LLE and LQD scenarios, three curves are drawn for each mSUGRA scenario corresponding to the three different \cancel{L} coupling strength scenarios. Due to the very different cross sections of the mSUGRA points, the plots have been normalized to equal areas so that it is the fractions of events

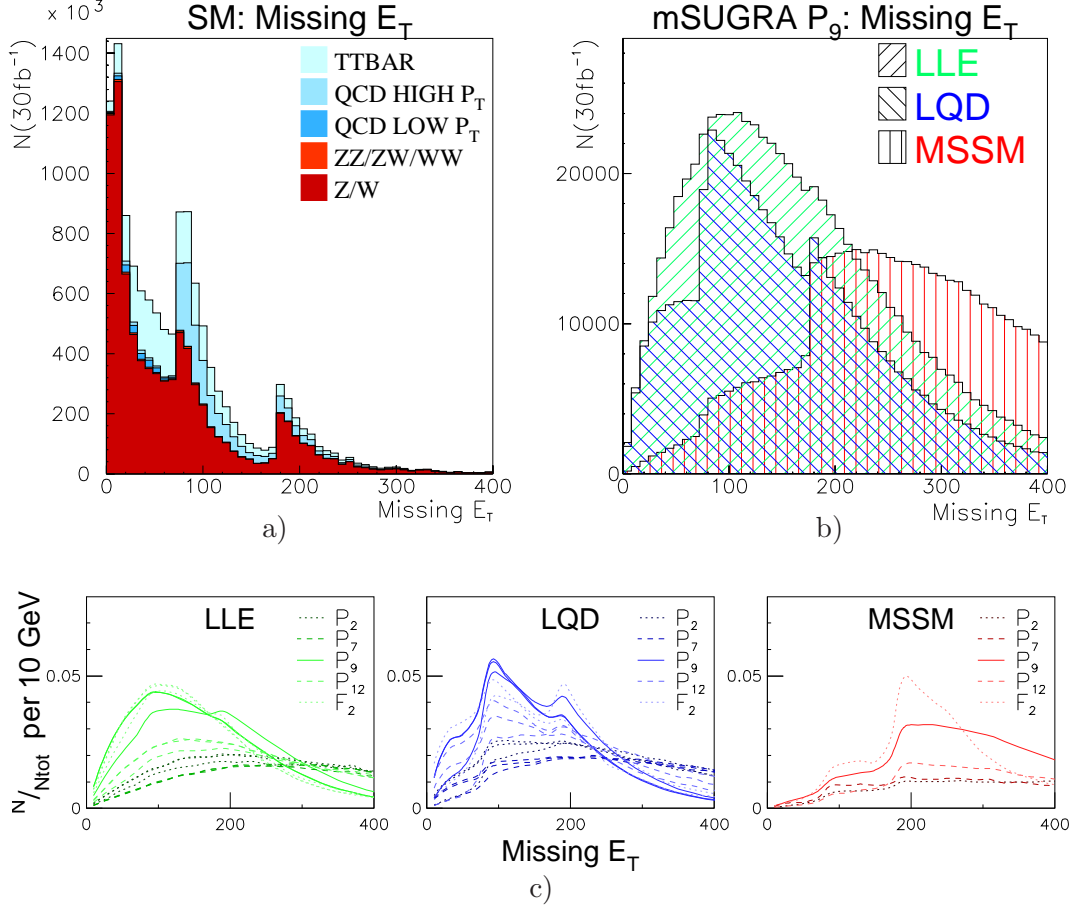


Figure 13: a) and b): \cancel{E}_T signatures for SM and SUSY processes normalized to 30fb^{-1} of data taking. “QCD LOW p_T ” means events from the $100\text{GeV} < p_T < 150\text{GeV}$ sample and “QCD HIGH p_T ” events from the $p_T > 150\text{GeV}$ sample. Note the large difference in vertical scale between the two SM plots. c): Event distributions normalized to unit area for LLE, LQD, and the MSSM for all mSUGRA and \cancel{E}_T coupling points studied (commented further in the text).

per 10 GeV which are plotted. In the LLE scenarios, the sharp rises at 75 and 175 GeV just mentioned are absent, since these scenarios do not rely as heavily on the \cancel{E}_T triggers as the two others.

Cuts on $\cancel{E}_T > 50\text{GeV}$, $\cancel{E}_T > 100\text{GeV}$, $\cancel{E}_T > 150$, and $\cancel{E}_T > 200\text{GeV}$ were investigated with results shown in table 9. The models are: MSSM, LLE (all λ couplings at 10^{-2}), LQD (all λ' couplings at 10^{-2}), nLLE (natural λ couplings, defined by eq. (31)), and nLQD (natural λ' couplings). Note that the number of triggered SM events given in table 9, 13 million, is not equal to $10^7\text{s} \times 2.1\text{Hz}$ since we are not including the factor of $5/3$ from pile-up here. Note also that the estimated number of SM events *do not* include $p_T < 100\text{GeV}$ events. As an explicatory note to what one sees in this table, it is not surprising that the MSSM does best under these cuts since escaping neutralinos give extra \cancel{E}_T . What really is noteworthy is that the R -Violating models, in spite of neutralino decays, do so well. With regard to what happens in the other mSUGRA models, only F_2 has lower efficiencies. F_2 is a special case in the sense that it represents a class of models where one really has only

EVENTS PASSING CUTS ON \cancel{E}_T .

	SM	P_9 MSSM	P_9 LLE	P_9 nLLE	P_9 LQD	P_9 nLQD
$N_{trig}(30 \text{ fb}^{-1})$	$(13 \pm 0.1) \text{ M}$	590 k	685 k	640 k	500 k	490 k
$\cancel{E}_T > 50 \text{ GeV}$	$(7.3 \pm 0.1) \text{ M}$	580 k	450 k	620 k	600 k	465 k
$\cancel{E}_T > 100 \text{ GeV}$	$(3.4 \pm 0.1) \text{ M}$	560 k	350 k	480 k	510 k	380 k
$\cancel{E}_T > 150 \text{ GeV}$	$(1.9 \pm 0.05) \text{ M}$	520 k	240 k	340 k	390 k	270 k
$\cancel{E}_T > 200 \text{ GeV}$	$(910 \pm 30) \text{ k}$	450 k	280 k	220 k	280 k	175 k
$\frac{N_{\text{post}}}{N_{\text{pre}}}$	0.26	0.95	0.70	0.70	0.80	0.79

Table 9: Event numbers passing cuts on \cancel{E}_T for several cut values with associated statistical errors, normalized to 30 fb^{-1} of data taking. “M” and “k” are the standard abbreviations for $\times 10^6$ and $\times 10^3$, respectively. Due to the comparatively large event samples generated for SUSY, the statistical uncertainties on the SUSY numbers are below the percent level, and so no uncertainties are shown. The selected cut of 100 GeV is marked in bold, and the ratio of events surviving after this cut to events generated is shown for each model.

a very few species of particle with low mass available, the rest having very high masses so that the \cancel{E}_T spectrum becomes peaked at low values despite the large GUT parameters.

Taking a look at the first row of table 9, one notices that a 5σ discovery is immediately possible for all the P_9 points using just the event numbers passing triggers, before any attempt at purifying the sample is made. By “a 5σ discovery”, we mean exactly the following:

$$\frac{S}{\sqrt{S+B}} > 5 \quad (34)$$

where S and B are the number of signal and background events expected, respectively. In section 5.5 we discuss this estimate more closely and how the uncertainties from the limited numbers of generated events can be taken into account using 95% confidence limits. Furthermore, we will seek to include, albeit in a very crude manner, the effects of QCD uncertainties and pile-up on the discovery potential as well. Setting this aside for the moment and doing the arithmetic yields that with 500.000 signal events, we could get a 5σ discovery even with background levels a few hundred times higher. However, since we are not guaranteed to be in quite this fortuitous situation in the real world, it is worthwhile to pursue the analysis further.

After the cut on \cancel{E}_T , no events remained in the intermediate- p_T QCD sample ($100 \text{ GeV} < p_T < 150 \text{ GeV}$). To estimate the number of events in the tail beyond $\cancel{E}_T=100 \text{ GeV}$, the last 6 bins which contained events were fitted to a falling exponential, fig. 14. Assuming uncorrelated gaussian errors on the fit and dividing the integral by the bin width gives an estimated 290 ± 450 in the tail above 100 GeV, meaning that less than 10^3 events pass the cut at 95% confidence level, yielding a rejection factor for these events of at least 130 by the \cancel{E}_T cut. Applying this rejection factor to the estimated 10^6 events in the $p_T < 100 \text{ GeV}$ QCD sample and adding up yields a maximum of $(1 + 7.5) \times 10^3 < 10^4$ QCD events with $p_T < 150 \text{ GeV}$ remaining after the cut. Henceforth we refer to these 10^4 events, combined, as the low- p_T (QCD) sample.

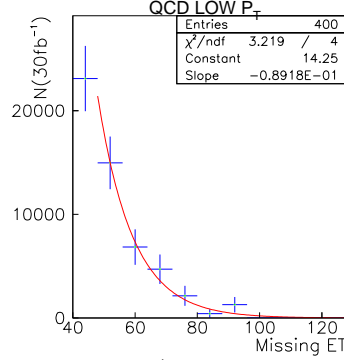


Figure 14: Exponential fit to the \cancel{E}_T tail of the low p_T QCD event sample.

5.3.2 Hard Leptons and Jets

As mentioned, a typical signature for SUSY is the large number of jets obtained. This, when combined with (possible) violation of Lepton Number, may well be accompanied by a large lepton multiplicity, and so it makes good sense to combine the analysis here. The lepton multiplicities (iso. muons + iso. electrons) in events with $\cancel{E}_T > 100$ GeV are shown in figures 15a (SM) and 15b (mSUGRA P_9 MSSM, LLE, and LQD), and an overview of the distributions in the other scenarios investigated are shown in 15c. Jet multiplicities are shown in figure 16. One sees the larger relative lepton multiplicity in LLE scenarios and the larger relative jet multiplicity in LQD scenarios. Finally, the “box” plots in figure 17 show the correlations between the number of leptons and the number of jets with large boxes meaning that a large fraction of events have the corresponding combination of N_{lep} and N_{jets} and small boxes meaning that a small fraction of events have the corresponding combination.

Based on these distributions, it seems reasonable to require at least N_J jets, at least $(N_J - 1)$ jets and at least 1 lepton, at least $(N_J - 2)$ jets and at least 2 leptons, or at least 3 leptons. Values for $N_J = 8 - 11$ have been investigated. Results are presented in table 10. For the $p_T < 100$ GeV QCD sample, applying the rejection factor of 8.5 found for the high p_T sample gives an estimated 900 events at most remaining after the cut.

As for the \cancel{E}_T cuts, it is not at all surprising that the MSSM is here the model which does the worst. After all, the MSSM has a lot of \cancel{E}_T exactly because the LSP *escapes* and does *not* give rise to extra jets and/or leptons. Note also that we have power to discriminate between MSSM, \cancel{R} with dominant LQD terms, or \cancel{R} with dominant LLE terms in these variables. This, however, is saved for the neural network analysis below.

Additional variables which are obvious as discriminators when studying the decays of heavy particles are (transverse) momenta of the hardest jets and leptons in the event. The transverse momenta of the four hardest jets and the two hardest leptons are therefore also used as inputs in the neural net analysis. For events with less than 4 jets and/or less than 2 leptons, the value 0 is assigned to the “missing” jet and lepton p_T ’s. In the cut-based analysis, we simply use the p_T of the hardest object in the event, p_T^{hard} . The SM and P_9 distributions for this variable are shown in figure 18. Cuts at $p_T^{hard} = 100, 150, 200$, and 250 were investigated with results as shown in table 11. Due to the higher resonance masses, the P_9 scenarios escape these cuts almost with impunity. The ratio of events surviving before and after the cut is even better for the rest of the mSUGRA points.

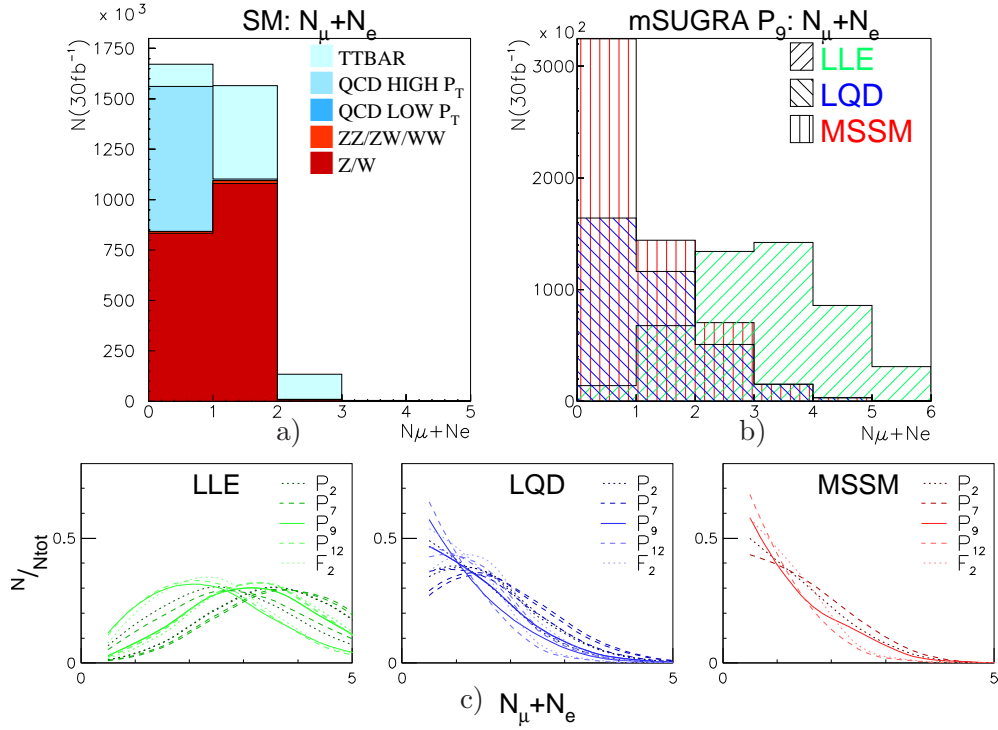


Figure 15: a) and b): Lepton multiplicities in the SM and P_9 of events surviving the cut on \cancel{E}_T . The numbering of the bins is such that the events with 0 leptons are in the bin to the right of the number 0. c): Fractional distributions of events in all scenarios investigated.

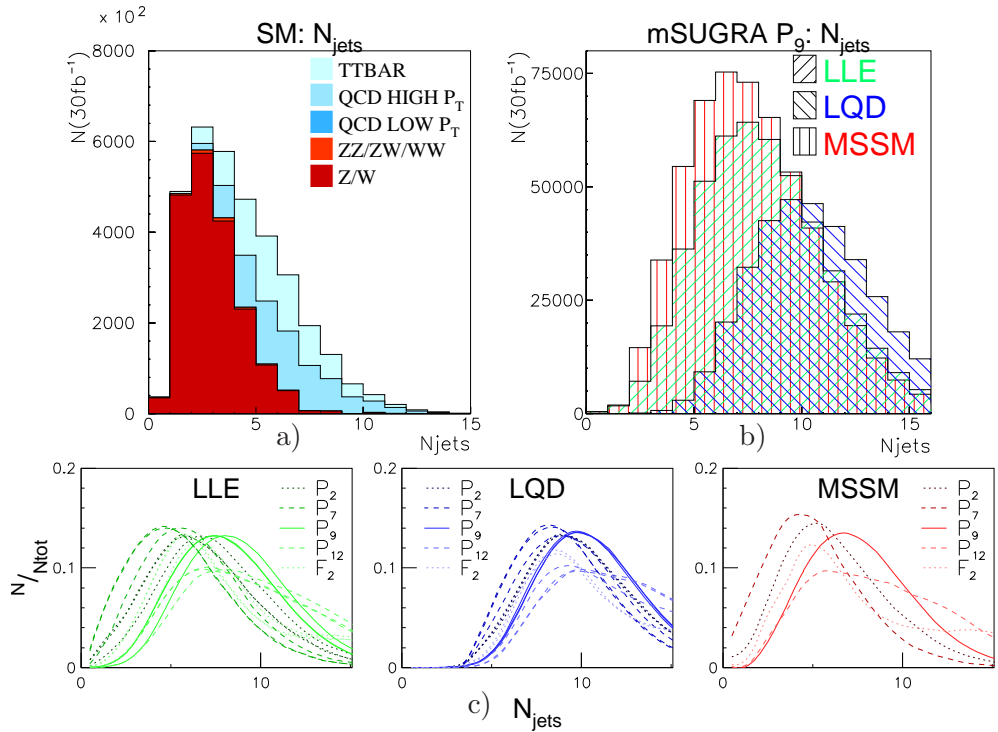


Figure 16: a) and b): Jet multiplicities in the SM and P_9 of events surviving the cut on \cancel{E}_T . c): Fractional distributions of events in all scenarios investigated.

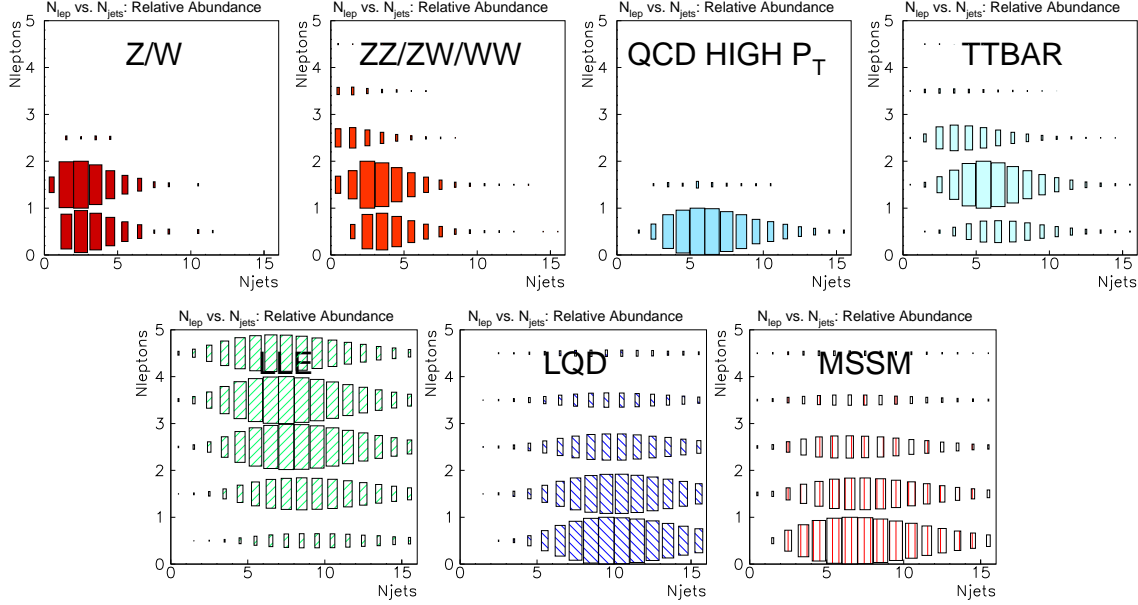


Figure 17: Lepton versus jet multiplicity (see text) in the SM and mSUGRA P_9 of events surviving the cut on \cancel{E}_T . The numbering of the bins is such that the events with 0 leptons are in the bin to the right of the number 0. The cuts investigated correspond to cutting out the lower left corner of each plot.

EVENTS PASSING CUTS ON N_{jets} AND N_{leptons} .

	SM	P_9 MSSM	P_9 LLE	P_9 nLLE	P_9 LQD	P_9 nLQD
$N_J = 8$	(200 ± 10) k	220 k	270 k	410 k	380 k	290 k
$N_J = 9$	(105 ± 4) k	160 k	230 k	380 k	340 k	240 k
$N_J = 10$	(51 ± 3) k	120 k	190 k	360 k	290 k	190 k
$N_J = 11$	(23 ± 2) k	80 k	150 k	330 k	250 k	150 k
$\frac{N_{\text{post}}}{N_{\text{pre}}}$	0.06	0.39	0.85	0.78	0.76	0.75

Table 10: Events passing cuts on N_{jets} and N_{leptons} for several choices of jet cutoff, N_J (see text). In addition, the requirement that each event pass the \cancel{E}_T cut was imposed. The selected cut is marked in bold, and the ratio of events surviving after this cut to events surviving before this cut is shown for each model. A very good rejection factor for SM events is obtained. The reason for this is plain to see in figure 17. Cutting out the lower left corner in those plots takes away the majority of Z/W events, and also a significant reduction in QCD and $t\bar{t}$ events is obtained. For the SM, the (gaussian) uncertainty due to the limited event sample is also shown.

After the cut on hardest object, only 1 Z/W event remained in the sample (out of 5×10^7 generated). As is apparent from figure 18a, it would clearly be nonsense to fit the P_T^{hard} distribution of Z/W events to thereby obtain an estimate. Rather, we use the procedure recommended by [29] that a conservative upper bound on the number, N , passing the cut is given by the mean of that Poisson distribution which yields a 5% chance of giving only one event or less surviving the cut. This gives an estimate for $N < 4.75$ at 95% confidence level, translating to 3400 events after 30fb^{-1} of data taking. With respect to the rejection factor expected for these events under subsequent cuts, we adopt

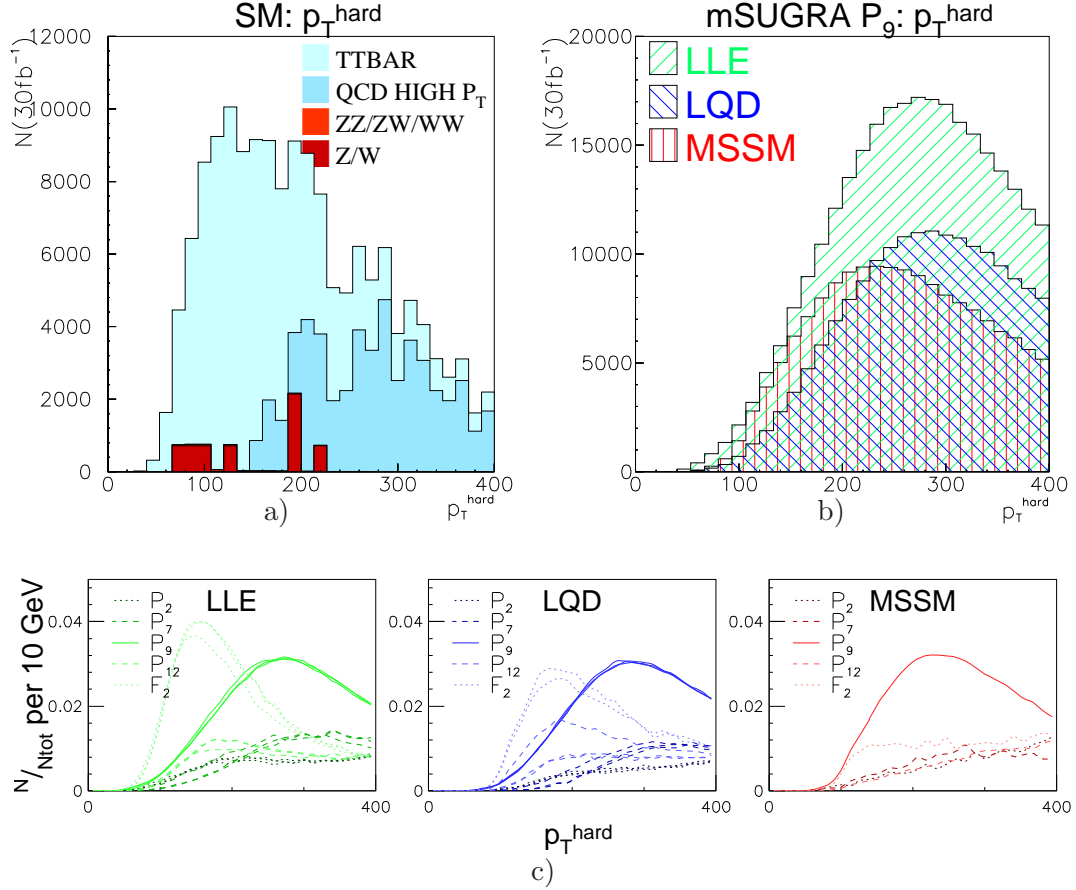


Figure 18: p_T distribution for hardest object in SM and SUSY, normalized to 30fb^{-1} of data taking. Events shown are the ones surviving previous cuts.

EVENTS PASSING CUTS ON p_T^{hard} .

	SM	P_9 MSSM	P_9 LLE	P_9 nLLE	P_9 LQD	P_9 nLQD
$p_T^{\text{hard}} = 100$	$(180 \pm 10) \text{ k}$	220 k	410 k	380 k	270 k	290 k
$p_T^{\text{hard}} = 150$	$(140 \pm 10) \text{ k}$	200 k	390 k	370 k	270 k	280 k
$p_T^{\text{hard}} = 200$	$(110 \pm 5) \text{ k}$	180 k	360 k	330 k	250 k	260 k
$p_T^{\text{hard}} = 250$	$(85 \pm 4) \text{ k}$	140 k	300 k	270 k	210 k	220 k
$\frac{N_{\text{post}}}{N_{\text{pre}}}$	0.57	0.80	0.86	0.85	0.90	0.90

Table 11: Events passing cuts on p_T^{hard} for several choices of cut value. The selected cut is marked in bold, and the ratio of events surviving after this cut to events surviving before this cut is shown for each model.

a slightly pessimistic assumption, reducing the number of events by the same factor as the double gauge events ($ZZ/ZW/WW$). Before leaving the Z/W events, we take one more look at figure 18a. It is here evident that there are 3 events *just* below the cut, and one might argue that our estimate of 3400 events is therefore likely to be too optimistic. This argument is incorrect since by using that knowledge we would invalidate the statistical approach just used. As long as the cut was not tuned to lie exactly above these events (and 200 was chosen only for its being a nice round number), the Poisson approach is

statistically sound.

For the low- p_T QCD events, the low rejection factor, 1.07, found for the high p_T sample gives an estimated negligible reduction of event numbers by the p_T^{hard} cut. One must recall, however, that the high p_T QCD sample consists entirely of events where the hard scattering gave rise to $p_T > 150$ GeV in the CM of the scattering. It is therefore quite natural that almost no reduction is accomplished for these events by demanding that the p_T of the hardest object in the event be larger than 200 GeV. For the low- p_T QCD sample, we expect the reduction from this cut to be significantly greater, yet to be conservative, we use the same rejection as for the high p_T sample, yielding maximally 420 events remaining.

5.3.3 LSP Decay Signature

The \cancel{R} scenarios give us one extra possible signature for SUSY events which is not present in the R -conserving cases, LSP decay. Out of necessity, we shall here focus on the case of a neutralino LSP. This means that we are looking for 3-body decays, a more difficult situation than for 2-body decays. It is, of course, impossible to say whether the lightest neutralino decays into $qq\nu$, qql , or $\ell\ell\nu$ without making assumptions about the relative coupling strengths, something which is obviously not acceptable when one is interested in defining as general a search strategy as possible. Whatever coupling is dominant, there are maximally two neutrinos in an event with double neutralino decay (see section 3). One would therefore expect to see at least 4 hard jets/leptons with energies not greatly differing from each other. We therefore introduce the following measure for this “4-object energy correlation”:

$$E_{4C} \equiv \frac{1}{3} \left(\frac{E_4}{E_3} + \frac{E_3}{E_2} + \frac{E_2}{E_1} \right) \quad (35)$$

where E_{1-4} are the energies of the 4 hardest objects (leptons or jets) in the event ordered in energy, the hardest being E_1 . Events with $N_{lep} + N_{jet} < 4$ are assigned the value zero. Following the above line of reasoning we would expect the SUSY events to have 4-object correlations close to 1. In contrast, there is no reason to expect this kind of correlation in e.g. Z/W or QCD events. Also, a large number of double gauge events will have low or zero values since two gauge bosons decaying leptonically *at most* produce 4 hard objects in the detector. The $t\bar{t}$ events, however, are quite indistinguishable from many of the SUSY scenarios in this variable. Noting that the more massive a particle is, the larger the momentum kicks given to its decay products will be, one would expect that particles coming from the decays of objects heavier than the top would, on average, have larger p_T than particles coming from top decays. We can use this to give the variable just defined some extra discriminating power against $t\bar{t}$ events. However, it comes at a cost. A look in table 4 reveals that P_9 , for instance, has the LSP and several other SUSY particles *lighter* than the top. By giving the 4-object energy correlation some p_T dependence, we will not only get rid of top events, we will also be throwing away signal events for SUSY scenarios with low-mass particles. This is not a serious drawback, since we can afford to lose a certain amount of signal in the low-mass scenarios due to the relatively high production cross sections. In return, we get a more pure signal for the heavier scenarios where we don’t have so many signal events and so require a better background rejection.

This is the basis for using the 4-object energy correlation multiplied by the average p_T of the four hardest objects rather than the 4-object energy correlation alone, and so we

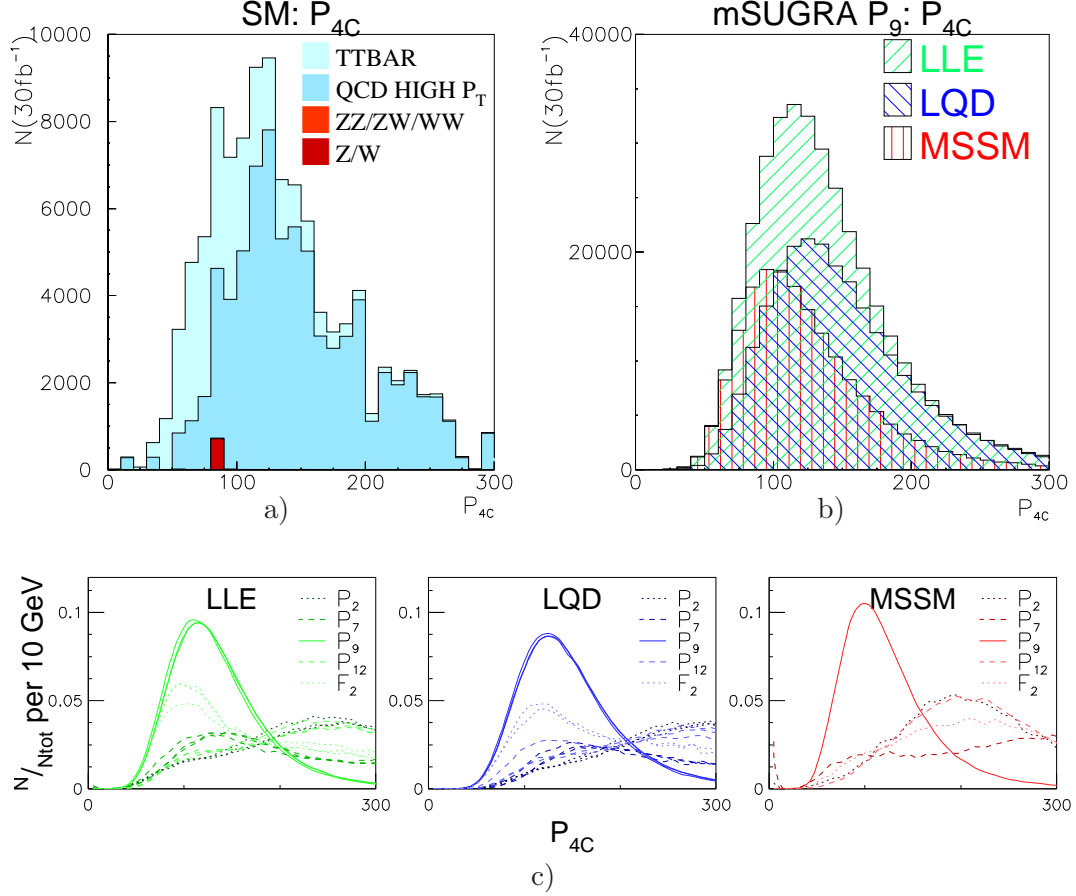


Figure 19: Distributions of P_{4C} in the SM (a and b) and for mSUGRA P_9 . All events used survive previous cuts.

introduce the p_T -weighted 4-object energy correlation:

$$P_{4C} \equiv \frac{1}{12} \left(\frac{E_4}{E_3} + \frac{E_3}{E_2} + \frac{E_2}{E_1} \right) (p_{T1} + p_{T2} + p_{T3} + p_{T4}) \quad (36)$$

The suspicion that the low-mass scenarios will not do well in this variable is quickly verified by taking a look at figure 19c where peaks around 100 GeV are seen for both P_9 and F_2 whereas the heavier scenarios show more flat distributions.

For SUSY events where double LSP decay does not occur, note that there must be either one or more heavier particles decaying directly to SM particles or R -parity is conserved. In the first case, the E_i/E_j will generally be lower, since jet/lepton energies are presumably not equal to so great an extent, but since heavier particles are decaying, the average p_T will be larger, evening out the score. The R -conserving scenarios will look more like the SM in this variable, since no LSP decay occurs.

For the high- p_T QCD and the double gauge events, rejection factors of 1.2 and 2.7, respectively, were found, yielding an estimated maximum of 350 low- p_T QCD events and 1300 Z/W remaining.

EVENTS PASSING CUTS ON P_{4C} .

	SM	P_9 MSSM	P_9 LLE	P_9 nLLE	P_9 LQD	P_9 nLQD
$P_{4C} > 50$	(108 ± 5) k	170 k	350 k	330 k	250 k	260 k
$P_{4C} > 75$	(97 ± 5) k	160 k	330 k	310 k	240 k	250 k
$P_{4C} > 100$	(79 ± 4) k	110 k	270 k	240 k	210 k	220 k
$P_{4C} > 125$	(57 ± 4) k	72 k	190 k	170 k	160 k	160 k
$\frac{N_{\text{post}}}{N_{\text{pre}}}$	0.72	0.65	0.77	0.84	0.75	0.83

Table 12: Events passing cuts on P_{4C} for SM and P_9 events surviving previous cuts, scaled to correspond to 30 fb^{-1} of data taking. The selected cut is marked in bold, and the ratio of events surviving after this cut to events surviving before this cut is shown for each model. One sees that the MSSM for does even worse than the SM for P_9 , due to the absence of LSP decay. The rest of the mSUGRA points generally have acceptances close to 100% even for the MSSM. The only exception is F_2 which nonetheless lies above 80% in all cases.

5.3.4 Thrust

One may intuitively understand that pair production involving less massive particles is liable to produce decay products which lie more “on a line” than processes involving more massive particles (where the decay products get larger momentum kicks). It is based on this that thrust is expected to be of use as a discriminating variable. Its value is defined as:

$$T = \max \left\{ \frac{\sum_i |p_i \cdot \vec{n}|}{\sum_i |p_i|} \right\} \quad (37)$$

where i runs over all particles in the event and \vec{n} is a unit vector along an arbitrary axis. The axis which maximizes the expression is defined as the thrust axis. For a completely pencil-shaped event, the thrust value is 1, going down to 0.5 for an event where the momenta are evenly distributed throughout the detector. The thrust distributions for events satisfying the previous cuts are shown in figure 20. Cuts on $T < 0.75$, $T < 0.8$, $T < 0.85$, and $T < 0.90$ were investigated. Results are shown in table 13. The selected cut, $T < 0.85$, is marked in bold. Rejection factors of 2.0 and 2.1 were obtained for the high p_T QCD events and the double gauge sample, respectively, yielding 180 low- p_T and 620 Z/W events maximally remaining. Note that the Z/W events would most likely have higher rejections under this cut than their double gauge counterparts, yet finding it difficult to

EVENTS PASSING CUTS ON THRUST.

	SM	P_9 MSSM	P_9 LLE	P_9 nLLE	P_9 LQD	P_9 nLQD
$T < 0.75$	(10 ± 2) k	35 k	75 k	77 k	76 k	80 k
$T < 0.8$	(24 ± 2) k	59 k	130 k	130 k	120 k	130 k
$T < 0.85$	(40 ± 3) k	83 k	190 k	180 k	160 k	170 k
$T < 0.90$	(62 ± 4) k	100 k	240 k	220 k	190 k	200 k
$\frac{N_{\text{post}}}{N_{\text{pre}}}$	0.51	0.73	0.69	0.74		

Table 13: Events passing cuts on thrust for three values of thrust cutoff. The selected cut is marked in bold, and the ratio of events surviving after this cut to events surviving before this cut is shown for each model.

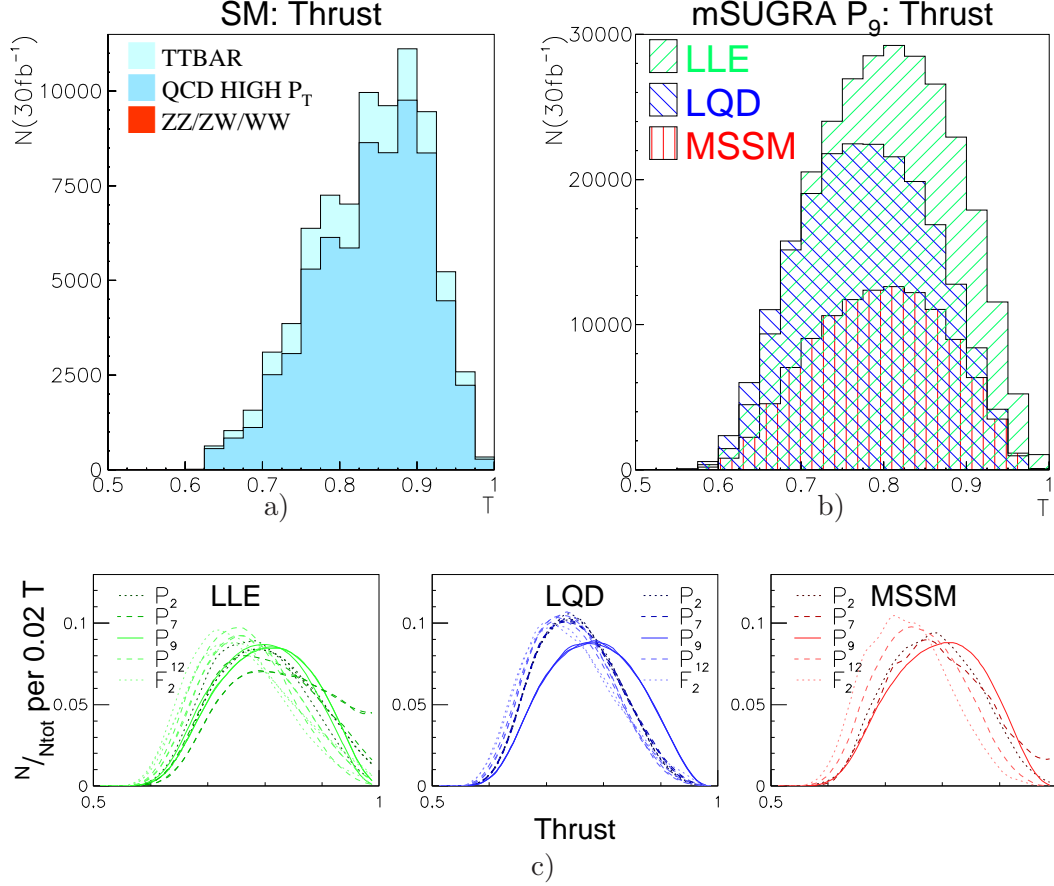


Figure 20: Thrust distributions for SM processes and mSUGRA P_9 . Observe that the QCD processes peak around 0.9 whereas P_9 peaks around 0.8. All events used survive previous cuts.

quantify it, we do not include any additional suppression in the estimated number.

5.3.5 Oblateness and Circularity

Having defined the thrust axis for each event, one can take one step further and define Major and Minor axes in the plane perpendicular to the thrust axis in exactly the same way as thrust was defined:

$$\text{Major} = \max \left\{ \frac{\sum_i |p_i \cdot \vec{n}|}{\sum_i |p_i|} \right\} \quad (38)$$

where the maximum is now to be found perpendicular to the thrust axis. The Minor axis is then fixed as the axis perpendicular to both the thrust and Major axes, yet its value is computed exactly like thrust and Major values. These definitions of the Major and Minor axes, used at e^+e^- colliders, get into trouble at a pp machine like the LHC where variables sensitive to boosts along the z -axis are of very limited use. At pp machines, one therefore defines the Major and Minor axes to lie orthogonal to the z -direction. This means that the Major axis will most often just be the projection of the thrust axis onto the (x, y) plane. A measure for how “spread out” the event is in the (x, y) plane is then given by subtracting the Minor from the Major, yielding the *oblateness*, O .

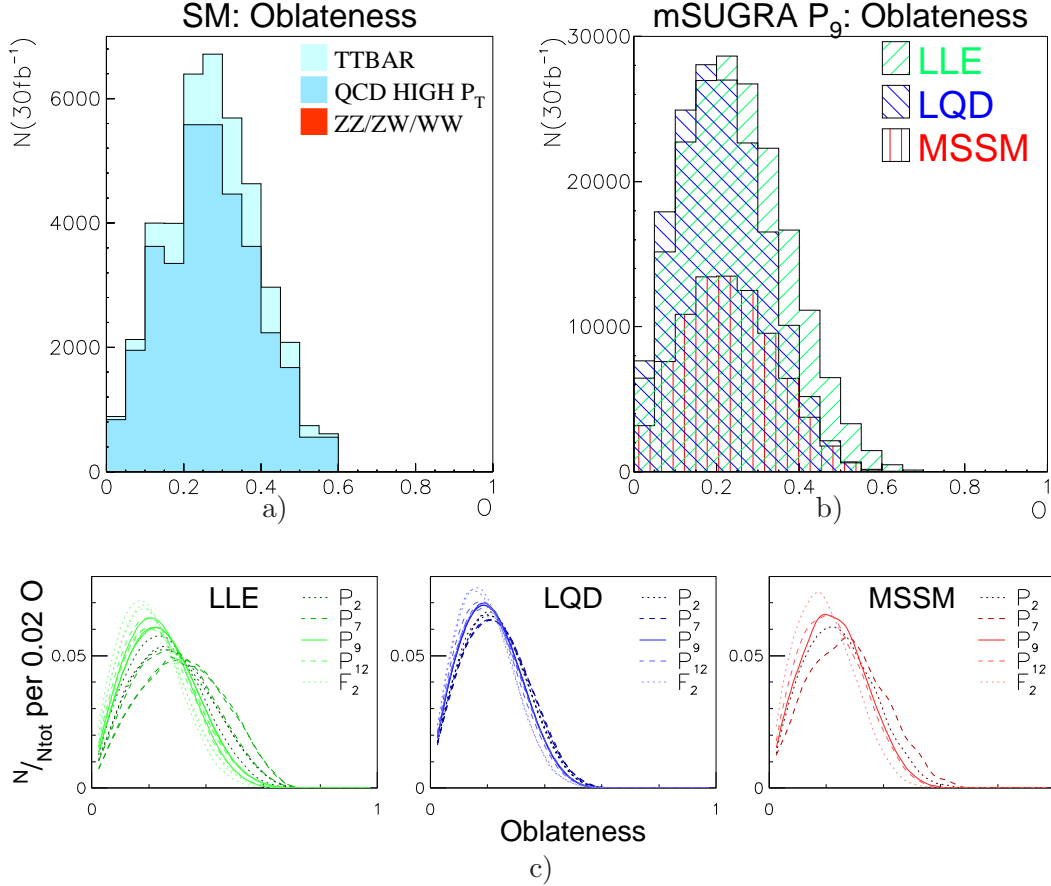


Figure 21: Oblateness distributions for SM processes and mSUGRA P_9 . Observe that the QCD processes peak around 0.3 whereas P_9 peaks around 0.2. All events used survive previous cuts.

Essentially, the oblateness compares the fraction of p_T in the direction where most p_T is going and the fraction in the direction where least p_T is going. An event with low oblateness is an event in which the p_T is evenly distributed in the (x, y) plane, and an event with high oblateness has its p_T concentrated around the direction of the Major axis. Based on the same arguments that led us to introduce a p_T dependence on the 4-object energy correlation, we expect SUSY events to have lower oblateness values than SM events, again with a tradeoff involved between signal loss at low SUSY masses and background rejection for higher SUSY masses. Distributions are shown in figure 21. The effect of requiring the oblateness to be lower than 0.25, 0.3, 0.4, and 0.5 were investigated with results as given in table 14.

A remarkable feature of the plots in figure 21c is that P_7 , by far the heaviest mSUGRA point, has oblateness distributions which are *broader* than the lower-mass points. To understand the reason for this, a closer look was taken at the event histories for high-oblateness events in an nLLE P_7 scenario. A plausible explanation is that the extremely massive resonances in P_7 are produced more often than not with p_T less than their masses. When we argued above that we would expect low oblateness for events containing more massive resonances, we implicitly assumed that the original direction of flight of the resonances would define the Major axis around which a non-zero Minor value would be generated by the decay of the resonances in proportion to their masses. But for resonances

EVENTS PASSING CUTS ON OBLATENESS.

	SM	P_9 MSSM	P_9 LLE	P_9 nLLE	P_9 LQD	P_9 nLQD
$O < 0.25$	(17 ± 2) k	49 k	100 k	100 k	110 k	110 k
$O < 0.3$	(24 ± 2) k	61 k	130 k	130 k	130 k	140 k
$O < 0.4$	(34 ± 3) k	77 k	170 k	160 k	160 k	160 k
$O < 0.5$	(40 ± 3) k	83 k	180 k	180 k	160 k	170 k
$\frac{N_{\text{post}}}{N_{\text{pre}}}$	0.84	0.92	0.88	0.95	0.91	0.95

Table 14: Events passing cuts on oblateness, normalized to 30fb^{-1} of data taking. The selected cut is marked in bold, and the ratio of events surviving after this cut to events surviving before this cut is shown for each model.

with masses as heavy as those found in P_7 (around 2 TeV) this argument is turned upside down. At P_7 , the (two-body) decays of the resonances produce momentum kicks of such large magnitudes that the original direction of flight can be completely erased, resulting in events looking roughly as depicted in figure 22 in the (x, y) plane.

The last event shape variable used in this work is the circularity, again a transverse version of a variable commonly used in e^+e^- colliders, the sphericity [67]. It is similar, but not identical, to 1 minus oblateness, in that events which have their p_T evenly distributed in the transverse plane have high circularities and events with more uneven distributions low circularities. Having cut away the highest oblateness events, we try to catch a few more fish (background events) by cutting away the lowest circularity events as well. It is defined through the eigenvalues of the circularity matrix:

$$C = \frac{1}{\sum_i (p_T^i)^2} \begin{bmatrix} \sum_i (p_x^i)^2 & \sum_i p_x^i p_y^i \\ \sum_i p_y^i p_x^i & \sum_i (p_y^i)^2 \end{bmatrix} \quad (39)$$

where i runs over the reconstructed particles/jets in the event. The Circularity value is defined as twice the smallest eigenvalue of this matrix, making it a measure of the momentum fraction along the smaller of the principal axes. The distributions of events in the SM and SUSY surviving all previous cuts can be seen in figure 23. Taking a look at the very first few bins of the plots, one sees that circularity does indeed have some discriminating power beyond what was contained in the oblateness though it has not been

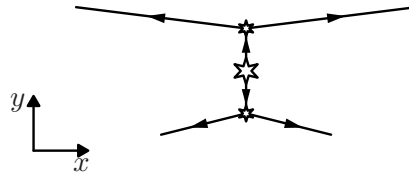


Figure 22: Decay of a pair of extremely massive resonances, projected onto the (x, y) momentum plane. Here, the decay products of the upper resonance have their momenta oriented predominantly along the x axis, whereas the lower have larger fractions in the z direction. In cases like this, the x axis is close to being the Major with only little p_y to generate a sizeable Minor.

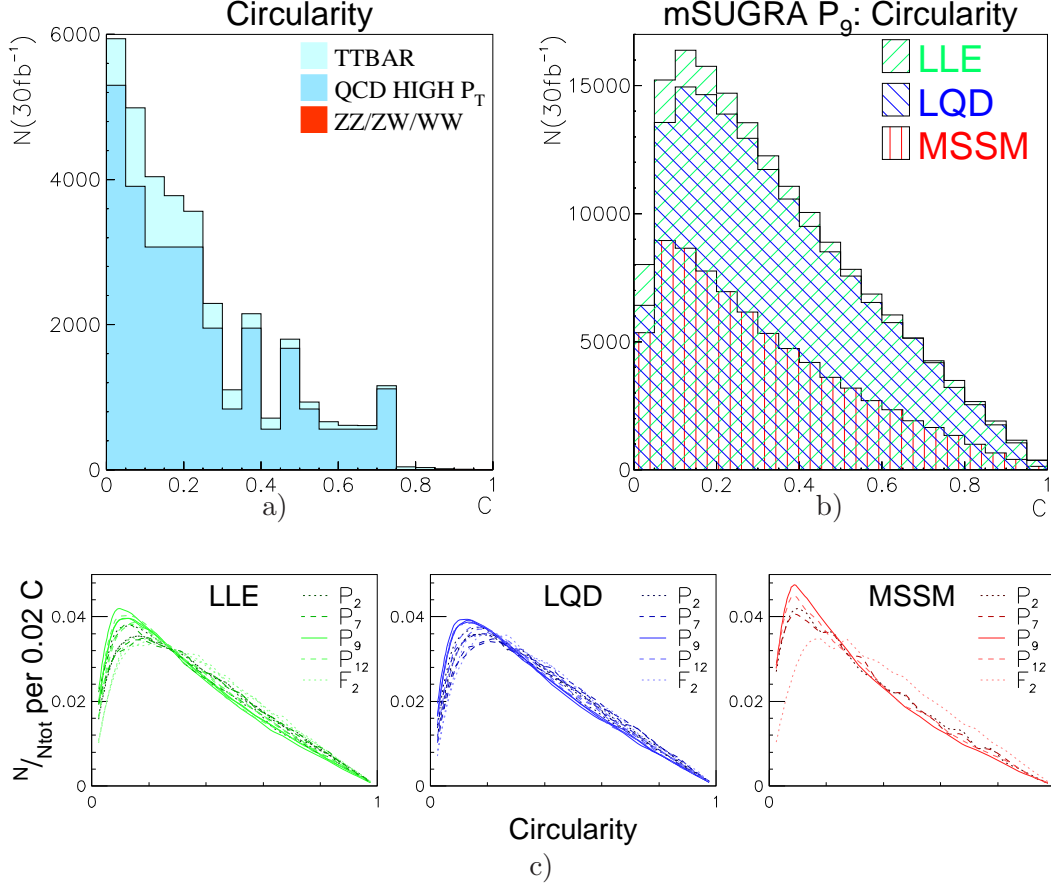


Figure 23: Circularity distributions for SM and mSUGRA scenarios. Observe that the number of QCD events rises almost linearly with C as one goes to smaller C whereas the mSUGRA distributions peak around $0.1 - 0.2$. All events used survive previous cuts.

EVENTS PASSING CUTS ON CIRCULARITY.

	SM	P_9 MSSM	P_9 LLE	P_9 nLLE	P_9 LQD	P_9 nLQD
$C > 0.05$	$(29 \pm 3) \text{ k}$	72 k	160 k	160 k	150 k	150 k
$C > 0.10$	$(24 \pm 2) \text{ k}$	63 k	140 k	140 k	140 k	140 k
$C > 0.15$	$(20 \pm 2) \text{ k}$	54 k	130 k	120 k	120 k	120 k
$C > 0.20$	$(16 \pm 2) \text{ k}$	46 k	110 k	110 k	110 k	110 k
$\frac{N_{\text{post}}}{N_{\text{pre}}}$	0.68	0.81	0.86	0.84	0.87	0.86

Table 15: Events passing cuts on circularity, normalized to 30fb^{-1} of data taking. The selected cut is marked in bold, and the ratio of events surviving after this cut to events surviving before the cut is shown for each model. Note that only 70 high- p_T QCD events remain after the cut, and so the gaussian errors used here will be replaced by Poisson statistics in what follows.

possible to identify the cause. Cuts requiring a circularity greater than 0.05, 0.1, 0.15, and 0.20 were investigated with results shown in table 15.

A last thing worth noticing about the circularity is that whereas the thrust and the oblateness are *linear* in the momenta, circularity is quadratic. This means that two events

which are identical in every respect except that one parton in the first event is replaced by two collinear partons with some sharing of the momentum in the other will not have the same circularities, since $(p_a + p_b)^2 \neq p_a^2 + p_b^2$. This, in turn, means that the circularity is sensitive to uncertainties in the fragmentation model (where such splittings occur), in contrast to thrust and oblateness.

The combined rejection factors under the oblateness and circularity cuts were 1.7 and 1.6 for the high- p_T QCD and double gauge events respectively. We thus estimate a maximum of 110 and 400 low- p_T and single gauge events remaining, respectively. These numbers should be compared to 4000 $t\bar{t}$ and 20000 high- p_T QCD events. Based on the 22 generated double gauge events remaining, an upper limit of 31.4 events can be set using the conservative Poisson estimate discussed in section 5.3.2, translating to a maximum of 20 events after 30fb^{-1} of data taking. One thus sees that the double gauge events are completely negligible as background, giving some justification of the earlier made statement that triple gauge events should also be negligible.

5.4 Pattern Recognition with Neural Networks

We now turn to the more specialized part of the analysis where we shall seek to extract signals for LLE, LQD, and MSSM SUSY scenarios separately using three neural networks trained to recognize the specific event shapes associated with each scenario. The results of the analysis are presented in section 5.5. Here, we concentrate on the structure and function of neural networks and their application to the present problem, essentially one of pattern classification. Does this event “look” like a Standard Model event, or does it look like a SUSY event?

5.4.1 What Neural Networks Do

The first step in any analysis based on cuts is to find as optimal variables as possible to place cuts on, the second step to find the optimal *placements* of the cuts. What neural networks do is to *learn* which variables to use and where to place the cuts, based on a teaching sample of background and signal events. The simplest type of network consists of a single neuron which computes a linear combination of the input variables in the problem, in our case the discriminating variables just discussed. It then places a cut on this “activation level” and returns 1 if the activation was above the cut value and 0 otherwise. In our case, these two outputs would correspond to the event having been classified as either a signal or a background event. The learning algorithm then serves to adjust the coefficients in the linear combination and the placement of the cut according to the average error the network makes over the learning sample such that next time it goes over the sample it will classify more events correctly. The way this works is by a procedure called “gradient descent” where the network calculates the gradient of the error squared, or some other function that one wishes to minimize, with respect to each network parameter. It then adjusts each parameter, taking a small step in parameter space in the minimizing direction each time it has processed an event or, to decrease the effect of insignificant fluctuations, it sums up the required changes over a number of processed events before it applies them. This latter approach smoothes out the otherwise jittering movement of the network across parameter space, often allowing faster progress towards the minimum.

For gradient descent to work, note that the neuron cannot be allowed to compute a sharp cut on its activation level, since the step function is discontinuous and hence not

differentiable. Instead, one uses so-called sigmoidal functions which look like smoothed out versions of the step function. We consider these functions and the gradient descent algorithm in more detail below, yet let us first extend our network beyond just a single neuron.

In problems where the classification is not quite so easy that it can be performed using a cut on just one linear combination of the inputs, more neurons are needed, each one computing a sigmoidal function of its activation level, resulting in an output from each of these “cut neurons” between zero and one. These outputs then serve as inputs to the output neuron who sums them up in a new linear combination, the output neuron activation. In the present case, this activation is used directly as the network output, alternatively one may let the output neuron compute a function of its input. It remains that the computing power of the network lies in the cut neurons. A function may or may not be handy to apply to the output, but it will not increase the amount of information there is in the output value. It now also becomes apparent why the cut neurons are customarily referred to as hidden neurons. The world outside the network interacts with it by giving it input on the input neurons and by reading the output from the output neuron. The cut neurons communicate only with other neurons. Henceforth, we refer to these internal neurons as hidden neurons.

The function of a neural network is thus nothing but a number of smoothed cuts on the same number of linear combinations of the inputs, with the results of the cuts being used as variables in a last linear combination defining the output of the network – similar to what is being done in an ordinary cut-based analysis. The benefit is that neural networks automatically pick up correlations and anti-correlations between arbitrarily many of the input variables. A hypothetical example of high-dimensional correlations would be if we imagine that many signal events have high jet multiplicities when there is little \cancel{E}_T in the event, but that they have very few jets when \cancel{E}_T is high. Furthermore, let us suppose that, at high \cancel{E}_T a certain fraction of signal events with few jets have high lepton multiplicities, but that at low \cancel{E}_T high lepton multiplicities would be a characteristic of background events, unless there was also a high thrust in the event, or failing that at least a high oblateness. These correlations would of course follow from physical arguments related to the processes involved in shaping the hypothetical background and signal processes in this example, and linear combinations of the variables designed to make use of the correlations could be constructed and optimized manually, yet this would be an extremely time-consuming task considering the more than 50 different scenarios investigated in this work. Moreover, it is a task which neural networks are ideally suited for by construction.

5.4.2 Network Layout and Network Learning:

For each event to be processed, each of the discriminating variables defined above are presented as inputs to the network. Since the network is initialized with random weights between 0 and 1, it is sensible to scale these inputs to typically lie in the range $[0, 1]$ as well for faster learning. Otherwise, the input-to-hidden weights (the coefficients in the linear combination mentioned above) have to be corrected, possibly for a long time, until the right ball-park is found. The input normalizations used here are listed in table 16. The hidden layer in most applied networks normally has fewer neurons than the input layer, representing that some generalization can already be made at this stage: it is not always necessary to form N linear combinations of N variables since some mutual interdependence can usually be eliminated. In the present analysis with 14 inputs, it is found that a network

i	1	2	3	4	5	6	7
In_i	$\frac{E_T}{200}$	$\frac{N_{\text{jets}}}{15}$	$\frac{N_{\mu}^{\text{iso}}}{5}$	$\frac{N_e^{\text{iso}}}{5}$	$\frac{P_{4C}}{500}$	Thrust	Circularity
i	8	9	10	11	12	13	14
In_i	Oblateness	$\frac{p_{T,\text{jet}}^1}{100}$	$\frac{p_{T,\text{jet}}^2}{100}$	$\frac{p_{T,\text{jet}}^3}{100}$	$\frac{p_{T,\text{jet}}^4}{100}$	$\frac{p_{T,\ell}^1}{100}$	$\frac{p_{T,\ell}^2}{100}$

Table 16: Inputs to the neural network and their normalizations. In the text, i is used as an index denoting input neurons and In_i the value of the input variable as given in this table. Note that In_i is not necessarily identical to the output of the input neuron which we denote by I_i . P_{4C} is defined in section 5.3.3, $p_{T,\text{jet}}^{1-4}$ are the transverse momenta of the four hardest jets, and $p_{T,\ell}^{1-2}$ of the two hardest leptons.

with 10 hidden neurons performs with negligible loss of discriminating power compared to networks with more hidden neurons. As described above, each hidden neuron computes a sigmoidal of its activation level, the name sigmoidal coming from the tilted S shape of these functions. The particular sigmoidal used in this work is the logistic function (the most commonly used). This function assigns an output value for the j 'th neuron in the hidden layer of:

$$H_j = \frac{1}{1 + e^{-\sum_{i=1}^{N_{\text{in}}} (I_i w_{ij}) - \delta_j^H}} \quad (40)$$

where I_i is the output of the i 'th input neuron, w_{ij} is the weight of the synapse connecting input i to hidden neuron j , δ_j^H is a bias term for the hidden neuron, and N_{in} is the number of neurons in the input layer. Henceforth, we follow the convention that subscript i refers to the input layer whereas subscript j refers to the hidden layer. The slope of the sigmoid is sometimes also adjusted by introducing a “temperature”, T :

$$H_j = \frac{1}{1 + e^{-\left(\sum_{i=1}^{N_{\text{in}}} (I_i w_{ij}) - \delta_j^H\right)/T_j}} \quad (41)$$

The effect of this modification is shown in figure 24. However, since introducing a temperature different from unity simply corresponds to rescaling all the weights connecting to H_j and the bias by a common factor $1/T_j$, there is nothing gained by introducing such a parameter. Moreover, the network becomes slower and there is the risk that it begins

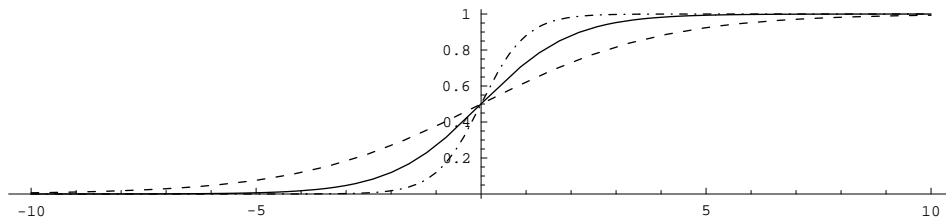


Figure 24: The logistic (sigmoid) function for $T = 2$ (dashed), $T = 1$ (solid), and $T = 0.5$ (dot-dashed).

to oscillate between changing T_j and rescaling the weights in the learning procedure, and so we stick with eq. (40). For the input neurons, only a bias is added to the value of the input variables:

$$I_i = \text{In}_i - \delta_i^I \quad (42)$$

Taking one more look at figure 24 one also sees the reality of the earlier made comment that these functions look like smoothed out step functions and so can be regarded as smooth versions of cuts. The complete network layout looks as depicted in figure 25.

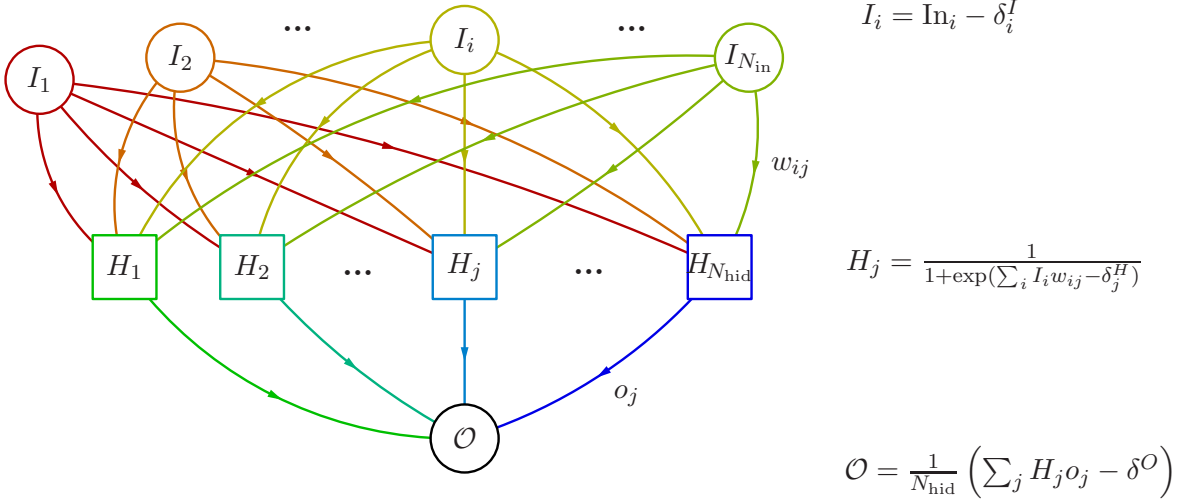


Figure 25: Layout of the neural networks used in the final part of the analysis (before brain-damage – see below).

5.4.3 Network Training

The neural networks used in this work all learn by adjusting their synaptic weights and biases in the direction which minimizes the error squared of the network, the error being defined on an event-by-event basis by:

$$e = t - \mathcal{O} \quad (43)$$

where t is the target output (0 for background, 1 for signal), and \mathcal{O} is the output that was actually obtained for the event.

As the name implies, the *gradient descent* learning algorithm [77] consists of a learning rule defined by taking a step in weight space in the direction of the gradient of the (squared) error:

$$p \rightarrow p + \Delta p = p - \alpha \frac{\partial e^2}{\partial p} = p + 2\alpha e \frac{\partial \mathcal{O}}{\partial p} \quad (44)$$

where p represents any of the adjustable parameters in the network, e is the error on the output, and α is a learning rate parameter specifying how large steps the network takes. This rule does not necessarily have to be applied immediately after each event in the learning sample has been processed. In order to wash out sharp, irregular changes called for from extreme events in the distributions, possibly pulling in opposite directions, we do

better in accumulating the parameter changes over some processing period before invoking them. After the period, the *accumulated* change to each parameter is invoked, and the accumulated error is reset. In order to get as little statistical noise in the parameter changes as possible, the period was here set to be the number of events in the learning sample. Denoting event number by n , the learning rule above becomes:

$$p \rightarrow p + \Delta p = p + 2\alpha \sum_n e(n) \frac{\partial \mathcal{O}(n)}{\partial p} \quad (45)$$

One further improvement can be made on the learning rule. Seeing as two successive changes to the parameters of the network often go in roughly the same direction in parameter space, we add a mixture of the last parameter change to the current change, something which often increases the learning speed of the network:

$$p \rightarrow p + \Delta p = p + 2\alpha \sum_n e(n) \frac{\partial \mathcal{O}(n)}{\partial p} + \beta \Delta p^{\text{last}} \quad (46)$$

where Δp^{last} is the change which was made after the previous period, and $\beta < 1$ specifies the “inertia” of the system. We are now ready to specify the learning rules for each of the parameters of the network in fig. 25. These can be easily derived (using the chain rule).

$$\begin{aligned} \frac{\partial \mathcal{O}}{\partial \delta^O} &= -1/N_{\text{hid}} & \frac{\partial \mathcal{O}}{\partial o_j} &= \frac{H_j}{N_{\text{hid}}} \\ \frac{\partial \mathcal{O}}{\partial \delta_j^H} &= o_j H_j (H_j - 1) & \frac{\partial \mathcal{O}}{\partial w_{ij}} &= \frac{o_j}{N_{\text{hid}}} H_j (1 - H_j) I_i \\ \frac{\partial \mathcal{O}}{\partial \delta_i^I} &= I_i (1 - I_i) \sum_j o_j H_j (H_j - 1) w_{ij} \end{aligned} \quad (47)$$

Replacing these quantities back into eq. (46) directly yields the required learning rules.

5.4.4 Optimal Brain Damage

As described above, the first derivatives of the squared error with respect to the network parameters are used in training by gradient descent. It was shown by LeCun, Solla, and Denker [78] that the *second* derivatives can be used to trim the network by getting rid of the most redundant parameters. This is desirable since redundant parameters are the ones that will eventually cause the network to overfit the sample space. This can have a severe effect on the generalizational ability of the network, i.e. its performance on data samples it has not been in contact with during the learning process. The idea of Optimal Brain Damage is to introduce a measure for how much the squared error will change as a result of deleting each network parameter. The parameters whose deletion will have the least effect can then be discarded if over-fitting is a problem. The measure proposed in [78] is the *saliency*, defined for the network parameter p as:

$$s_p = \frac{p^2}{2} \frac{\partial^2 e^2}{\partial p^2} \quad (48)$$

This definition is appropriate when the learning process is near its end and the network is almost in the minimum (otherwise a more general formula would apply. See [78]). The

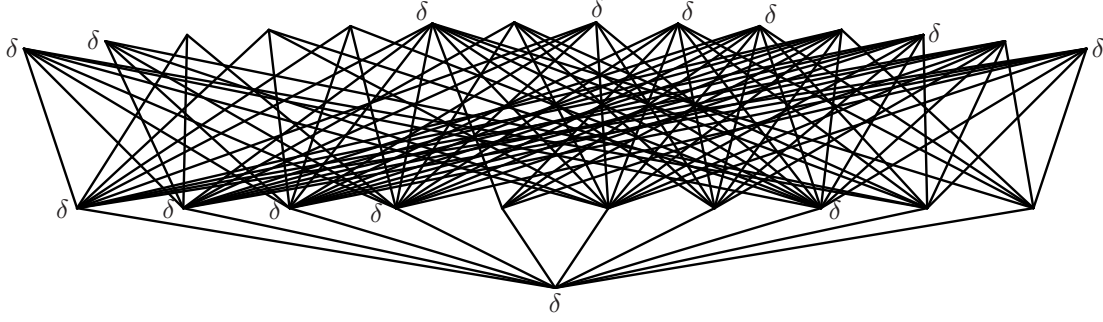


Figure 26: Sketch of the MSSM network after brain damage. Neurons with biases still on are shown with the symbol δ . The numbering of the inputs goes from left to right.

procedure is quite simple. One begins with a network that contains many parameters. One then trains it and deletes the parameters with lowest saliency. The resulting, “brain-damaged”, network is then retrained until it converges. This procedure is repeated until a satisfactory compromise between the mean squared error and the generalizational ability of the network is found. As a side benefit, the finished network contains fewer parameters and is therefore faster to run. What happens is typically that the smallest coefficients in the linear combinations forming the hidden neuron activations get thrown away while the larger coefficients are kept. The diagonal second derivatives of the parameters for the present network are:

$$\frac{\partial^2 e^2}{\partial(\delta_i^I)^2} = \frac{2}{N_{\text{hid}}} \left[\left(\sum_{j=1}^{N_{\text{hid}}} w_{ij} H_j o_j (1 - H_j) \right)^2 - e \left(\sum_{j=1}^{N_{\text{hid}}} w_{ij}^2 o_j H_j (1 - H_j (3 - 2H_j)) \right) \right] \quad (49)$$

$$\frac{\partial^2 e^2}{\partial w_{ij}^2} = \frac{2}{N_{\text{hid}}} I_i^2 H_j o_j (o_j H_j (1 - H_j)^2 + e(1 - H_j (3 - 2H_j))) \quad (50)$$

$$\frac{\partial^2 e^2}{\partial(\delta_j^H)^2} = \frac{2}{N_{\text{hid}}} H_j o_j (o_j H_j (1 - H_j)^2 + e(1 - H_j (3 - 2H_j))) \quad (51)$$

$$\frac{\partial^2 e^2}{\partial o_j^2} = \frac{2H_j^2}{N_{\text{hid}}} \quad (52)$$

$$\frac{\partial^2 e^2}{\partial(\delta^O)^2} = \frac{2}{N_{\text{hid}}} \quad (53)$$

Each of the networks used thus started out with 14 inputs (= 14 biases), 10 hidden units (= 10 biases), 140 input-to-hidden synapses, 10 hidden-to-output synapses, and a bias on the output for a total of 175 parameters. Approximately a quarter of the parameters can be deleted with very little effect on the mean squared error of the networks over the learning samples, but with an increase in convergence rate and processing speed. An example of a finished, brain-damaged network, the one used for MSSM recognition, is illustrated in figure 26.

To improve the convergence rate, two further improvements were made in the design. Firstly, a fixed learning rate is not optimal since there may be regions in “error space” which look like endless plateaus to one whose legs are not long enough. The network was therefore equipped with the ability to increase its learning rate if the relative change in the squared error (averaged over the learning sample) after a learning cycle is small. A

little experimenting showed an error change of less than 5% from cycle to cycle to be a good indicator of when a larger learning rate was needed. Secondly, unlimited growth is not desirable. At the other side of a plateau, a mountaneous region may yet exist, and so a mechanism to decrease the rate is also included. If the error change is greater than zero, meaning that the error *increases*, the network “concludes” that it has taken too big a step, unlearns the direct effects of the last learning step (“direct” here meaning that the effects of the momentum term are not unlearned) and goes forward again with a smaller learning rate. After some more experimenting to reach a good balance between increase and decrease, this technique proved highly efficient, typically improving the convergence rate by factors of ten.

5.5 Results

As the last item on the agenda, results for signal extraction in all \mathbb{Z} -SUSY scenarios studied are now presented. For this purpose, three networks were constructed and trained to recognize MSSM, LLE, and LQD signals respectively. Approximately 8000 background events, scaled to represent approximately 10^7 events in the learning algorithm, and 6000 signal events were used in each training process, all events required only to have passed the triggers. The relative numbers of signal and background events, as seen by the learning algorithm, are thus fairly similar to the post-trigger event numbers expected for SUSY cross sections around 10^{-10} mb. For the LQD network, the background numbers were scaled by twice as much to obtain a better rejection factor in view of the less clean signatures of the LQD couplings. For each sample, half of the events were set aside as an independent sample on which the performance of the network was tested for over-fitting cycle by cycle. A typical learning curve is shown in figure 27, together with the gradually improving separation of the two distributions early on in the learning process (only discernible in colour).

Selecting for each network events with network outputs above 0.9, we obtain a number of signal and background events for which we define the statistical significance of the signal (which we shall call the discovery potential) by:

$$P = \frac{S}{\sqrt{S+B}} \quad (54)$$

where B should be understood as the number of background events, N , coming out of the analysis plus 1.64 standard deviations to account for the statistical uncertainty related to the limited number of generated events, 1.64 being chosen since 95% of a gaussian distributed event sample will lie below the mean plus 1.64σ . For low numbers of generated events, we use the conservative Poisson estimate discussed in section 5.3.2 to reach the same 95% confidence on B . If P is above 5 for any of the networks, we draw the preliminary conclusion that a 5σ discovery is possible.

In reality, P should be corrected for QCD uncertainties and the effects of pile-up, and so we can only be confident that a 5σ discovery is possible if P is somewhat larger than 5. Therefore, aside from working with the definition, eq. (54), we attempt to obtain a more believable estimate by including the effects of pile-up and QCD uncertainties in a very crude, *ad hoc* manner. To accomplish this, we now take a look at why eq. (54) is a reasonable quantity to use for the statistical significance. When we ask for a 5σ discovery, we are really asking that the background hypothesis be more than 5 standard deviations away from the number of observed events. Assuming the event numbers to be gaussian

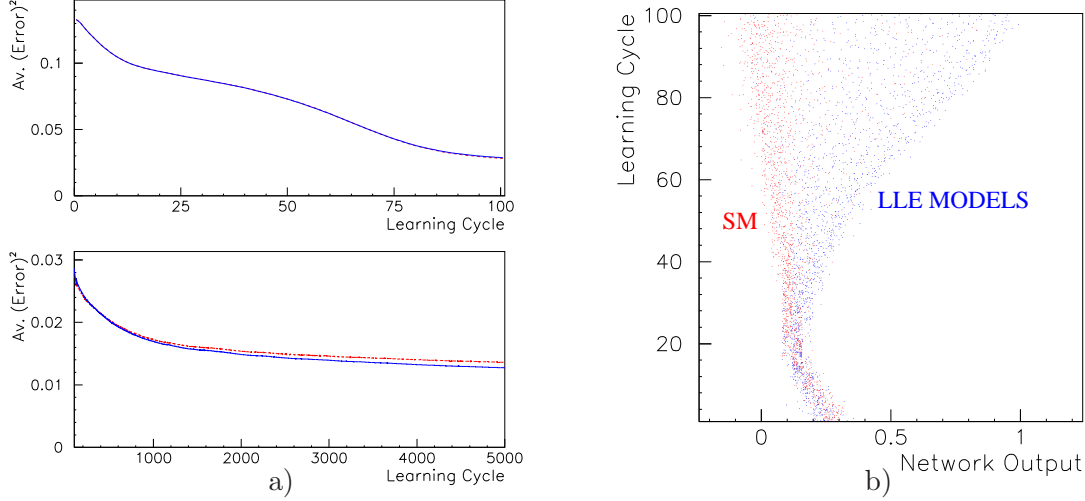


Figure 27: a) Learning Curves for the LLE network, average squared error versus learning cycle. The blue curve represents the average squared error on the learning sample and the red (dashed) the performance on the independent sample. b) learning cycle versus network output. Each red point represents an SM event and each blue point a SUSY event. In the beginning, the network is not capable of distinguishing between them, yet it quickly learns to separate the two distributions.

distributed, we arrive at the requirement:

$$\begin{aligned}
 N_{obs} - 5\sigma_{N_{obs}} &> B \\
 \Rightarrow S + B - 5\sqrt{S+B} &> B \\
 \Rightarrow P = \frac{S}{\sqrt{S+B}} &> 5
 \end{aligned} \tag{55}$$

Note that other definitions are also possible. One could equally well ask that the background plus $5\sqrt{B}$ should be less than the observed number, resulting in more optimistic P values for larger numbers of signal events.

The problem with pile-up lies in that the ratio of signal to background events passing the analysis is too optimistic. To include an estimate of the reduction of this ratio, we rewrite eq. (55) to:

$$P = \frac{\sqrt{S}}{\sqrt{1+B/S}} > 5 \tag{56}$$

where we include the effects of pile-up by multiplying B/S by some factor. That twice as many background events per signal event could be passing the analysis if pile-up was included seems a reasonably pessimistic guess. Furthermore, assuming that the intrinsic uncertainty on both S and B coming from uncertainties on QCD parameters will, to a first approximation, work in the same direction and with a comparable magnitude for both B and S , we expect that the denominator in the above formula is not affected by this uncertainty, and so we include the QCD-related uncertainties by reducing the number of signal events in the numerator by a factor of 1.5. This yields the following form for the

Process	$B_{MSSM-net}$	$B_{LLE-net}$	$B_{LQD-net}$
Low- p_T QCD	5	5	5
High- p_T QCD	840	840	840
Z/W	150	150	150
$t\bar{t}$	210	140	100
ZZ/ZW/WW	5	5	5
Total SM	1210	1140	1100

Table 17: Estimated maximal event numbers remaining after network cuts. Maximal here means that the Poisson estimate discussed in section 5.3.2 has been used to estimate B as the mean of the distribution that would result in 5% probability of getting the number of generated events or less which remained in the event samples actually used. Since any distribution with a higher mean would have less than 5% probability of resulting in the generated numbers, this is equivalent to saying that we have 95% confidence in the numbers here being maximal.

“corrected discovery potential”:

$$P_{corr} = \frac{S}{\sqrt{1.5S + 3B}} \quad (57)$$

Both P and P_{corr} will be listed in the results below.

As was indeed the purpose, the network classifications gave very few background events with outputs above 0.9. The response to background events surviving the cut-based analysis over the entire output range is shown in figure 28. For all three networks, no QCD

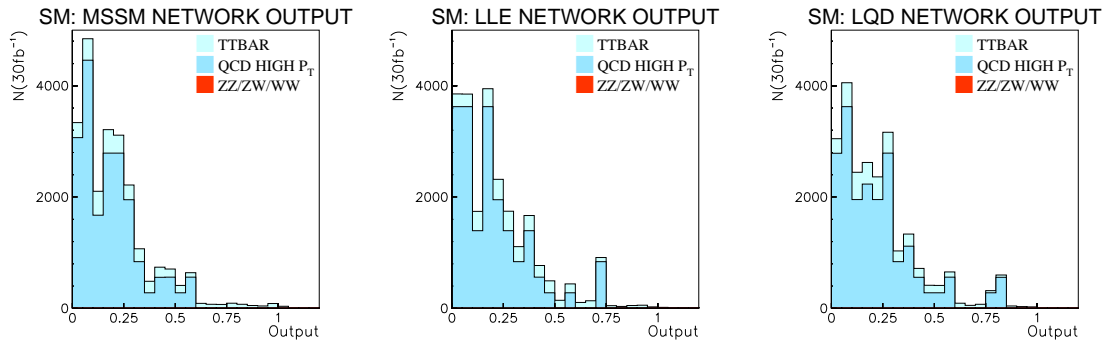


Figure 28: Network outputs for background events. As for the previous plots, the numbers of double gauge events are too small to be visible. We include them in the legend merely to signify that they have been taken into account.

events survived the cut at 0.9. Knowing that the network is a highly non-trivial function, especially near 0 and 1, we do not attempt to fit the distribution. Rather, we note that zero events has less than 5% probability of coming from a distribution with mean larger than 2.99. Adopting and scaling this estimate yields the numbers given in table 17. The same kind of Poisson estimate was used for the double gauge events, mainly to estimate the rejection factor which should be applied to the remaining single gauge events. Also for

the $t\bar{t}$ event sample, the Poisson estimate was used where the number of generated events remaining was less than 100, else the gaussian 95% confidence estimate, $B < N + 1.64\sqrt{N}$.

The total number of background events passing each network, as listed in table 17, can now be used as upper limits on the quantity B entering eqs. (54) and (57) by which we have defined the discovery potential and the corrected discovery potential, respectively. Typically, around 500 – 1000 signal events remain after cuts for P_2 , P_{12} , and F_2 . More remain for P_9 because of the larger cross section, but not nearly as large a fraction as for the other scenarios. P_7 , of course, was impossible from the start, with only 114 events expected after 30 fb^{-1} , yet one should keep in mind that large values of the \cancel{R} couplings can lead to a significant increase in the production cross section for the heavy-mass points, P_7 and F_2 , due to single sparticle production not included in the present analysis. For a hadron machine like the LHC, this effect will be largest in the LQD scenarios since single squark production will then be possible.

The discovery potentials, corrected and uncorrected, for all scenarios are given in table 18. The labelling of the models in the table should be self-explanatory to a large extent. The subscripts a , b , and n refer to the column labels in table 5 where the \cancel{L} scenarios were defined, so that a and b are the constant coupling scenarios, and n is the scenario with natural (hierarchical) couplings. This distinction, of course, does not exist for the MSSM where no lepton number violating couplings exist. The individual numbers in the table are not extremely interesting, except for the quite significant fact that, except for P_7 , they are all above 5 for at least one of the network types. It is also of some interest to note that signals can be extracted reliably for the mixed (LLE+LQD) scenarios which neither entered in the cut optimization nor in the network training. Our estimate of the LHC discovery potential in the case of Lepton Number Violating SuperGravity scenarios is thus that a 5σ discovery is possible for cross sections down to at least 10^{-10} mb with 95% certainty when the effects of pile-up and uncertainties on QCD parameters are neglected. Depending on whether our reduced estimate of the discovery potential does a reasonable job, these uncertainties should not be able to affect this general conclusion, yet one sees that there could be cause for concern for models with non-zero LQD couplings in SUSY scenarios of the F_2 type. As mentioned above, however, one would expect single sparticle production to be enhancing the cross section for this model for large values of the λ' couplings whereas low values would mean longer LSP lifetimes and hence either secondary vertices or an MSSM-like signature if the LSP escapes detection altogether. In the first case, we would have an extra discriminating variable, and in the second we note that even in the present analysis (in which the cuts were not optimized with the MSSM in mind) we have a reduced discovery potential of up to 6.5σ for the F_2 MSSM model.

ATLAS $\cancel{t}\bar{t}$ -SUSY DISCOVERY POTENTIAL

SUSY Point	NETWORK			SUSY Point	NETWORK		
	MSSM P/P_{corr}	LLE P/P_{corr}	LQD P/P_{corr}		MSSM P/P_{corr}	LLE P/P_{corr}	LQD P/P_{corr}
P_{2a}^{LLE}	24.3/16.2	25.5/17.1	25.4/17.1	P_2^{MSSM}	10.4/6.4	10.2/6.3	10.2/6.3
P_{2b}^{LLE}	24.5/16.3	25.8/17.3	25.7/17.3	P_7^{MSSM}	0.2/0.1	0.2/0.1	0.2/0.1
P_{2n}^{LLE}	23.2/15.4	24.7/16.5	24.3/16.3	P_9^{MSSM}	136/108	121/95.9	93.5/72.8
P_{7a}^{LLE}	0.7/0.4	0.7/0.4	0.8/0.5	P_{12}^{MSSM}	16.1/10.3	15.5/9.9	16.1/10.3
P_{7b}^{LLE}	0.8/0.4	0.8/0.4	0.8/0.5	F_2^{MSSM}	9.4/5.8	9.7/6.0	10.5/6.5
P_{7n}^{LLE}	0.7/0.4	0.7/0.4	0.8/0.5				
P_{9a}^{LLE}	191/153	315/256	218/176	$P_{2a}^{LLE+LQD}$	24.3/16.2	25.9/17.4	25.8/17.4
P_{9b}^{LLE}	190/153	316/256	218/176	$P_{2b}^{LLE+LQD}$	24.5/16.3	25.9/17.4	25.9/17.4
P_{9n}^{LLE}	166/133	257/208	169/135	$P_{2n}^{LLE+LQD}$	21.4/14.0	23.2/15.4	24.2/16.2
P_{12a}^{LLE}	23.4/15.5	25.6/17.2	25.5/17.2	$P_{7a}^{LLE+LQD}$	0.8/0.5	0.8/0.5	0.9/0.5
P_{12b}^{LLE}	23.4/15.5	25.5/17.2	25.5/17.2	$P_{7b}^{LLE+LQD}$	0.8/0.5	0.8/0.5	0.9/0.5
P_{12n}^{LLE}	21.8/14.4	24.2/16.2	24.3/16.3	$P_{7n}^{LLE+LQD}$	1.0/0.6	1.0/0.6	1.1/0.6
F_{2a}^{LLE}	11.3/7.0	14.0/8.8	13.3/8.4	$P_{9a}^{LLE+LQD}$	179/143	289/234	203/164
F_{2b}^{LLE}	11.2/6.9	13.7/8.7	13.1/8.2	$P_{9b}^{LLE+LQD}$	178/143	291/236	204/164
F_{2n}^{LLE}	9.9/6.1	12.4/7.8	12.3/7.7	$P_{9n}^{LLE+LQD}$	114/89.3	132/105	111/87.0
				$P_{12a}^{LLE+LQD}$	20.7/13.6	23.8/15.8	24.3/16.3
P_{2a}^{LQD}	20.9/13.7	24.3/16.2	24.8/16.6	$P_{12b}^{LLE+LQD}$	20.8/13.6	23.8/15.8	24.4/16.4
P_{2b}^{LQD}	21.4/14.1	24.7/16.5	25.3/17.0	$P_{12n}^{LLE+LQD}$	16.5/10.6	18.5/12.0	20.8/13.7
P_{2n}^{LQD}	21.5/14.1	23.3/15.5	24.2/16.2	$F_{2a}^{LLE+LQD}$	9.0/5.5	11.9/7.4	11.9/7.5
P_{7a}^{LQD}	1.0/0.6	1.0/0.6	1.1/0.6	$F_{2b}^{LLE+LQD}$	9.0/5.5	11.7/7.3	11.8/7.4
P_{7b}^{LQD}	1.0/0.6	1.0/0.6	1.1/0.7	$F_{2n}^{LLE+LQD}$	7.1/4.3	8.9/5.5	10.4/6.4
P_{7n}^{LQD}	1.0/0.6	1.0/0.6	1.1/0.6				
P_{9a}^{LQD}	116/91.6	153/122	125/99.0				
P_{9b}^{LQD}	113/88.7	151/121	123/97.6				
P_{9n}^{LQD}	113/88.5	131/104	110/86.6				
P_{12a}^{LQD}	15.7/10.0	19.2/12.5	20.9/13.7				
P_{12b}^{LQD}	15.8/10.1	19.4/12.6	21.1/13.9				
P_{12n}^{LQD}	16.6/10.6	18.6/12.1	20.9/13.8				
F_{2a}^{LQD}	7.0/4.2	9.5/5.9	10.5/6.5				
F_{2b}^{LQD}	7.0/4.2	9.4/5.8	10.5/6.5				
F_{2n}^{LQD}	6.9/4.2	8.8/5.4	10.3/6.4				

Table 18: ATLAS discovery potential and corrected discovery potential (see text) for all SUSY scenarios investigated using each of the three networks.

6 Outlook and Conclusion

6.1 Outlook

Though some preliminary studies have been performed in the present work, many important things remain to be done in this field. From my perspective, the most important theoretical/phenomenological issues which remain are:

1. The inclusion of Baryon number violating processes in the `PYTHIA` generator. In addition, this will require a study of the exceptional colour flows that are possible when baryon number is broken. Such a study has already been carried out for the `HERWIG` generator (see [13]), but it remains to be done in `PYTHIA`.
2. The inclusion of resonant slepton and squark production in the `PYTHIA` generator. In \tilde{R} scenarios, the production of single sparticle resonances is possible and can extend the discovery potential of the LHC towards higher SUSY masses.
3. The existence of \tilde{R} couplings of comparable magnitude to the gauge couplings would have a significant effect on the renormalization group evolution of the masses and couplings from the input scale to the electroweak. At present, `PYTHIA` can be told to call on `ISASUSY` to perform this evolution, but the R -violating couplings are not yet included.

On the experimental side, several studies would be advisable:

1. The present work has only dealt with lepton number violation, the signatures of which are most likely easier to identify than baryon number violating signatures (an excess of jets). Preliminary studies indicate a lessening of the reach of the LHC in these scenarios [79]. Therefore, dedicated studies which could push this reach to the limit would be advisable. These can be performed either with the present version of the `HERWIG` generator or with the `PYTHIA` generator when \tilde{B} has been included. Since the reach is lessened, it is advisable to wait with such a study until single squark production (an enhancing mechanism) has also been included. Studying only decays is likely to give too pessimistic predictions. Again, single sparticle production *is* included in the `HERWIG` generator in its present form.
2. Having concentrated on signal isolation and discovery potential, no mass reconstruction has been undertaken in this work. Taking e.g. the events isolated by the current analysis as a basis, it would be interesting to determine how well the SUSY mass spectrum can be disentangled in the various scenarios.
3. A systematic study of the consequences of hierarchical structure in the \tilde{R} couplings. E.g. one sees that large 1st generation couplings will lead to electrons or electron-neutrinos in the final state etc. It would be of interest to study how well we can expect to “measure” the individual \tilde{R} couplings.
4. The mSUGRA points studied in this work were all based on the MSSM and as such had a neutralino LSP. As mentioned, this is not required in \tilde{R} -SUSY. It is therefore of some importance to study the effects of having non-neutralino LSP’s. A special case is if one imagines e.g. a slepton (or, less likely, a squark) LSP, for which the three-body LSP decays studied here would be replaced by two-body decays

with the associated much simpler kinematics, allowing more precise invariant mass reconstruction.

5. Re-evaluation of the trigger rates and of the trigger objects proposed here for both high and mid luminosities with better detector simulation, either a parametrization of the effects of pile-up at mid-luminosity in **AtlFast** or full detector simulation.
6. A study of to what extent the trigger menus here proposed can be combined with trigger menus for other kinds of physics.

6.2 Conclusion

In the first part of this work, it was seen that the most general space-time symmetries possible in an interacting quantum field theory includes a symmetry between bosons and fermions which is not present in the currently accepted theory, the so-called Standard Model of Particle Physics. That this extra symmetry, Supersymmetry, is not forbidden gave us our first motivation to study the physical consequences of having such a symmetry in nature. Disjoint from this, it was argued that the discovery of a fundamental Higgs boson would lead, through the hierarchy problem, to a requirement of the existence of physics not contained within the framework of the Standard Model itself. It was with the realization that Supersymmetry could cure the hierarchy problem *and* give a natural explanation for the size of the electroweak scale that we found our second, more compelling motivation. It was then noted that supersymmetry is not without defects in that it must be broken at low energies and some *additional* symmetry must exist to assure the experimentally observed high degree of proton stability.

Basically, three choices for this symmetry exist: the conservation of both lepton and baryon number or the conservation of only one of them, in the supersymmetric interactions. The former is usually cast in the shape of a conserved, multiplicative quantum number, R , and has the additional property of giving a natural dark matter candidate, since it results in the Lightest Supersymmetric Particle (the LSP) being stable. The latter two do not have this property in most of their parameter spaces. Moreover, they give rise to more free parameters and more complex phenomenologies, i.e. many additional production and decay mechanisms for the supersymmetric particles. On these grounds, supersymmetrized versions of the Standard Model are most often found with R -parity conservation being implicitly assumed.

In section 3, some effort was devoted to explain the potential fallacies and the dangers of this assumption with the conclusion that R -parity cannot assure proton stability when Supersymmetry is embedded into more fundamental frameworks containing baryon and lepton number violation exterior to Supersymmetry, as is the case, for example, in a wide range of Grand Unified Theories. The danger in focussing too much on R -parity conserving scenarios in accelerator searches becomes clear when one considers the ramifications of LSP decay on event topologies in the detector. Particularly, the reduction of the missing transverse energy signature associated with escaping LSP's in R -parity conserving scenarios could be greatly reduced if R -parity is not conserved.

1278 decay modes of Supersymmetric particles into Standard Model particles through lepton number violating couplings in the Minimal Supersymmetric Standard Model were therefore studied and implemented in the **PYTHIA** event generator. Combining this augmented version of the generator with a crude simulation of the ATLAS detector, trigger menus for mid-luminosity running of the LHC were proposed and seen to have a high

acceptance of supersymmetric events in several L -violating SuperGravity scenarios while still giving event rates in the 1Hz region.

Taking these trigger menus as basis, the possibility for a 5σ discovery after 30 fb^{-1} data taking was estimated for each investigated model, including also the R -conserving MSSM for reference. The analysis was divided into two parts, the first of which consisted of a series of cuts on kinematical and inclusive variables, placed so as to have good background rejection factors while accepting events from as many of the various SUSY models as possible (excepting the MSSM scenarios used only as reference). The second part consisted of processing the remaining events through three neural networks trained to recognize R -conserving scenarios and two different variants of lepton number violating scenarios. For cross sections down to 10^{-10} mb it was found that a 5σ discovery was possible for all scenarios with 30 fb^{-1} of data. It is not estimated that uncertainties related to QCD parameters or pile-up in the detector, both of which have not been taken into account in the present analysis, could significantly affect this conclusion.

Acknowledgements

I am deeply grateful to my two supervisors, both for their excellent guidance and for having allowed me a considerable freedom in what I have occupied myself with this last year. In many ways, the master thesis is likely to be the only chance a student gets to learn about and discuss within so few pages so many aspects of his/her field, here from quantum gravity effects on global symmetries through supersymmetric phenomenology, Monte Carlo simulations, and detector studies to brain-damaged neural networks (though of course not one of these subjects has been treated in as much detail as it might deserve). From my perspective, such freedom is a luxury, and I am very happy to have found it in carrying out this work. On the same note, I thank all the members of the HEP group at NBI for discussions, an inspiring atmosphere, and for the $n \rightarrow \infty$ CPU hours I spent on the farm. In addition, I would like to thank Dr. Alexander Khodjamirian for the depth of physical insight he gave to me before I embarked on this work. Lastly, I would like to thank Paula Eerola and the Nordic Academy for Advanced Studies for having made it possible for me to stay in Lund on a regular basis through the spring of 2001.

A Decays of SUSY particles: Conventions and References

Both SPYTHIA [80] and HERWIG [81] follow [16] (identical to [17]) for the neutralino and chargino mixing conventions whereas ISASUSY follows [82]. HERWIG uses [12] for the sfermion mixing conventions, corresponding to changing the sign of the mixing angles in [16], used in ISASUSY and SPYTHIA (as well as the work performed here). All matrix elements used in this work have been calculated in [13]. Note that it is assumed that there are no right-handed neutrinos (and thus no $\tilde{\nu}_R$ SUSY particles). The a and b couplings defined in [13] are for particles. The antiparticle couplings are obtained by $a(\tilde{c}^*) = b(\tilde{c})$. Furthermore, $a(\tilde{c})$ (and thus also $b(\tilde{c}^*)$) change sign for all couplings pertaining to the neutralino χ if the diagonalization of the neutralino mass matrix results in a negative eigenvalue for the χ mass (this sign change is the effect of changing the physical field to $\gamma_5\chi$, thus obtaining a field with positive mass, but with slightly different couplings). With respect to the signs of mixing matrix elements and a and b couplings, one should not be distressed by noticing a number of sign differences between SPYTHIA and HERWIG for the neutralino mixing. These are artifacts of the diagonalization procedure, and as such of no physical importance. If they exist, they are always such that all mixing matrix elements pertaining to e.g. $\tilde{\chi}_1^0$ have their sign flipped, both in N_{ij} and N'_{ij} (defined in section 2.2.1). Since the decay rates of neutralino i depend only on products of mixing matrix elements like $N_{ij}N'_{ik}$ (see [13]), the overall signs of the rows in N and N' have no importance.

With respect to the scalar mixing, there is indeed a convention difference, as mentioned above. HERWIG uses [12] while SPYTHIA uses [16]. The difference is in the sign of the mixing angle, but the mixing elements themselves should still be the same. One can quickly see this by taking a look at the mixing matrices as expressed in the two conventions with their two different choice for the sign of the mixing angle:

$$\begin{pmatrix} \tilde{s}_L \\ \tilde{s}_R \end{pmatrix} = \begin{pmatrix} \cos \theta_+ & \sin \theta_+ \\ -\sin \theta_+ & \cos \theta_+ \end{pmatrix} \begin{pmatrix} \tilde{s}_1 \\ \tilde{s}_2 \end{pmatrix} \quad \begin{pmatrix} \tilde{s}_L \\ \tilde{s}_R \end{pmatrix} = \begin{pmatrix} \cos \theta_- & -\sin \theta_- \\ \sin \theta_- & \cos \theta_- \end{pmatrix} \begin{pmatrix} \tilde{s}_1 \\ \tilde{s}_2 \end{pmatrix} \quad (58)$$

in the conventions of [12] and [16], respectively, and noting that $\theta_+ = -\theta_-$.

B Phase Space Integrations in Dalitz Variables

The kinematics of an unpolarized three-body decay $0 \rightarrow 1, 2, 3$ can be parametrized in terms of the Dalitz variables:

$$m_{12}^2 \equiv (p_1 + p_2)^2 \quad m_{23}^2 \equiv (p_2 + p_3)^2 \quad m_{13}^2 \equiv (p_1 + p_3)^2 \quad (59)$$

$$M_0^2 = m_{12}^2 + m_{23}^2 + m_{13}^2 - m_1^2 - m_2^2 - m_3^2 \quad (60)$$

Since $|\overline{M}|^2$ can contain resonances in any of these variables, we wish to study how we can parametrize the phase space in terms of *any* combination of two of these, enabling an optimization of numerical integration procedures.

Changing variables inside $|\overline{M}|^2$ is an easily accomplished task. If one desires to chose e.g. m_{12}^2 and m_{23}^2 to parametrize the degrees of freedom, one simply uses eq. (60) to interpret any dependence of $|\overline{M}|^2$ on m_{13}^2 as a dependence on m_{12}^2 and m_{23}^2 . The integration must then be performed over phase space parametrized in terms of the two chosen variables. The limits for this integration can be derived as follows:

In all generality, we know that

$$m_{ab}^2 = (p_a + p_b)^2 = m_a^2 + m_b^2 + 2E_a E_b - 2\vec{p}_a \cdot \vec{p}_b = (E_a + E_b)^2 - (\vec{p}_a + \vec{p}_b)^2 \quad (61)$$

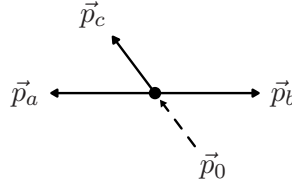
$$= (p_0 - p_c)^2 = M_0^2 + m_c^2 - 2E_0 E_c + 2\vec{p}_0 \cdot \vec{p}_c = (E_0 - E_c)^2 - (\vec{p}_0 - \vec{p}_c)^2 \quad (62)$$

As the Dalitz variables are Lorentz invariant, we can chose any frame to evaluate them in. Going to the CM of a and b , we find that the minimum value of m_{ab}^2 must occur when the two particles are lying completely still. On the other hand, the maximum value must occur when particle c is lying completely still. In this case, the CM of a and b is also the CM of the decaying particle, and so the decaying particle is also lying completely still. Using eqs. (61) and (62) we then have:

$$m_{ab,\min}^2 = (m_a + m_b)^2 \quad m_{ab,\max}^2 = (M_0 - m_c)^2 \quad (63)$$

These are the limits for the ‘outside’ integration.

For the ‘inside’ integration, the limits follow almost as easily. m_{ab}^2 should now be thought of as having some specific value. Again going to the rest frame of a and b , we have the following picture:



Taking a look at eq. (61), we see that that m_{ac}^2 (m_{bc}^2) attains its minimum when c goes parallel to a (parallel to b), and its maximum when c goes antiparallel to a (b). Thus, using $*$ to denote that we are to evaluate energies and momenta in the CM of a and b , we have:

$$m_{(a,b)c}^2 = (E_{a,b}^* + E_c^*)^2 - (\vec{p}_{a,b}^* + \vec{p}_c^*)^2 = (E_{a,b}^* + E_c^*)^2 - (|\vec{p}_{a,b}^*|^2 + |\vec{p}_c^*|^2 + 2|\vec{p}_{a,b}^*||\vec{p}_c^*|\cos\theta) \quad (64)$$

$$\begin{aligned} \Rightarrow m_{(a,b)c,\min}^2 &= (E_{a,b}^* + E_c^*)^2 - \left(\sqrt{E_{a,b}^{*2} - m_{a,b}^2} + \sqrt{E_c^{*2} - m_c^2} \right)^2 \\ m_{(a,b)c,\max}^2 &= (E_{a,b}^* + E_c^*)^2 - \left(\sqrt{E_{a,b}^{*2} - m_{a,b}^2} - \sqrt{E_c^{*2} - m_c^2} \right)^2 \end{aligned} \quad (65)$$

with the CM energies [29, chp.34]:

$$E_{a,b}^* = \frac{m_{ab}^2 - m_{b,a}^2 + m_{a,b}^2}{2m_{ab}} \quad E_c^* = \frac{M_0^2 - m_{ab}^2 - m_c^2}{2m_{ab}} \quad (66)$$

B.1 Numerical Integration Procedure for Virtual Contributions

Now that the most advantageous integration variables can be chosen without problems, we need to select the most advantageous integration technique. In general, the integrations could contain fairly narrow peaks (resonances), and so a simple step-by-step integration would be either too coarse or too time-consuming. A good solution in many cases is to resort to an optimized Monte Carlo technique, but when the number of dimensions is small (in our case $d = 1-2$), a better idea is to use a transformation of integration variables that results in approximately flat integrands (this is usually referred to as variance reduction)

which can then be integrated using a simple stepping algorithm on a uniform lattice. This optimizes both CPU time and accuracy simultaneously.

For the case at hand, however, note that the resonances *will never* lie inside the integration limits. If they did, it would mean that the process could happen with the intermediate particle on shell, and so we could really speak of the process as being composed of two distinct parts, namely 1) the (R conserving) decay of a neutralino/chargino to an on-shell sfermion and an SM fermion, and 2) the (R violating) decay of the sfermion to two SM fermions. The branching ratio for the first process is already calculated by the SPYTHIA code, and the branching ratio for the second is calculated by the sfermion part of the R -violation code. Thus we would be doing double counting if we added such a contribution again. The only contributions not already handled by other parts of the code are the off-shell contributions where the intermediate sfermion is truly virtual and therefore outside the kinematical limits for the integrations we will perform.

It is therefore exceedingly important to note that the R -Violating 3-body widths and branching ratios for the neutralinos and charginos as output by PYTHIA only contain the off-shell contributions! For the complete exclusive branching ratios, the on-shell contributions should be computed and added separately.

Since the integrands for virtual contributions can be expected to be reasonably flat, the integrations can be handled using standard gaussian quadrature without problems. With respect to interference terms, these are neglected if either of the interfering diagrams have an on-shell propagator, since they are then suppressed by $(\Gamma_{\text{res}}/M_{\text{res}})^2$.

B.2 Numerical Integration Procedure for Total Exclusive Contributions

Above, we have only given justification for why the integrands in this specific implementation can be expected to be smooth and thus integrable by standard methods. In addition, we shall now give a method to calculate the full, exclusive width (i.e. including both off-shell and on-shell intermediate states) where gaussian quadrature would be a hazardous enterprise since it cannot be relied upon to catch sharp peaks in the integrand. Rather, we should make use of our knowledge of the shape of the resonances to integrate efficiently those contributions that are peaked and reserve gaussian quadrature for the “flat” contributions.

In all generality, we know that the matrix elements are expressible as sums of terms of which the most complicated are the interferences between different diagrams with different resonances in different Dalitz variables. As mentioned in section 3.3.3, the interference terms can be expected to be relatively small and do not exhibit sharp peaks. We then concentrate on the pure resonance terms. A rough idea of the shape of these terms is given by (with x denoting the resonant Dalitz variable squared):

$$R(x) + C(x) \tag{67}$$

where C is a slowly varying function, and R is the Breit-Wigner resonance function:

$$R(x, M, \Gamma) = \frac{1}{(x - M^2)^2 + M^2\Gamma^2} \tag{68}$$

with M being the mass of the resonance and Γ its decay width. Since we shall only need a rough approximation, let C be approximated by a constant. For a specific resonance term

characterized by the resonance mass, M_{res} , and the width Γ_{res} , the Phase Space integral then becomes:

$$\begin{aligned} \int_{x_{min}}^{x_{max}} \int_{y_{min}}^{y_{max}} [R(x) + C] dy dx &= \Delta y \int_{x_{min}}^{x_{max}} \frac{1}{(x - M_{res}^2)^2 + \Gamma_{res}^2 M_{res}^2} dx + C \Delta x \Delta y \\ &= \frac{1}{\Gamma_{res} M_{res}} \left[\arctan \left(\frac{x_{max} - M_{res}^2}{\Gamma_{res} M_{res}} \right) - \arctan \left(\frac{x_{min} - M_{res}^2}{\Gamma_{res} M_{res}} \right) \right] + C \Delta x \Delta y \end{aligned} \quad (69)$$

We now introduce the following functions, normalized to integrate to unity, which will represent the slowly varying and resonant contributions, respectively:

$$f_1(x) \equiv \frac{1}{\Delta x} \quad , \quad f_2(x) \equiv \frac{R_1(x)}{\int R_1(x) dx} \quad (70)$$

$$f(x) \equiv f_1(x) + f_2(x) \quad (71)$$

with the primitive functions:

$$F_{1,2}(x) = \int_{x_{min}}^x f_{1,2}(x) dx \quad \implies \quad dF_{1,2}(x) = f_{1,2}(x) dx \quad (72)$$

From the normalization of the f_i , it is clear that $F_i(x_{min})$ and $F_i(x_{max}) = 1$. The usefulness of these definitions becomes clear when we rewrite the original integral (using $|\overline{T}|^2$ to denote a resonant term in $|\overline{M}|^2$ and assuming that $f(x)$ is positive definite):

$$\int_{x_{min}}^{x_{max}} \int_{y_{min}}^{y_{max}} |\overline{T}(x, y)|^2 dy dx = \int_{x_{min}}^{x_{max}} \int_{y_{min}}^{y_{max}} \frac{|\overline{T}(x, y)|^2}{f(x)} (f_1(x) + f_2(x)) dy dx \quad (73)$$

The quantity $|\overline{T}|^2/f(x)$ must be reasonably flat. If, for some x , there is suddenly a large deviation from flatness in $|\overline{T}|^2$, this must be due to the resonance, and so $f(x)$ will also deviate from flatness there, making the quotient of the two approximately flat over the entire integration region. We can get rid of the factor multiplying the quotient by changing integration variables using the primitive functions:

$$\int_{x_{min}}^{x_{max}} \int_{y_{min}}^{y_{max}} |\overline{T}(x, y)|^2 dy dx = \int_0^1 \int_{y_{min}}^{y_{max}} \frac{|\overline{T}(x, y)|^2}{f(x)} dy dF_1(x) + \int_0^1 \int_{y_{min}}^{y_{max}} \frac{|\overline{T}(x, y)|^2}{f(x)} dy dF_2(x) \quad (74)$$

Furthermore, the resonance terms in the matrix elements considered in this work (see appendix A) only depend on the resonant variable, here denoted x , so $|\overline{T}(x, y)|^2 = |\overline{T}(x)|^2$. The integral over dy then simply becomes Δy , and there is now no problem in discretizing eq. (74) using a simple grid lattice in F_i (i.e. with constant grid spacing). The definitions of the primitive functions can then be inverted to yield x as a function of F_i . Using an $N \times N$ lattice, one obtains:

$$\Delta y \int_0^1 \frac{|\overline{T}(x)|^2}{f(x)} dF_{1,2}(x) \quad \rightarrow \quad \frac{\Delta y}{N} \sum_{i=1}^N \frac{|\overline{T}(x_i)|^2}{\frac{1}{\Delta x} + \frac{R(x_i)}{\int R dx}} \quad (75)$$

It is clear that a uniform stepping in the F_1 variable corresponds directly to a uniform stepping in x :

$$F_1(x) = \frac{1}{\Delta x} \int_{x_{min}}^x dx \quad \implies \quad x = x_{min} + F_1 \Delta x \quad (76)$$

so that a stepping of F_1 between 0 and 1 will produce a uniform distribution of x values between x_{min} and x_{max} . For the second integral in eq. (74), the expressions become a bit more involved. Translating the simple F_2 grid to x values involves the inversion of a complicated function:

$$F_2(x) = \int_{x_{min}}^x \frac{R(x)}{\int R(x) dx} dx = \frac{\arctan\left(\frac{x - M_{res}^2}{\Gamma_{res} M_{res}}\right) - \arctan\left(\frac{x_{min} - M_{res}^2}{\Gamma_{res} M_{res}}\right)}{\arctan\left(\frac{x_{max} - M_{res}^2}{\Gamma_{res} M_{res}}\right) - \arctan\left(\frac{x_{min} - M_{res}^2}{\Gamma_{res} M_{res}}\right)} \quad (77)$$

Isolating x in this equation (using `Mathematica`) yields

$$x = M_{res}^2 + \Gamma_{res} M_{res} \tan \left[F_2 \arctan \left(\frac{x_{max} - M_{res}^2}{\Gamma_{res} M_{res}} \right) - (F_2 - 1) \arctan \left(\frac{x_{min} - M_{res}^2}{\Gamma_{res} M_{res}} \right) \right] \quad (78)$$

This is not as bad as it looks. Most of the involved quantities need to be evaluated only once, since only F_2 changes. A quick check is furnished by letting F_2 be zero in which case it is obvious from the above formula that x becomes simply x_{min} (only the +1 of the last term in (78) contributes, and $\tan(\arctan(f(x))) = f(x)$). For $F_2 = 1$, it is also quick to verify that $x = x_{max}$. We have thus arrived at a complete prescription for how to press the resonances flat, obtaining the sum of a uniform and a non-uniform grid in x instead.

C \not{L} -SUSY in PYTHIA. User's Reference.

C.1 Switches & Parameters set by the user in the PYTHIA calling program

- IMSS(51): λ couplings. Default is off (=0).
 - (=0): λ couplings off.
 - (=1): All allowed couplings set to fixed value given by $10^{\text{RMSS}(51)}$. Default value for RMSS(51) is 0.
 - (=2): Couplings set to “natural values”, $\lambda_{ijk} \propto \sqrt{m_i m_j m_k / (126 \text{ GeV})^3}$, as defined in [35, eq. (17)], giving a hierarchical structure in generations. RMSS(51) is here used to give the constant of proportionality. If the user does not have other specific wishes, its value should be set to 1 when using this scenario.
 - (=3): The program initializes with default values ($\lambda_{ijk} = 0$), but expects the user to enter all non-zero couplings by hand into the RVLAM(I,J,K) array in the calling program.
- IMSS(52): λ' couplings. Default is off (=0).
 - (=0): λ' couplings off.
 - (=1): All couplings set to fixed value given by $10^{\text{RMSS}(52)}$. Default value for RMSS(52) is 0.

- (=2): Couplings set to “natural values”, $\lambda'_{ijk} \propto \sqrt{m_i m_j m_k / (126 \text{ GeV})^3}$, as defined in [35], with the constant of proportionality given by RMSS(52). If the user does not have other specific wishes, its value should be set to 1 when using this scenario.
- (=3): The program initializes with default values ($\lambda'_{ijk} = 0$), but expects the user to enter all non-zero couplings by hand into the RVLAMP(I,J,K) array in the calling program.
- (IMSS(53)): Should be reserved for λ'' couplings on/off together with RMSS(53).
- PYMSRV : This is the commonblock in PYTHIA where the L -violating couplings reside; the λ_{ijk} couplings are stored in RVLAM(i,j,k), and the λ'_{ijk} in RVLAMP(i,j,k). Space has been reserved for an eventual future study of B -violation in the RVLAMB(i,j,k) array which is intended to store the λ''_{ijk} couplings.

C.2 Subroutines and functions handling R -violation inside PYTHIA

- PYRVST : Subroutine to print information about semi-inclusive branching ratios and coupling values. Called from PYSTAT if R-Violation has been turned on (IMSS(51)=1 or IMSS(52)=1).
- PYRVSF : Subroutine to calculate \not{R} decay widths of sfermions based on the selected SUSY scenario and coupling values. If there is no phase space available for a given mode, the width for that mode is set to zero and PYTHIA is told to ignore the mode completely.
- PYRVN : Same as above for \not{R} decays of neutralinos.
- PYRVCH : Same as above for \not{R} decays of charginos.
- PYRVSB : Calculates sfermion two-body widths.
- PYRVGW : Routine for calculating three-body decay widths of neutralinos and charginos.
- PYRVI1, PYRVI2, PYRVI3 : Functions to integrate resonant terms, L-R interference terms, and true interference terms, respectively over phase space.
- PYRVG1, PYRVG2, PYRVG3, PYRVG4 : Integrands for the phase space integrations.

In addition, a consistency check has been added to the routine which diagonalizes the neutralino mass matrix (PYEIG4) so that error messages will be printed if the off-diagonal elements of the diagonalized matrix (recomputed from the original matrix and the diagonalizing matrix given by the routine) are larger than 10^{-6} or if the diagonal elements calculated by brute force deviate by more than 10^{-6} from the values in the mass vector given by the routine. This does not encumber the performance of PYTHIA in any way, since the matrix needs to be diagonalized only once for each run.

C.2.1 Warnings and error messages:

- **PYRVGW ERROR: Negative Width in $\tilde{a} \rightarrow b\ c\ d$.** This error, if encountered, is not as serious as one should think. Even though resonant diagrams are not included in the calculations, neither are the interferences between resonant and non-resonant diagrams (which are proportional to $\Gamma_{\text{res}}^2/M_{\text{res}}^2$ and so negligible for narrow resonances). This means that the calculation should still be positive definite, and so a negative width can only occur as a result of numerical error. Such errors are most likely to occur in the presence of strong threshold effects where the diagram values are small (due to limited phase space) and can be greatly differing, quickly building up a sizeable numerical error. Since the decay rate in these cases is at any rate very small (compared to rates for modes with bigger phase spaces), the program just keeps running, setting the offending width to zero. One may want to check, however, that the process concerned really does lie near the edge of its phase space.

C.3 Resonant decay treatment

Each time a physical particle is generated in PYTHIA, a random mass is calculated, distributed according to the Lorentz profile for that particle. As decay widths and therefore branching fractions depend on the mass of the incoming particle¹², the most detailed method for determining in which channel the particle will decay is to calculate its widths to all available channels at that mass and from them determine the branching fractions. This is feasible for low-mass particles with few and/or simple decay channels, and so every time a W boson, for example, decays in PYTHIA, its branching fractions are evaluated at the specific mass of that W . For supersymmetric particles with hundreds of decay channels and many adjustable SUSY parameters entering the calculations, this method would be very time consuming with *all* decay widths having to be recalculated each time a particle is generated. Instead, an approximate method is used. All branching fractions are evaluated once and for all at the resonance mass during each program execution. This saves CPU time, yet it has the potential danger that some of the sparticles produced in the generator have masses that could be lower than some threshold where some channel reaches zero phase space. Allowing such a sparticle to decay into that channel would result in violation of energy conservation. The way that PYTHIA is told to handle this in the present case is to go away from the full Lorentz profile when generating masses, using instead a limited range (symmetrically, so as not to skew the center point) where the lower bound is the kinematical threshold causing the trouble.

¹²This becomes especially important when some of the channels contain particles with masses close to the decaying particle's mass. In that case, there will be a threshold where only particles above the threshold mass can decay via that channel.

D Trigger Shapes

D.1 Background Rates

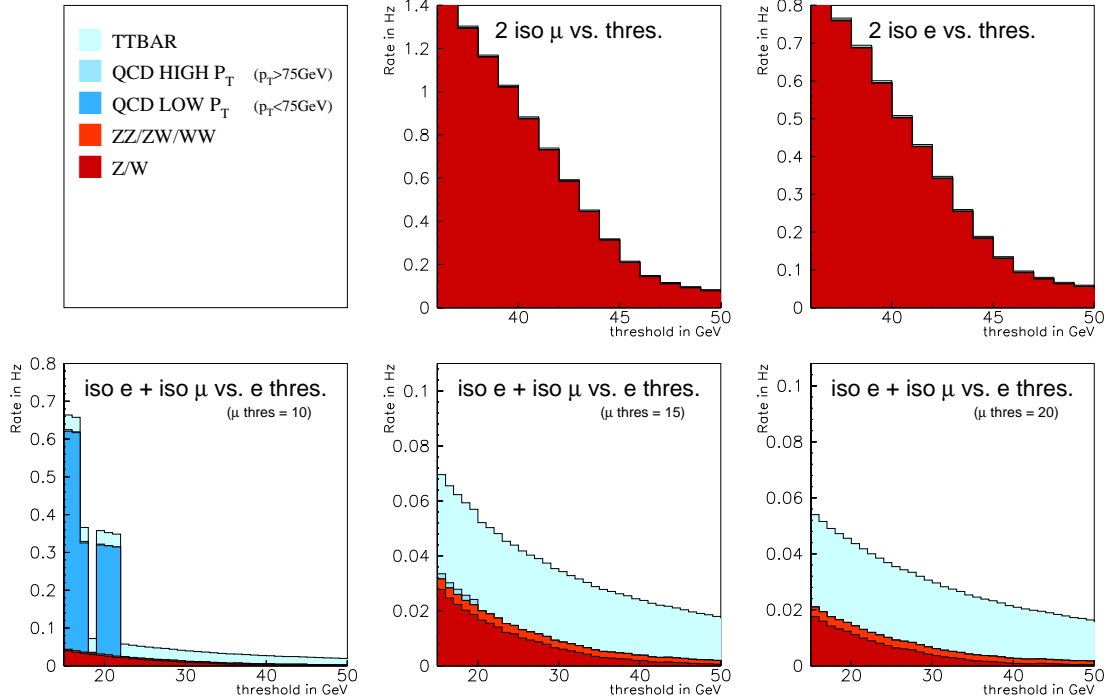
A comprehensive collection of trigger rates as functions of thresholds is here given. Note that the vertical scale is not the same in the plots. It is implicitly understood that all threshold values are on p_T in GeV. With respect to the normalizations of these plots, one should allow for significant uncertainties since we are extrapolating already uncertain parton distributions (GRV 94L) over orders of magnitude in energy. Caution in too strong interpretations of these figures should also be exercised since the impact of the PDF uncertainties on the *shape* of the distributions can be non-trivial.

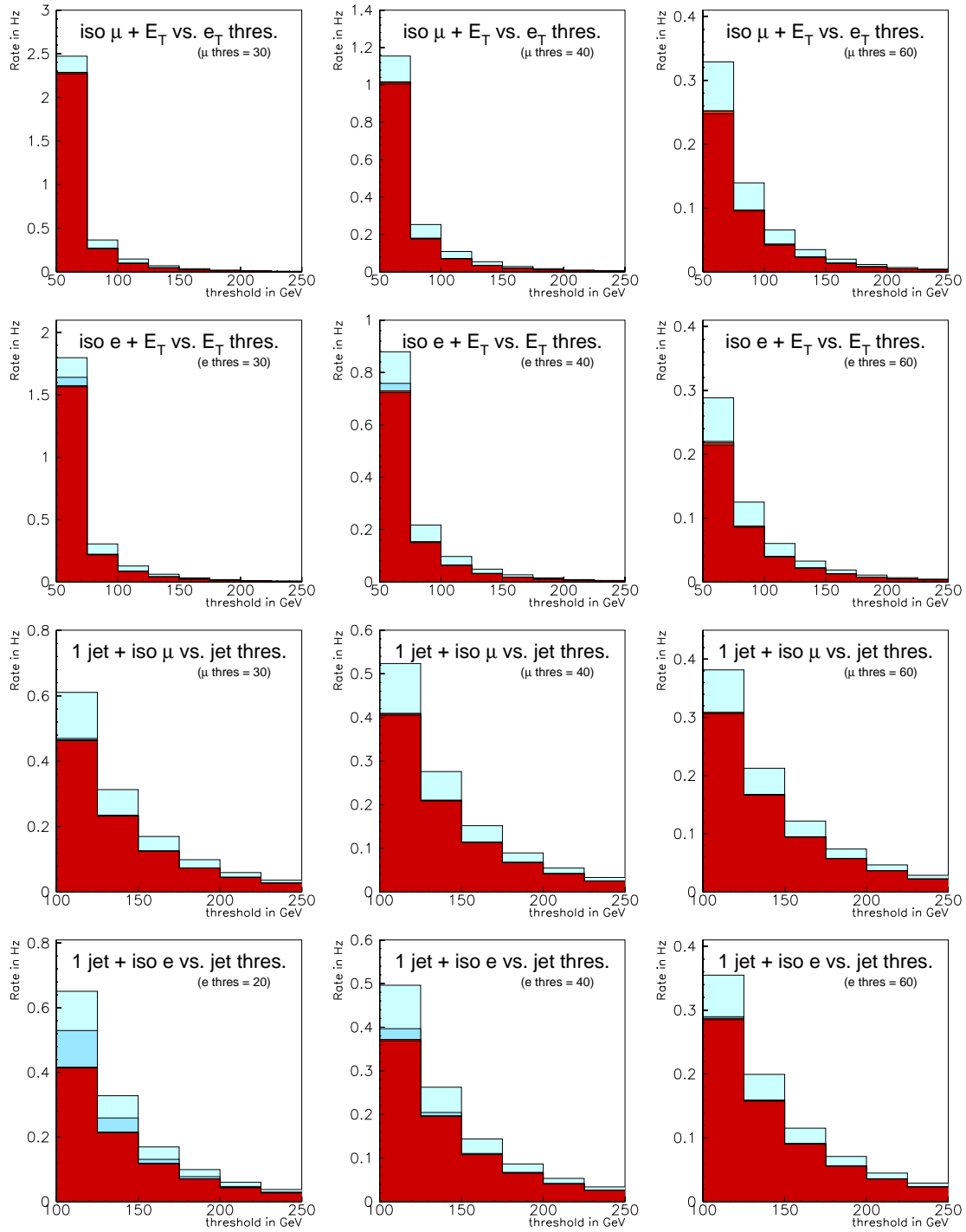
Plots show the total background rates passing the trigger p_T thresholds as functions of the thresholds. For the two-muon and two-electron trigger, *both* of the muons/electrons are required to be above threshold. Since the number of events passing a threshold should obviously be a monotonically decreasing function of the threshold value, all plots shown should be strictly decreasing functions of the thresholds. In some of the plots, there is some “noise” or “jitter” superimposed on this decreasing behaviour, due to the way muon and electron reconstruction efficiencies were taken into account in the analysis. For each event for each trigger threshold a random number was compared to the trigger efficiency for each lepton candidate. This creates a natural “jitter” since more events could be thrown away for one threshold than another if generated event numbers are low, as happens on the tails of the p_T distributions. This problem is especially significant for the low- p_T QCD $2 \rightarrow 2$ processes where rates are extremely high and the number of events in the p_T -tails surviving cuts are extremely low. Even though comparably large event samples, $\mathcal{O}(10^8)$ events, have been generated for the lowest p_T processes, still only two make it to the e+mu10I trigger (see below), creating sudden drops in the trigger rate at the p_T ’s of the electrons in those events. With larger samples, these problems could be avoided, yet considering the uncertainties already associated with QCD processes in the extreme parts of the p_T spectrum, it has not been deemed worth the (significant) extra computer resources and time required to do so here. The overall numbers of generated events used in the trigger analysis are given in table 19.

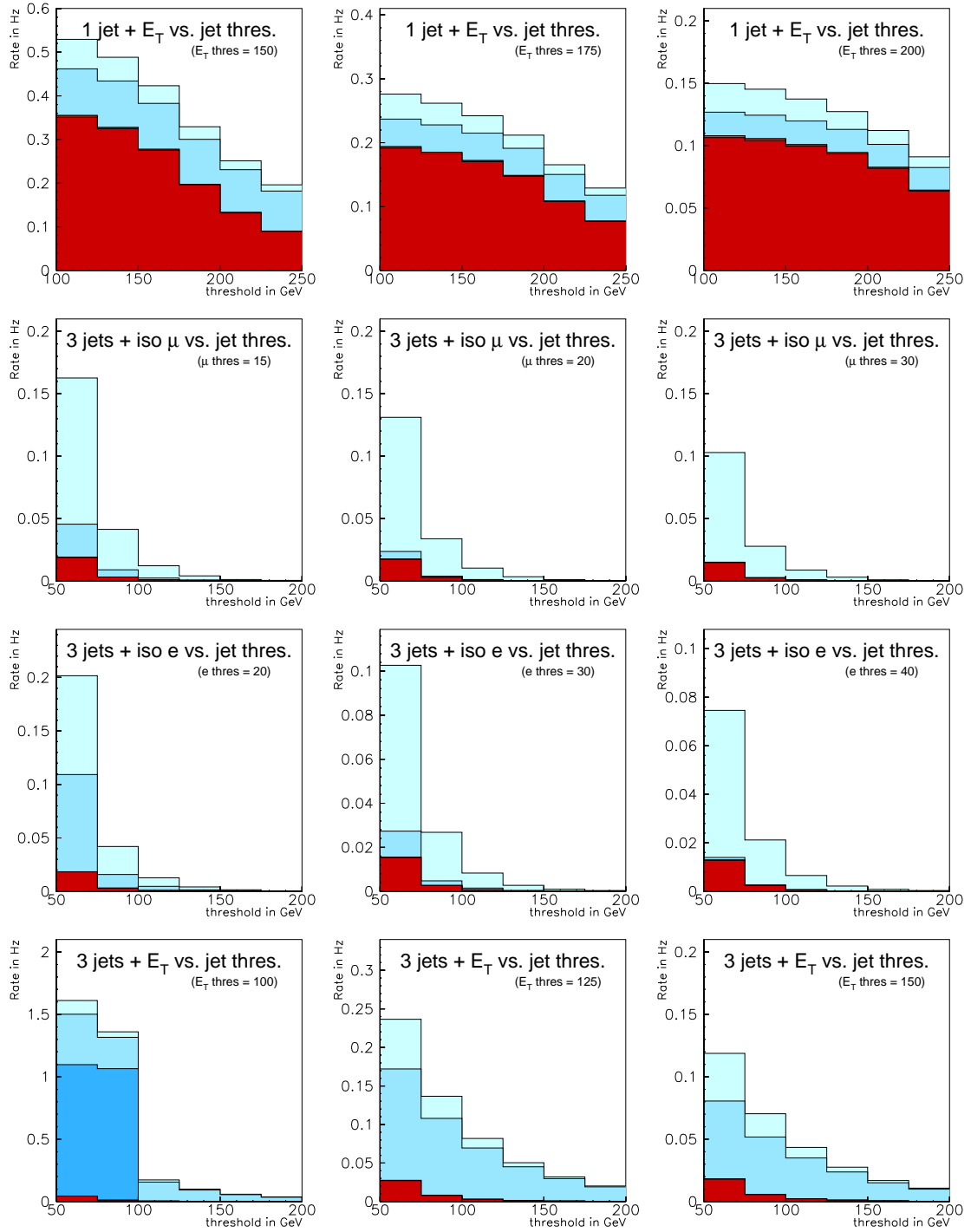
Process	QCD $2 \rightarrow 2$	QCD $2 \rightarrow 2$	QCD $2 \rightarrow 2$	QCD $2 \rightarrow 2$
	$p_T = 1 - 10 \text{ GeV}$	$p_T = 10 - 75 \text{ GeV}$	$p_T = 75 - 150 \text{ GeV}$	$p_T > 150 \text{ GeV}$
σ	55 mb	12 mb	$5.5 \times 10^{-3} \text{ mb}$	$2.9 \times 10^{-4} \text{ mb}$
Rate [s^{-1}]	1.6×10^8	3.7×10^7	1.7×10^4	8.7×10^2
N_{gen}	2.5×10^8	2.2×10^8	1.4×10^7	1.1×10^7

Process	$t\bar{t}$	Z/W	$ZZ/ZW/WW$
σ	$6.2 \times 10^{-7} \text{ mb}$	$1.2 \times 10^{-3} \text{ mb}$	$1.2 \times 10^{-7} \text{ mb}$
Rate [s^{-1}]	1.9	3.6×10^3	0.36
N_{gen}	5.9×10^6	1.8×10^8	5.9×10^6

Table 19: Numbers of generated events for the trigger study. The rates listed are total rates before trigger for $L = 3 \times 10^{33} \text{ cm}^{-2} \text{ s}^{-1}$. To avoid unnecessarily messy plots, the two lowest p_T QCD $2 \rightarrow 2$ samples have been combined and are shown in the same colour below, as are the two highest p_T samples.

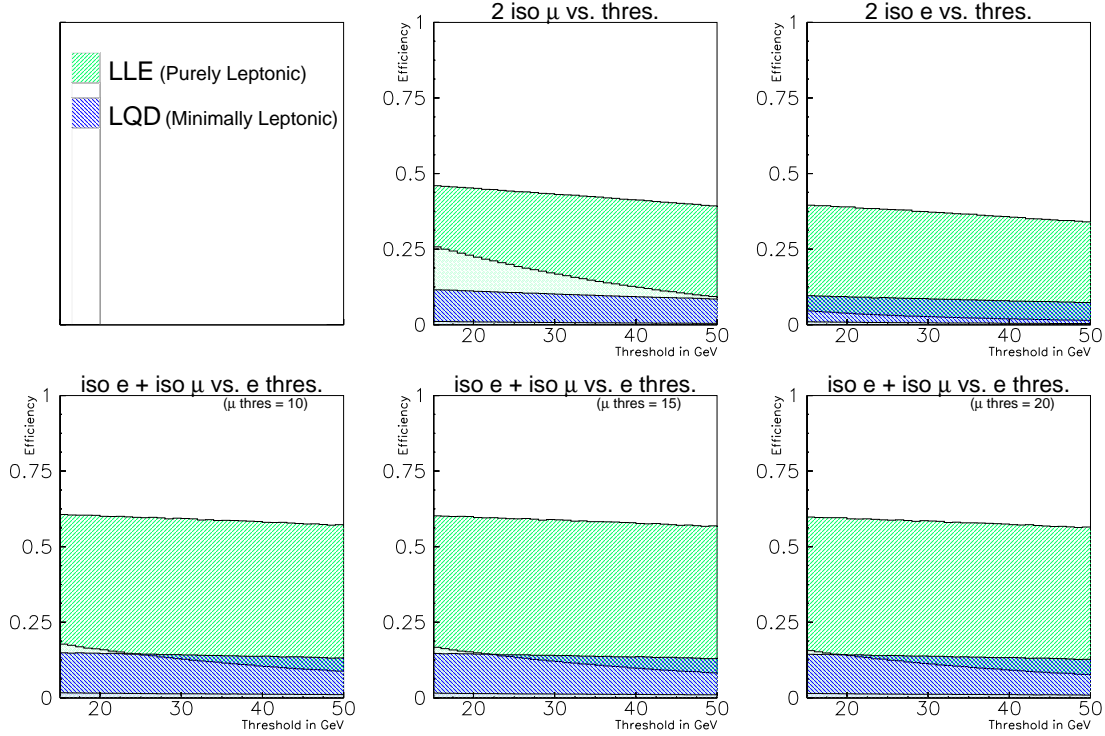


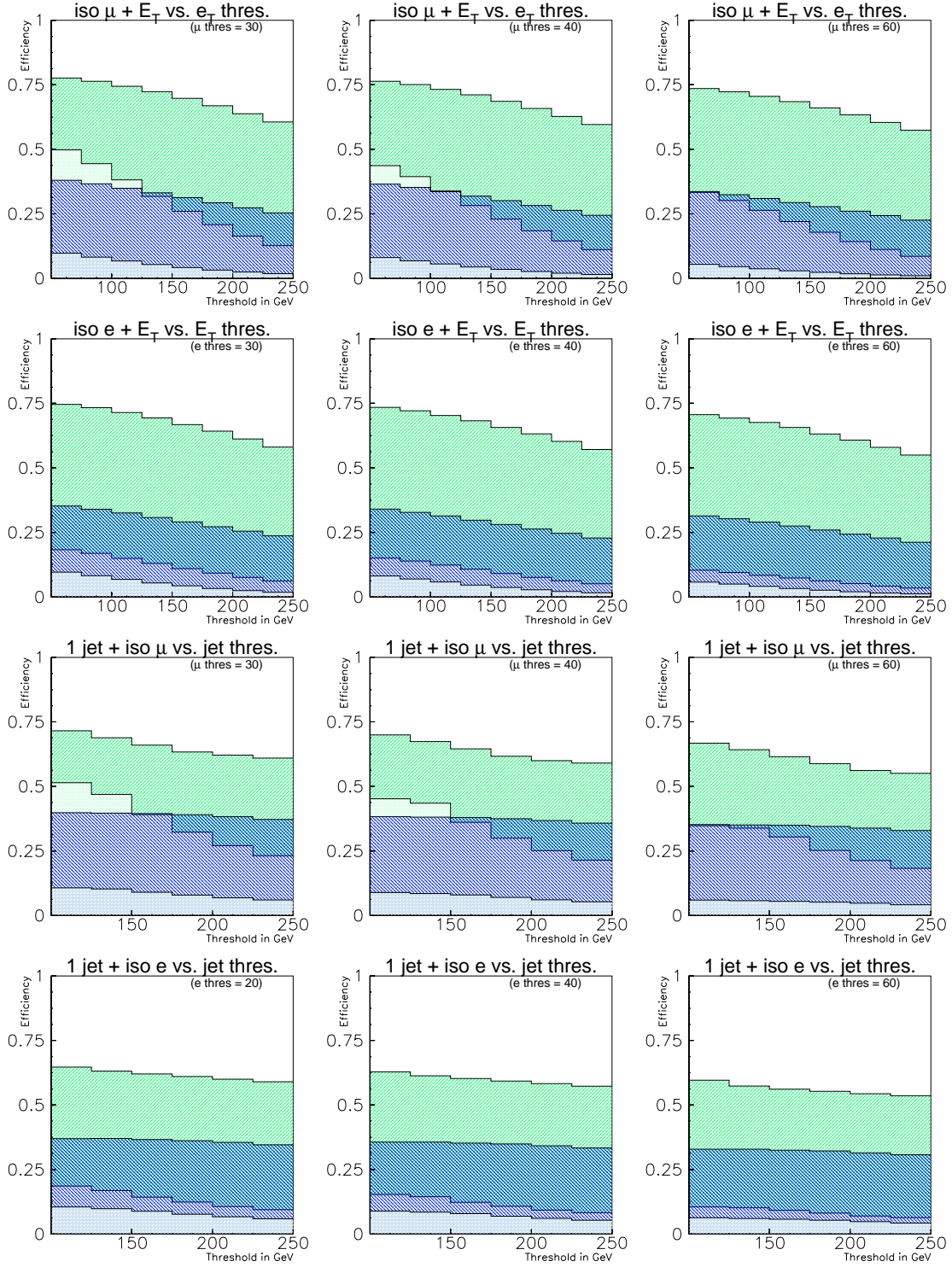


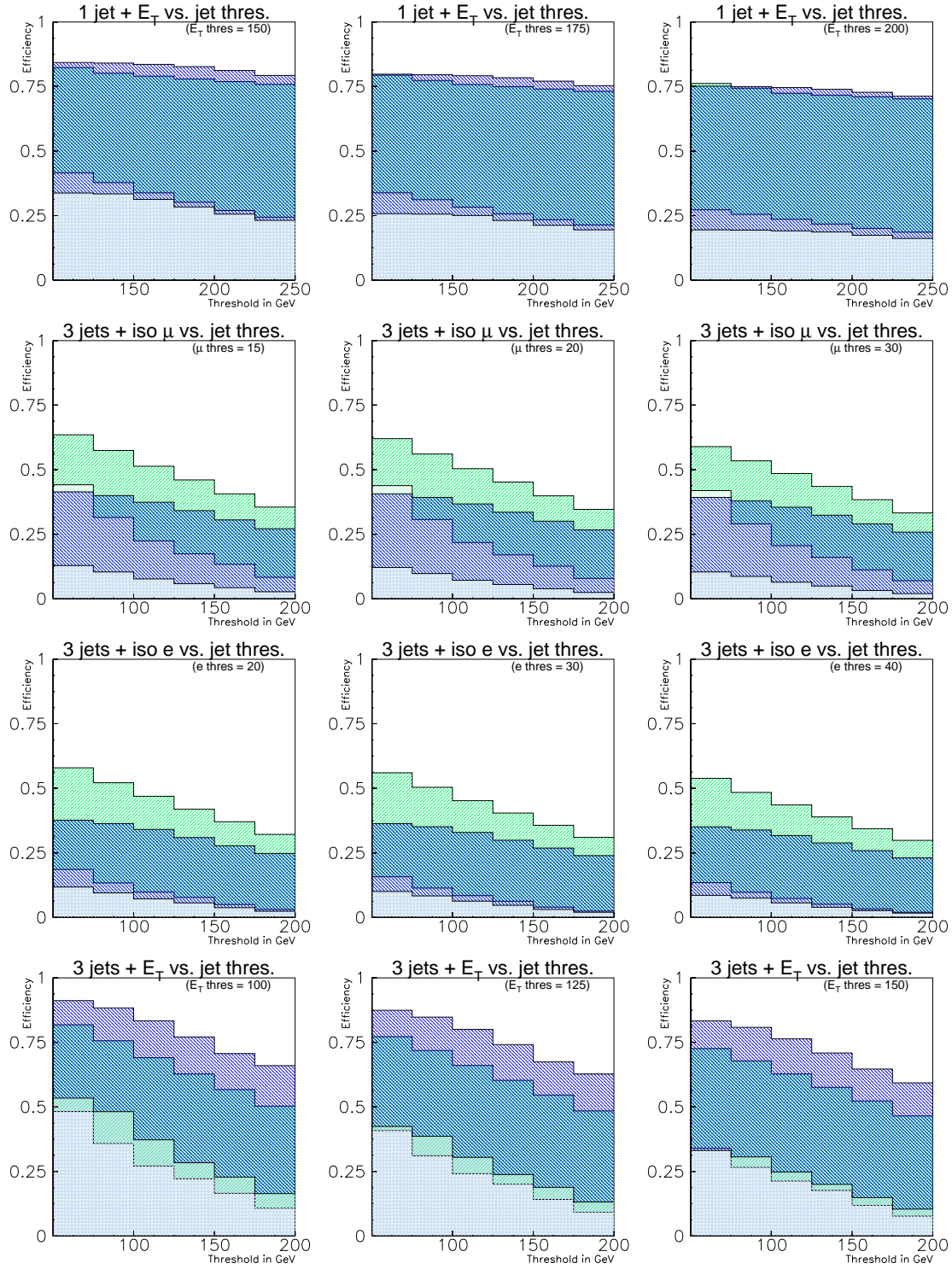


D.2 Signal Efficiencies

The following plots attempt to combine a large amount of information in as small a space as possible. For each of the two \cancel{E}_T terms in the superpotential, LLE and LQD, a scan has been made over all five mSUGRA points and over the three different possibilities for the individual coupling strengths investigated. The range of efficiencies (min to max found in the scan over mSUGRA and coupling scenarios) for the scenarios with non-zero LLE couplings is shown in green and the efficiencies for LQD in blue. In order not to over-clutter the plots, the LLE+LQD scenarios studied are not shown. Their efficiencies all lie within the boundaries set by the two “pure” scenario types. As one would expect, the LLE scenarios do well in the leptonic triggers while the LQD terms do not fare quite as well as one could have hoped in the jet triggers. This is simply due to the fact that the lightest neutralino has a tendency to decay into $q\bar{q}\nu$ in these scenarios, caught mainly by the jets + \cancel{E}_T triggers which must necessarily have high thresholds due to the large background rates. In the generation of each plot, 10^5 events were generated per scenario. Since more than 1000 events pass the triggers in all cases, we do not see the same jitter caused by the electron and muon reconstruction efficiencies as in the previous plots. The total efficiency is, of course, a complicated function of each of these triggers. These plots are merely presented to give the reader some feeling for how useful each trigger item is by itself and as a potential starting point for future studies.







References

- [1] ATLAS Collaboration. ATLAS: Detector and Physics Performance Technical Design Report. Technical report, CERN, 1999. CERN/LHCC 99-14.
- [2] S. Coleman and J. Mandula. All possible symmetries of the S matrix. *Phys. Rev.*, 159:1251, 1967.
- [3] R. Haag, J. T. Lopuszanski, and M. Sohnius. All possible generators of supersymmetries of the S matrix. *Nucl. Phys.*, B(88):257, 1975.
- [4] G. L. Kane, editor. *Perspectives on Supersymmetry*. World Scientific, 1998.
- [5] J. D. Lykken. Introduction to supersymmetry. In *Talk given at TASI 96: Fields, Strings, and Duality*, June 1996. hep-th/9612114.
- [6] K. Cahill. Elements of supersymmetry, Chp. 14. hep-ph/9907295, 1999.
- [7] C. S. Wu et al. Experimental test of parity conservation in beta decay. *Phys. Rev.*, 105:1413, 1957.
- [8] S. P. Martin. A supersymmetry primer. In G. Kane, editor, *Perspectives on supersymmetry*, chapter 1. World Scientific, 1998.
- [9] S. Weinberg. Supersymmetry at ordinary energies. Masses and conservation laws. *Phys. Rev.*, D(26):287, 1982.
- [10] S. Dimopoulos and H. Georgi. Softly broken supersymmetry and SU(5). *Nucl. Phys.*, B(193):150, 1981.
- [11] A. J. Buras and R. Fleischer. Quark mixing, CP violation and rare decays after the top quark discovery. In A. J. Buras and M. Linder, editors, *Heavy Flavours II*. World Scientific, 1996. hep-ph/9704376.
- [12] H. Baer, J. Sender, and X. Tata. The search for top squarks at the fermilab tevatron collider. *Phys. Rev.*, D(50):4517, 1994. hep-ph/9404342.
- [13] H. Dreiner and M. H. Seymour. Parton shower simulations of R-parity violating supersymmetric models. *JHEP*, April 2000. hep-ph/9912407.
- [14] E. K. Akhmedov. Neutrino physics. In *Lectures given at ICTP Summer School in Particle Physics 1999*, 1999. hep-ph/0001264.
- [15] E. A. Baltz and P. Gondolo. Neutralino decay rates with explicit R parity violation. *Phys. Rev.*, D(57):31, 1998. hep-ph/9709445.
- [16] H. E. Haber and G. L. Kane. The search for supersymmetry: Probing physics beyond the Standard Model. *Phys. Rep.*, 117:76–263, 1985. Mixing conventions can be found in App. C.
- [17] J. F. Gunion and H. E. Haber. Higgs bosons in Supersymmetric models - I. *Nucl. Phys.*, B(272):1, 1986. SLAC-PUB-3404.
- [18] L. B. Okun. *Leptons and Quarks*, chapter 24. Elsevier Science, 1st edition, 1984. Third impression (1999).

- [19] J. Ellis. The 115 GeV Higgs Odyssey. hep-ex/0011086, 2000.
- [20] E. Witten. Dynamical breaking of supersymmetry. *Nucl. Phys.*, B(188):513, 1981.
- [21] L. E. Ibáñez and G. G. Ross. $SU(2)_L \times U(1)$ symmetry breaking as a radiative effect of supersymmetry breaking in GUTs. *Phys. Lett.*, B(110):215, 1982.
- [22] M. Drees and S. P. Martin. Implications of SUSY model building. In T. L. Barklow et al., editors, *Electroweak symmetry breaking and new physics at the TeV scale*, pages 146–215, 1995. hep-ph/9504324.
- [23] N. Arkani-Hamed, S. Dimopoulos, and G. Dvali. The hierarchy problem and new dimensions at a millimeter. *Phys. Lett.*, B(429):263, 1998. hep-ph/9803315.
- [24] L. Randall and R. Sundrum. A large mass hierarchy from a small extra dimension. *Phys. Rev. Lett.*, 83:3370–3373, 1999. hep-ph/9905221.
- [25] P. Kanti, K. A. Olive, and M. Pospelov. Solving the hierarchy problem in two-brane cosmological models. hep-ph/0005146, 2000.
- [26] L. Randall and R. Sundrum. Out of this world supersymmetry breaking. *Nucl. Phys.*, B(557):79, 1999. hep-th/9810155.
- [27] I. Antoniadis, N. Arkani-Hamed, S. Dimopoulos, and G. Dvali. New dimensions at a millimeter to a fermi and superstrings at a TeV. *Phys. Lett.*, B(436):257, 1998. hep-ph/9804398.
- [28] J. F. Gunion, H. E. Haber, G. Kane, and S. Dawson. *The Higgs hunter’s guide*, chapter 7. Addison-Wesley, 1990.
- [29] Particle Data Group, D. Groom et al. Review of Particle Physics. *Eur. Phys. J.*, C(15), 2000.
- [30] C. H. Llewellyn Smith, G. G. Ross, and J. F. Wheather. Low-energy predictions from grand unified theories. *Nucl. Phys.*, B(177):263, 1981.
- [31] L. E. Ibáñez and G. G. Ross. Low energy predictions in supersymmetric grand unified theories. *Phys. Lett.*, 105B(6):439, 1981.
- [32] J. Ellis and D. Ross. A light higgs boson would invite supersymmetry. hep-ph/0012067, 2000.
- [33] H. Dreiner. An introduction to explicit R -parity violation. In G. Kane, editor, *Perspectives on supersymmetry*, chapter 20. World Scientific, 1998.
- [34] L. E. Ibáñez and G. G. Ross. Discrete gauge symmetries and the origin of baryon and lepton number conservation in supersymmetric versions of the standard model. *Nucl. Phys.*, B368:3–37, 1992.
- [35] I. Hinchliffe and T. Kaeding. B and L -violating couplings in the minimal supersymmetric standard model. *Phys. Rev.*, D(47):279, 1993.
- [36] G. R. Farrar and P. Fayet. Phenomenology of the production, decay, and detection of new hadronic states associated with supersymmetry. *Phys. Lett.*, B76:575–579, 1978.

- [37] F. Takayama and M. Yamaguchi. Gravitino dark matter without R -parity. *Phys. Lett.*, B(485):388, 2000. hep-ph/0005214.
- [38] SuperKamiokande Collaboration (Y. Fukuda et al.). Measurement of the flux and zenith angle distribution of upward through going muons by superkamiokande. *Phys. Rev. Lett.*, 82:2644, 1999. hep-ex/9812014.
- [39] SNO Collaboration (Q. R. Ahmad et al.). Measurement of the charged current interactions produced by b-8 solar neutrinos at the sudbury neutrino observatory. *Submitted to Phys.Rev.Lett.*, June 2001. nucl-ex/0106015.
- [40] M. Drees, S. Pakvasa, X. Tata, and T. ter Veldhuis. A supersymmetric resolution of solar and atmospheric neutrino puzzles. *Phys. Rev.*, D(57):5335, 1998. hep-ph/9712392.
- [41] A. Abada and G. Bhattacharyya. Can R -parity violation explain the LSND data as well? hep-ph/0007016, 2000.
- [42] H1 Collaboration, C. Adloff et al. Observation of events at very high Q^2 in ep collisions at HERA. *Z. Phys.*, C(74):191, 1997. hep-ex/9702012.
- [43] ZEUS Collaboration, J. Breitweg et al. Comparison of ZEUS data with standard model predictions for $e^+p \rightarrow e^+X$ scattering at high x and Q^2 . *Z. Phys.*, C(74):207, 1997. hep-ex/9702015.
- [44] G. Altarelli, J. Ellis, G. F. Giudice, et al. Pursuing interpretations of the HERA large- Q^2 data. *Nucl. Phys.*, B(506):3, 1997. hep-ph/9703276.
- [45] E. Perez (on behalf of the H1 and ZEUS collaborations). Searches for exotica at HERA. In K. Huitu et al., editors, *International Europhysics Conference on High Energy Physics 99*, page 818, 2000. hep-ex/9911037.
- [46] C. Oehler. Analysis of the KARMEN time-anomaly. *Nucl. Phys. B, Proc. Suppl.*, 85:101, 2000.
- [47] E. Zimmerman. Recent results addressing the KARMEN timing anomaly. In *CIPANP2000*, 2000. hep-ex/0009008.
- [48] D. Choudhury, H. Dreiner, P. Richardson, and S. Sarkar. A supersymmetric solution to the KARMEN time anomaly. *Phys. Rev.*, D(61):95, 2000. hep-ph/9911365.
- [49] D. Choudhury and S. Sarkar. A supersymmetric resolution of the KARMEN anomaly. *Phys. Lett. B.*, 374:87, 1996. hep-ph/9511357.
- [50] P. Richardson. *Simulations of R -parity violating SUSY models*. PhD thesis, University of Oxford, 2000. hep-ph/0101105.
- [51] L. E. Ibáñez and G. G. Ross. Discrete gauge symmetry anomalies. *Phys. Lett.*, B(260):291–295, 1991.
- [52] G. Gilbert. Wormhole-induced proton decay. *Nuc. Phys.*, B(328):159–170, 1989.
- [53] P. Z. Skands. Did R -conservation kill the proton?. Talk given at 3rd Nordic LHC Workshop. Slides at <http://www.fys.uio.no/epf/nordic-network/programme.htm>.

- [54] L. M. Krauss and F. Wilczek. Discrete Gauge Symmetry in Continuum Theories. *Phys. Rev. Lett.*, 62(11):1221–1223, 1989.
- [55] S. Weinberg. Baryon- and lepton-nonconserving processes. *Phys. Rev. Lett.*, 43(21):1566, 1979.
- [56] H. Murayama. Probing physics at short distances with supersymmetry. In G. Kane, editor, *Perspectives on supersymmetry*, chapter 13. World Scientific, 1998.
- [57] B. de Carlos and P. L. White. R-parity violation effects through soft supersymmetry breaking terms and the renormalisation group. *Phys. Rev. D*, 54(5):3427, 1996. hep-ph/9602381.
- [58] M. E. Peskin and D. V. Schroeder. *An Introduction to Quantum Field Theory*. Perseus Books, 1995.
- [59] T. Sjöstrand. PYTHIA 5.7 and JETSET 7.4 Physics and Manual. hep-ph/9508391, 1993.
- [60] F. James. Monte Carlo theory and practice. *Rep. Prog. Phys.*, 43:73, 1980.
- [61] ATLAS Inner Detector Community. Inner Detector Technical Design Report. Technical report, CERN, 1997. CERN/LHCC 97-16.
- [62] ATLAS Collaboration. Calorimeter Performance Technical Design Report. Technical report, CERN, 1997. CERN/LHCC 96-40.
- [63] ATLAS Tile Calorimeter Collaboration. Tile Calorimeter Technical Design Report. Technical report, CERN, 1996. CERN/LHCC 96-42.
- [64] ATLAS Collaboration. Liquid Argon Calorimeter Technical Design Report. Technical report, CERN, 1996.
- [65] ATLAS Collaboration. ATLAS Technical Proposal. Technical report, CERN, 1994. CERN/LHCC 94-43.
- [66] E. Richter-Was et al. ATLFAST 2.0 a fast simulation package for ATLAS. ATLAS Internal Note ATL-PHYS-98-131, 1998.
- [67] R. K. Ellis, W. J. Stirling, and B. R. Webber. *QCD and Collider Physics*. Cambridge University Press, 1996.
- [68] DØ Collaboration (B. Abbot et al.). Determination of the absolute jet energy scale in the DØ calorimeters. *Nucl. Instr. Meth.*, A424:352, 1999. hep-ex/9805009.
- [69] ATLAS Muon Collaboration. ATLAS Muon Spectrometer Technical Design Report. Technical report, CERN, 1997. CERN/LHCC 97-22.
- [70] G. Feldman and R. Cousins. Unified approach to the classical statistical analysis of small signals. *Phys.Rev.D.*, 57:3873, 1998.
- [71] B. C. Allanach, A. Dedes, and H. K. Dreiner. Bounds on R-parity violating couplings at the weak scale and at the GUT scale. *Phys. Rev.*, D60:075014, 1999. hep-ph/9906209.

- [72] I. Hinchliffe. Private communication. 2001.
- [73] B. Webber. Improving QCD event generators. Talk Given at the Durham Workshop, 2000. Slides can be found at <http://www.hep.phy.cam.ac.uk/theory/webber>.
- [74] J. Forshaw and M. Seymour. Subjet rates in hadron collider jets. *JHEP*, 09:009, 1999. hep-ph/9908307.
- [75] M. Seymour. Jets in hadron collisions. In *QCD and High Energy Hadronic Interactions*, Les Arcs, Savoie, France, March 2000. hep-ph/0007051.
- [76] J. Bystricky et al. ATLAS trigger menus at luminosity $10^{33}\text{cm}^{-2}\text{s}^{-1}$. *ATLAS Internal Note*, 1996. DAQ-NO-054.
- [77] J. McClelland and D. Rumelhart. *Explorations in Parallel Distributed Processing*. MIT Press, 1989. Fourth print.
- [78] Y. LeCun et al. Optimal brain damage. In D. S. Touretsky et al., editors, *Advances in Neural Information Processing Systems 2*, pages 396–404. MIT Press, 1990.
- [79] H. Baer, C. Chen, and X. Tata. Impact of hadronic decays of the lightest neutralino on the reach of the CERN LHC. *Phys. Rev.*, D55:1466–1470, 1997.
- [80] S. Mrenna. SPYTHIA, a supersymmetric extension of PYTHIA 5.7. *Comp. Phys. Comm.*, 101:232, 1997.
- [81] G. Corcella et al. Herwig 6: An event generator for hadron emission reactions with interfering gluons (including supersymmetric processes). *JHEP*, 01:010, 2001. hep-ph/0011363.
- [82] H. Baer et al. Higgs boson signals in superstring inspired models at hadron supercolliders. *Phys. Rev.*, D(36):96, 1987.